DEVELOPMENT OF II-VI AND IV-VI GROUP QUANTUM DOTS AND THEIR CORE/SHELL STRUCTURES

Thesis submitted in fulfillment for the requirement of the degree of

DOCTOR OF PHILOSOPHY

in

PHYSICS

by

Hitanshu Kumar

[Enrollment No. 116902]

DEPARTMENT OF PHYSICS AND MATERIALS SCIENCE

JAYPEE UNIVERSITY OF INFORMATION TECHNOLOGY WAKNAGHAT
SOLAN-173234, H.P, INDIA

MAY 2015

JAYPEE UNIVERSITY OF INFORMATION TECHNOLOGY
(Established by H.P. State Legislature vide Act No. 14 of 2002)
P.O. Waknaghat, Teh. Kandaghat, Distt. Solan - 173234 (H.P.) INDIA
Website : www.juit.ac.in
Phone No. +91-01792-257999 (30 Lines).
Fax: +91-01792-245362

DECLARATION

I hereby declare that the work contained in the PhD thesis entitled **"Development of II-VI and IV-VI group quantum dots and their core/shell structures"** is original and has been done by me under the supervision of Dr. Ragini Raj Singh (Supervisor) and Prof. P. B. Barman (Co-supervisor) submitted to **Jaypee University of Information Technology, Waknaghat, India**. The work has not been submitted to any other organization for any degree or diploma.

Hitanshu Kumar.

(Hitanshu Kumar)
Department of Physics & Materials Science
Jaypee University of Information Technology
Waknaghat, Solan, H.P. India-173234

Date: **May 11, 2015**

JAYPEE UNIVERSITY OF INFORMATION TECHNOLOGY
(Established by H.P.State Legislative vide Act No. 14 of 2002)
Waknaghat, P.O. DumeharBani, Kandaghat, Distt. Solan – 173234 (H.P.) INDIA
Website: www.juit.ac.in
Phone No. (91) 07192-257999 (30 Lines)
Fax: (91) 01792 245362

CERTIFICATE

This is to certify that the work reported in the Ph.D. thesis entitled "**Development of II-VI and IV-VI group quantum dots and their core/shell structures**", which is being submitted by **Hitanshu Kumar** for the award of degree of Doctor of Philosophy in Physics by Jaypee University of Information Technology, Waknaghat, India, is the record of the candidate's own work, carried out under our supervision. This work has not been submitted partially or wholly to any other university or institute for the award of this or any other degree or diploma.

Dr. Ragini Raj Singh

Supervisor
Assistant Professor
Department of Physics and Materials Science
Jaypee University of Information Technology
Waknaghat, Solan, H.P. India-173234

Date: May 11, 2015

Prof. P. B. Barman

Co-supervisor
Head of the Department
Department of Physics and Materials Science
Jaypee University of Information Technology
Waknaghat, Solan, H.P. India-173234

ACKNOWLEDGEMENT

First of all from the depth of my heart I express my deep sincere gratitude to the Almighty for the blessings He had bestowed upon me to do this work.

I am immensely pleased to place on record my profound gratitude and heartfelt thanks to my supervisor, ***Dr. Ragini Raj Singh,*** *Assistant Professor of Physics Department of Physics and Materials Science, Jaypee University of Information Technology for her guidance and constant encouragement during my research. She provided inspiring guidance for the successful completion of my research work. I deem it as my privilege to work under her able guidance. I ever remain grateful to her.*

I great fully acknowledged and thank my co-supervisor ***Prof. P. B. Barman,*** *Head of the Department, Department of Physics and Materials Science, for his guidance, help, encouragement and cooperation throughout my research work.*

I insistently express my loyal and venerable thanks to ***Dr. Y. Medury*** *(former COO, JUIT),* ***Brig. (Retd.) Balbir Singh*** *(Director JUIT), and* ***Prof. T. S Lamba*** *(Dean JUIT) for providing opportunity to pursue my research work at Jaypee University of Information Technology, Waknaghat (H.P).*

I owe my thanks to ***Prof. Sunil Kumar Khah, Dr. Vineet Sharma, Dr. Pankaj Sharma, Dr. Rajesh Kumar, Dr. Surajit Kumar Hazra Dr. Sanjiv Kumar Tiwari (JUIT) and Dr. Manoj Kumar (JIIT Noida)*** *for providing me assistance, moral support, suggestions and necessary facilities in the department during the course of my research work.*

I am also thankful to all members of technical and non-technical staff ***Mr. Ravender Tiwari and Mr. Deepak Singh*** *for their valuable contributions.*

I also thanks to all Universities (JIIT Noida, IIT Rorkee, Panjab University) for allowing me the facilities for characterization.

It was indeed my good luck to have seniors Ankush Thakur, Abhishek, Pawan, Jai Vardhan, Ankush Badyal and Shweta who extended their support in all possible ways. I thank them for always being there to guide and encourage whenever the journey got tough. I am also privileged to have friends who always stood beside me. I extend my heartfelt thanks to my friend Rajinder Kumar and Bandana Bharti. I also thank my other colleagues Rajinder Singh, Sarita kango, Dikshita Gupta, Krishna Hari Sharma, Jonny Dhiman, Prashant Thakur, Neha Kondal, Rohit Sharma and Asha Kumari.

This work would have taken scans the moral supports and encouragement rendered by my family. I can never enough thanks to my brother and sisters for supporting my decision to take research and always being there.

Words cannot express my humble gratitude to my dear parents for their affectionate encouragement and blessing to complete this research work. My research work have couldn't be possible without their unconditional love and support.

Hitanshu Kumar

LIST OF PUBLICATIONS

1. Stable and luminescent wurtzite CdS, ZnS and CdS/ZnS core/shell quantum dots **Hitanshu Kumar**, Manoj Kumar, P. B. Barman, Ragini Raj Singh, Applied Physics A, November 2014, Volume 117, Issue 3, pp 1249-1258.
2. Effect of size and shell: Enhanced optical and surface properties of CdS, ZnS and CdS/ZnS quantum dots **Hitanshu Kumar**, P.B. Barman, Ragini Raj Singh Physica E: Low-dimensional Systems and Nanostructures, Volume 67, March 2015, Pages 168–177.
3. Low-temperature growth of inverted hexagonal ZnS/CdS quantum dots: functional and luminescence properties **Hitanshu Kumar**, P.B. Barman and Ragini Raj Singh Journal of electronic materials, 2015, Volume 44, Issue 2, pp 675-681.
4. Size-Controlled Synthesis and Characterization of CdS, ZnS Quantum Dots and their Core/Shell Structures for Bio Based Applications. **Hitanshu Kumar**, Partha Bir Barman, Ragini Raj Singh (2013). Proceedings of the National Conference on Multifunctional Advanced Materials [Shoolini University, Solan, India: May 2-4, 2013].
5. Development of CdS, ZnS quantum dots and their core/shell structures by wet chemical method. **Hitanshu Kumar**, P. B. Barman and Ragini Raj Singh, International Journal of Scientific and Engineering Research, 5(5) (2014) 40-53.
6. Controlled growth and characterization of CdS, ZnS, CdS/ZnS and ZnS/CdS core-shell quantum dots. **Hitanshu Kumar**, Partha Bir Barman, Ragini Raj Singh (2014). Proceedings of the NanoSciTech2014. Punjab University, Chandigarh, India: February 13-15, 2014 [Book Chapter].
7. Kumar, Hitanshu, et al. "Low temperature regulated growth of PbS quantum dots by wet chemical method." advanced materials and radiation physics (amrp-2015): 4th National Conference on Advanced Materials and Radiation Physics. Vol. 1675. AIP Publishing, 2015.
8. Kumar, R., Kumar, H., Singh, R. R., & Barman, P. B. (2015, August). Structural analysis of emerging ferrite: Doped nickel zinc ferrite. In advanced materials and radiation physics (amrp-2015): 4th National Conference on Advanced Materials and Radiation Physics (Vol. 1675, p. 030003). AIP Publish

9. Wurtzite ZnS/CdS/ZnS Quantum Dots Quantum Well: High luminescence with narrow emission due to narrow distribution. **Hitanshu Kumar**, Partha Bir Barman, Ragini Raj Singh under review in Materials Science and Engineering: B.
10. Amelioration in Optical Properties of wurtzite CdS/ZnS and ZnS/CdS Quantum Dots by Shell Alteration. **Hitanshu Kumar**, Partha Bir Barman, Ragini Raj Singh under review in Nanotechnology.

11. Investigation of Structural and Optical properties of PbS quantum dots. **Hitanshu Kumar**, Umesh Chandra Bind, P. B. Barman and Ragini Raj Singh under review in International Journal of Scientific and Engineering Research.
12. Synthesis and structural analysis of co doped Ni-Zn ferrite. Rajinder Kumar, **Hitanshu Kumar**, Manoj Kumar, Ragini Raj Singh and P. B. Barman under review in International Journal of Scientific & Engineering Research.
13. Enhanced saturation magnetization in cobalt doped Ni-Zn ferrite nanoparticles Rajinder Kumar, **Hitanshu Kumar**, Manoj Kumar, Ragini Raj Singh and P. B. Barman under review in Physics of the Solid State.
14. Structural and magnetic properties variation with doping: Cations distribution effect" Rajinder Kumar, **Hitanshu Kumar**, Ragini Raj Singh, and P. B. Barman under review in Inorganic materials.

PARTICIPATION / PRESENTATIONS IN WORKSHOPS / CONFERENCES

1. National Conference on Recent Trends in Materials Science (RTMS-11), JUIT Waknaghat, 08-10 Oct, 2011.
2. Two Day Workshop on "Antenna Materials" 14^{th} – 15^{th} December, 2012 at JUIT Waknaghat.
3. National Conference on Multifunctional Advanced Materials, at Shoolini University, Solan, India, May 2-4, 2013.
4. One week Workshop on "Nanotechnology (Fabrication and Characterization)" December 11, 2013 at JUIT Waknaghat.

5. International conference NanoSciTech2014 held in Punjab University, Chandigarh from 13 Feb to 15 Feb 2014.
6. National Conference on Advanced Materials and Radiation Physics (AMRP-2013) [SLIET, Longowal (Punjab) India : November 22-23, 2013}
7. National Conference on Advanced Materials and Radiation Physics (AMRP-2015) (March 13-14, 2015) [SLIET, Longowal (Punjab) India].
8. First International Convention of Engineering and Management at (iCEM-2015) JUIT Waknaghat.
9. 2nd International Convention of Engineering and Management (iCEM-2015) at JUIT Waknaghat Solan (H.P) India

LIST OF FIGURES

LIST OF TABLES

ABSTRACT

This thesis work preferentially concerned with the size tunable and stable quantum dots (QDs) synthesized by solution growth method at room temperature using 2-mercaptoethanol. Excellent structural, optical and surface properties have been attained such as highly stable structure and high luminescence. Prepared quantum dots structures and core/shell quantum dots structures are: CdS, ZnS, CdS/ZnS, ZnS/CdS, ZnS/CdS/ZnS, PbS, PbSe, PbSe/PbS.

CONTENTS

CHAPTER – I

INTRODUCTION

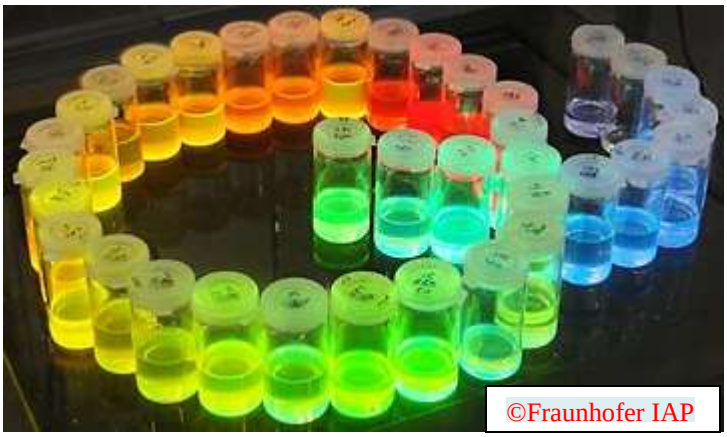

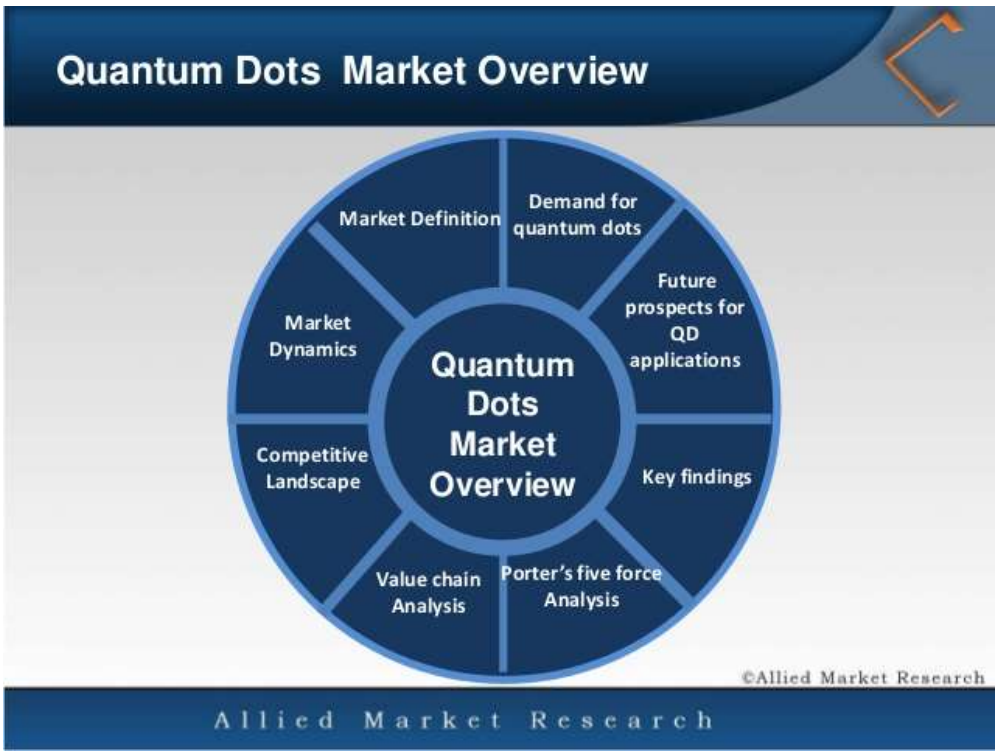

1.1 INTRODUCTION

1.1.1 Small is beautiful

Nanostructure materials are interesting, because they can link the gap between the bulk and molecular levels and leads to entirely new route for applications, especially in electronics, optoelectronics and biology. Semiconductor nanocrystals, especially quantum dots (QDs), have attracted much attention in the past decades owing their unique properties due to the quantum confinement. The size of QDs is on nanometer scale and the diameter is less than the Bohr exciton radius and the exciton are confined by potential barriers in all three dimensions [1]. Size dependent optical properties and quantum confinement was introduced by both Rossetti et al (1984) and Ekimor et al (1982). Luminescent semiconductor QDs, are generally composed of II-VI and IV-VI elements. QDs show some unique, fascinating optical properties, and are characterized as narrow with fine emission spectra, high quantum yields, broad absorption spectra, good chemical and photo-stability properties which is size dependent emission wavelength tunability. In recent times, QDs have been successfully used as new fluorescent tags in many biological, biomedical fields and become a new promising tool in biomedical studies, like drug delivery and clinical diagnostics. During the last decade, many solution based methods have been investigated for the synthesis of QDs. The evolution of new synthetic strategies for monodisperse, size tunable QDs from different materials has given rise to their wide spread applications in imaging, electroluminescent devices, lasing, photonic crystal structures etc [2]. Several routes have been used to synthesize QDs but, generally, techniques for QD synthesis used top-down processing methods and bottom-up approach. Top-down processing methods include molecular beam epitaxy (MBE), ion implantation, E-beam lithography and X-ray lithography. Using the alternative bottom-up approach, QDs are prepared by the solution following chemical reactions and they may be broadly sub divided into wet-chemical and vapor-phase methods. Wet-chemical methods are generally micro emulsion, sol–gel, solution growth and hot-solution decomposition. Vapor-phase methods for producing QDs begin with processes in which layers are grown in an atom-by-atom process. Among the different methods used to grow nanocrystals, solution growth at low temperatures is widely used because of its versatility and simplicity [3]. After many modifications and refinements, the solution growth procedure

now yields high-quality nanocrystals for a variety of applications. The main advantages of solution growth are: 1. Full control of particle size with high surface area and high purity in comparison with other methods; 2. Particle size can be controlled by adjusting preparation time or by use of a capping agent and agglomeration is negligible; 3. The method requires fewer and inexpensive chemicals; 4. The synthesis is performed at low temperature (35^{o}±2C); 5. The conditions used for synthesis of core and shell materials can be readily modified and provide an excellent environment for production of compatible cores and shells; 6. The monodispersed nanoparticles with high luminescence are produced. The individuality of the structural characteristics, energetic response, physics and chemistry of nanoparticles is indeed experimental and conceptual background for novel devices so these are the reasons for ***small is beautiful***……..Nowadays "Nanoscience and Nanotechnology" has some different nature and fact that make nanotechnology emerging and interesting for the society.

1.1.2 Basics of quantum dots

Quantum dots are very small particles of semiconductor materials ranges in a few nanometers and possess hundred to a few thousand atoms. The diameter of a quantum dot typically lies between two to ten nanometers. Quantum dots are semiconductor nanocrystals that exhibit unique optical properties due to a combination of their material band gap energy and quantum confinement phenomena. Due to their extremely small size, in nanometers, the dots behave similarly to three dimensional quantum wells. When an electron is excited by a photon striking the quantum dot, it behaves as a particle confined in an infinite potential well, since the electron cannot escape from the quantum dot. The hole, created by the excited electron, behaves in the same fashion. The energy levels can be calculated using the "particle in a box model" in which the energy of different states is dependent on the dimensions of the box. If the radius of the nanoparticles is equal to the exciton Bohr radius than there QDs are in the "weak confinement regime" while quantum dots are said to be in the "strong confinement regime" if their radii are smaller than the exciton Bohr radius. If the size of the QDs is less than 10 nm then "quantum confinement effects" lead electronic and optical properties become highly tunable. Small quantum dots emit higher energy light than larger quantum dots, which makes the wavelength of light emitted by the particles tunable, with smaller particles emitting blue light and larger particles emitting red light (Figure 1.1).

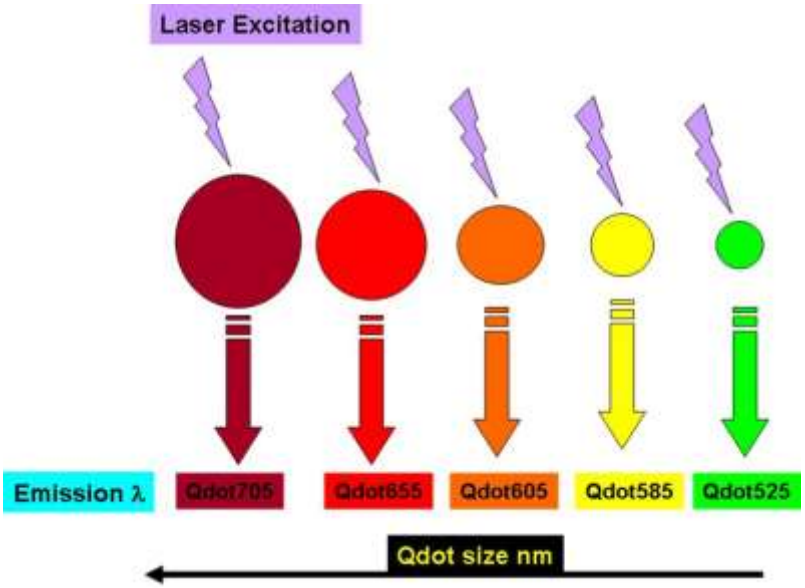

Figure 1.1: The wavelength of light emitted by quantum dots is tunable by changing the particle size. In this image, all of the quantum dot samples are excited by the same UV wavelength, but emit different visible wavelengths depending on particle size.

1.1.3 Core/shell quantum dots

Motivation behind formation of core/shell quantum dots: Since quantum dots are only a few nanometers in diameter, they have a very high surface-to-volume ratio, maximum number of atoms be located on the surface. Due to this high surface-to-volume ratio estimated that the properties of the surface have significant effects on the optical and structural properties of the particles. These very reactive surfaces induce the defects at the surface. Surface defects, just as dangling bonds, are surface-related trap states that act as non irradiative recombination sites which degrade the fluorescence quantum yield of quantum dots. Important motivation of utilizing core/shell nanostructure is to improve properties of core/shell QDs, such as luminescence efficiency. The organic ligand that surround colloidal quantum dots lend some degree of surface passivation, but do not provide sufficient protection from the surrounding environment or complete passivation of surface defects. To better passivate surface, a secondary semiconductor with band gap structure proposing electron hole pair reaching the surface can be epitaxially grown surrounding the core particle. After coating the core with shell, the quantum yield has been shown to greatly increase up to ten times, as well as displaying increased stability

against photo-oxidation and environmental attack. This is the motivation behind the core/shell QDs.

1.1.4 Types of core/shell quantum dots

The materials for the shell layer depend on the properties that we desire after coating. To understand this a little better, we need to look at the different "types" of core/shell systems. There are three main types, characterized by the alignment of the valence and conduction bands between the core and shell (Figure 1.2).

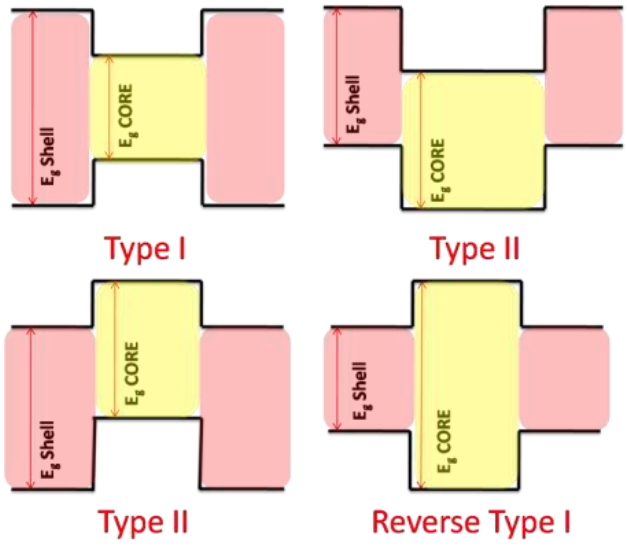

Figure 1.2: Band (valence and conduction bands) alignment of different core/shell systems.

The first and most common core/shell system is type-I in which a higher band gap semiconductor shell is formed on the core, confining the exciton to the core. The primary purpose of the type-I core/shell system is increasing fluorescence quantum yield by passivating the surface of the core, as well as isolating the core from the environment and reducing degradation. One of the first core/shell systems was CdSe/ZnS, which is the focus of this study as well. In type-I systems, there is a characteristic slight red shift, usually around 10 nm, of the fluorescence due to some leakage of the exciton from the core into the shell [4]. In reverse type-I systems, a narrower band gap semiconductor is grown onto a higher band gap core, partially delocalizing charge carriers from the core to the shell. Reverse type-I core/shell quantum dots are used when control is wanted over the red shifting of the fluorescence spectrum, as the shift can

be controlled by changing the coating thickness. The most common reverse type-I systems are CdS/CdSe and ZnSe/CdSe. Type-II core/shell systems aim to significantly red shift the fluorescence, often into wavelengths that are otherwise unattainable with the same materials. This is done by coating the core with a shell that has a staggered band gap from its own, creating a smaller effective band gap than either the core or shell. These core/shell types can be achieved using a wide variety of combinations of materials depending on the desired band alignment (Figure 1.3). Coe/shell and inverted core/shell quantum dots (QDs) synthesized using wet chemical route are a class of materials which are actively being explored because of their amendable optical and electronic properties. These kinds of QDs are extremely valuable class of materials in various applications such as light emitting diodes, photovoltaic devices, lasers, biological labeling, etc. [5, 6]. The optical and structural properties of these materials can be modified by controlling the size of QDs [6]. In general in all types of core/shell QDs (e.g. CdS/ZnS), shell increases quantum yield by passivating the surface trap states. Besides that the shell provides protection against environmental changes, photo-oxidative degradation and another route for modularity. Strict control of the size, shape, narrows FWHM (Full width at Half Maximum); high fluorescent quantum yield, and good monodispersity achieved by core/shell QDs. These materials have found good applications in biological systems. In such core/shell QDs, the shell provides a physical barrier between the optically active core and the surrounding medium, thus making the core/shell less sensitive to environmental changes and giving rise to a strongly enhanced fluorescence quantum yield. These effects are fundamental condition for the use of core/shell QDs in applications such as biological labeling and light-emitting devices, which depend on their emission properties. Specifically in inverted core/shell structures a core of a wide-gap semiconductor is over coated with a shell of a narrower gap material. The core and shell enable the emission wavelength to be tuned over a wider range of wavelengths than with either individual semiconductor. These “inverted” QDs provide capabilities for controlling functionalities by a direct control of the distribution of electron and hole wave functions and the *e-h* overlap integral; specifically by increasing the thickness of the shell for a fixed core size [7]. In these systems the size of core was retained fixed with varying shell thicknesses by controlling the size of shell QDs with the aid of capping agent. Surface modification of core material that is surrounded by another material is able to modify the orientation of charges and reactivity of the materials. Consequently results in enhancement in the

PL emission intensity due to localization of the e-h pair [8-10]. It implies that the wave function of electron and hole may be spatially separated in core and shell, reducing the probability of non-radiative decay in the surface states and trap sites [11]. This behavior of core/shell and inverted core/shell QDS are attractive in terms of the localization of e-h pair which is relatively extraordinary from the other core/shell QDs. Several different combinations of core/shell QDs such as CdSe/ZnS, CdS/ZnS, ZnO/ZnS, ZnSe/ZnS, CdSe/CdS, CdS/PbS, and ZnSe/CdS have previously been studied by different groups [12, 13].

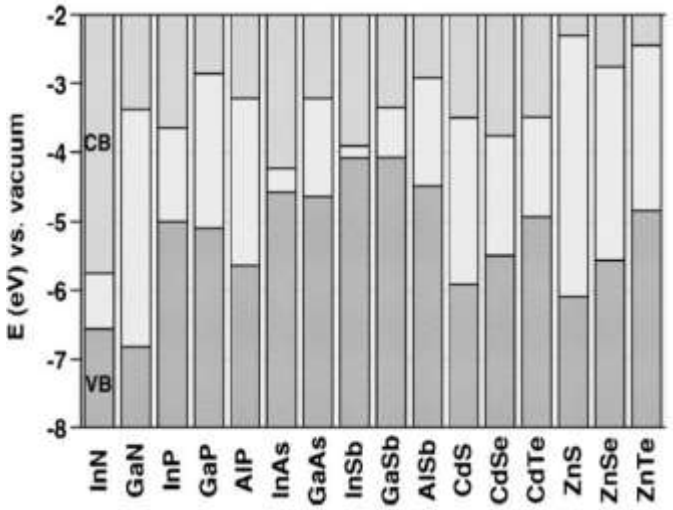

Figure 1.3: Electronic energy levels of selected III-V and II-VI semiconductors based valence band offsets (CB = conduction band, VB = valence band) (Reiss, P., Protiere, M., & Li, L. (2009). Core/shell semiconductor nanocrystals. small, *5*(2), 154-168).

1.1.5 Multishell structures

Particularly, scientists give more attention to QDs; core/shell QDs and multishell QDs because these classes of semiconductor nanocrystals will lead to a series of novel optical and electronic properties [14, 15]. The core/shell CdS/ZnS structures [16–17] and multilayer structures of CdS and ZnS (CdS/ZnS) [18-20] have attracted much attention now a days, since the optical properties can be enhanced and the band gap can be tuned by the surface chemical bonds and charge transfer in the surface/interface region of QDs and multishell QDs structures. Multishell QDs structures represent the special case of a core/shell/shell structure in which a lower band gap layer is embedded between a higher-band gap core and outer shell material with both semiconductors having type-I band alignment (right panel in Figure 1.3). Among the first

systems studied was CdS/HgS/CdS. [21] These kinds of structures with unique properties can be prepared by a chemical or physical process, and some new and enhanced physical properties were found due to the core/shell interface effects [22, 23]. Numerous investigations have focused on forming the multishell QDs by sandwiching the low band gap material in the well between the layers of quantum dots of higher band gap material viz. ZnS/PbS/ZnS [24], CdS/HgS/CdS [21], ZnS/CdSe/ZnS [25]. Literature states that when the low band gap material over coated with high band gap materials, formed core/shell sort of QDs or multishell QDs exhibit high photoluminescence intensity as a result of elimination of surface nonradiative recombination [26]. It has been found that few other also synthesized ZnS/CdS/ZnS with different method like (PLD), chemical method in an air atmosphere. Beside this many other authors have also been reported on ZnS/CdS/ZnS multishell QDs but they have opted for different synthesis methods and particles were of cubic structures [27]. Very few authors have been reported the wurtzite ZnS/CdS/ZnS but methods were different or they were used physical synthesis method on high temperatures [28, 29]. Uniform shell coverage was observed only for graded shells (e.g., CdS/ZnS) and was found to be critical to achieving high luminescence.

1.1.6 Density of states

Density of states (DOS) of in a system can be describes as the number of states per interval of energy at each energy level that are available to be occupied by electrons. For semiconducting quantum dots, the density of states are the sharp in the valance and conduction bands. The sharp edges in the density of states produce well-defined forbidden gap. Within the band, however, one density of states is extended implying that the wave functions occupy the entire volume.

(i) In a three-dimensional crystal, the energy states of electrons are characterized by the quantum number $\vec{k}$. The density of states D (E) varies as

$$D(E) = \left(\frac{m^*}{\hbar^2} \right)^{3/2} \frac{\sqrt{2E}}{\pi^2} \qquad (1.1)$$

Note that the energy E is related to $\vec{k}$, $E = \frac{\hbar^2 k^2}{2m}$ and $\hbar = k_x^2 + k_y^2 + k_z^2$, $k_{xyz} = \frac{2\pi}{a} n_{x,y,z}$

The dependence of D (E) on E has been shown in Figure 1.4 a

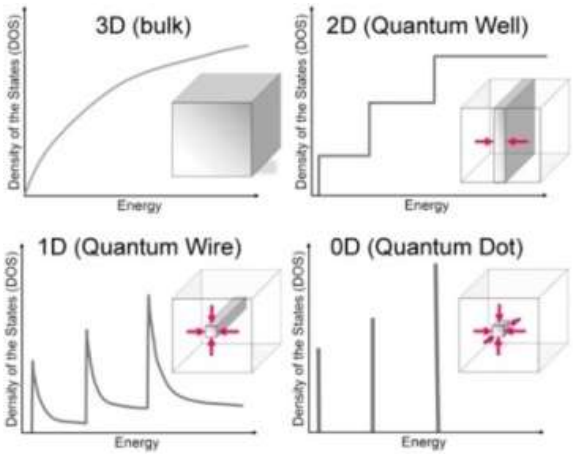

Figure 1.4: The density of states as a function of energy for (i) 3-D bulk, (ii) 2-D quantum well, (iii) 1-D quantum wire, and (iv) 0-dimensional quantum dot systems.

(ii) When the carrier are confined in one direction say the z direction. The energy of the system is given by

$$E = \frac{\hbar^2 k_z^2}{2m^*} + \frac{\hbar^2 k^2}{2m^*} \qquad (1.2)$$
$$= E_n + E_{x.y}$$

where $E_n = \frac{\hbar^2 k_z^2}{2m^*}$ is the confinement energy in z direction while $\frac{\hbar^2 k^2}{2m^*}$ is the energy in the other two direction (x & y). The density of state can now be expressed as

$$D_{2D}(E) = \frac{m^*}{\pi\hbar^2} \sum_n \theta(E - E_n) \qquad (1.3)$$

where θ is the step function

The quantum confinement in the z-direction thus leads to a ladder of states giving rise to a piecewise constant density of states shown schematically in Figure 1.4b

(iii) For confinement in two directions (say z & y) the total energy of the system can be written as

$$E = \frac{\hbar^2 k_z^2}{2m^*} + \frac{\hbar^2 k_y^2}{2m^*} + \frac{\hbar^2 k_x^2}{2m^*} \qquad (1.4)$$

where $k_z = \frac{p\pi}{L_z}, k_y = \frac{q\pi}{L_z}$, where p & q are integers

The density of states for all p & q is

$$D_{1D}(E) = \frac{1}{\pi}\left(\frac{2m^*}{\hbar^2}\right)^{1/2} \sum_{p,q} \frac{1}{\sqrt{E - E_{p,q}}} \theta(E - E_{p,q}) \qquad (1.5)$$

The density of state has been shown schematically in Figure 1.4 c

(iv) In case of zero dimensions, the confinement is in all three dimensions so that

$$D_{0D}(E) = \delta(E - E_n) \qquad (1.6)$$

The density of state will now be a delta function as shown in Figure 1.4.

Figure 1.4 shows that the DOS changes from a continuous dependence on $E^{1/2}$ to step like for 2D and delta function like for zero dimensional systems. The derivation of the Schrodinger equation for a low dimensional system was reported in literature.

1.1.7 Surface energy and surface to volume ratio

In the physics of solids surfaces must be intrinsically less energetically favorable than the bulk of a material (the molecules on the surface have more energy compared with the molecules in the bulk of the material), otherwise there would be a driving force for surfaces to be created, removing the bulk of the material. Simply all bonds in the bulk made without stress or strain. The surface energy may therefore be defined as the excess energy at the surface of a material compared to the bulk. Nanoparticles have an appreciable fraction of atoms on their surface. The general expression for specific surface area per gram 'S' is:

$$S = A / \rho V \qquad (1.7)$$

where ρ is the density expressed in g/cm^3, V the volume and A area of nanoparticles.

Obviously the specific surface area per gram scales up inversely with decrease in the size of nanoparticles. Simultaneously the surface free energy also increases. Thus nanoparticles have much greater surface area per unit mass compared with larger particles. The nanocrystals

therefore exhibit significantly high surface free energy. Thermodynamic properties will also be markedly different. Another important parameter related to scaling down a material is the relationship between the number of surface atoms 'Ns' vs the number of unit cells 'n' in a nanomaterials. For a zinc blende structure one can write

$$N_S = 12n^2, \quad D = na, \quad N_T = 8n^3 + 6n^2 + 3n$$

where D is the particle diameter, and a the lattice constant.

As the size of particles decreases, larger proportions of atoms will therefore be found at the surface compared to those within the bulk. For example a particle of size 30 nm has only 5% of surface atoms. The percentage increases from 20% to 50% as the size is decreased from 10 nm to 3 nm. The relative increase in surface area over the volume has been schematically shown in Figure 1.5. The higher surface area of nanomaterials also imparts them with a much higher catalytic activity in chemical reaction. The surface is therefore potentially important in dealing a with nonmaterial's properties.

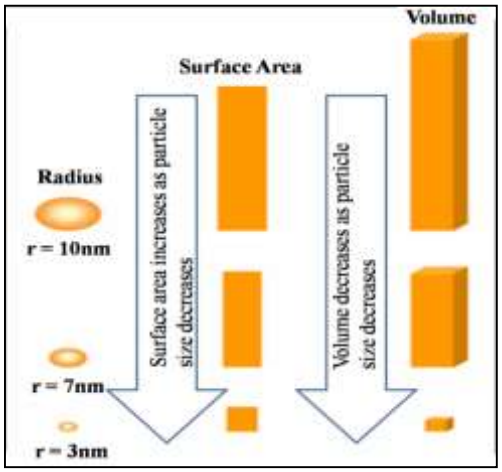

Figure 1.5: Interrelationships of radius, surface area, and volume of a quantum dot. Note that the volume decreases more rapidly than surface area for a given decrease in radius. Hence, surface area to volume ratio increases dramatically for a lower radius compared to the ratio for a higher radius.

1.1.8 Fluorescence

Fluorescence is the main property of semiconductor nanoparticles because of its optical property semiconductor nanoparticles are favorite materials for the scientist. When a photon of sufficient energy, greater than the band gap of the material, is incident on the material, an electron is excited from the valence band to the conduction band, forming a hole in the valence band. When the electron repose to the valence band, recombining with the hole left behind by its absence, a photon can be emitted, with energy comparative to the band gap of the material (Figure 1.6).

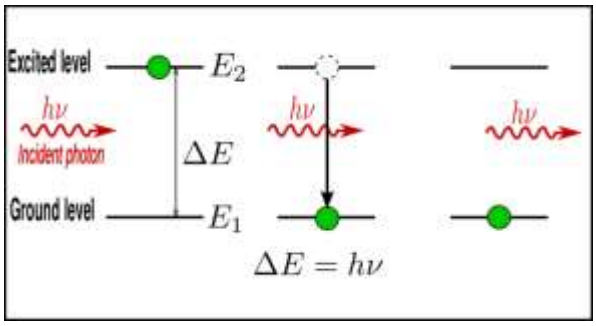

Figure 1.6: Mechanism of excitation and emission due to radiative recombination of an electron and hole.

1.1.9 The exciton

An exciton is a bound position of an electron and a hole which are bound to each other by the electrostatic force. When a photon incident on a semiconductor, electron can achieve energy from photon and get excited and reach in to the conduction band, a consequence a hole is also created in the valence band (Figure 1.7). Due coulomb attraction, the electron and hole form a bound state having some less energy than the unbound electron and hole. This bound state is termed an “exciton”. For semiconductors whose band gap is within the range of 1.4 to 2.5 eV, excitons are typically originate by the interaction of the crystal with visible light (absorption of a photon). As a result the separation between electron and hole, known as the effective Bohr radius a_B, is considerably larger than the crystal lattice constant (Mott–Wannier exciton). This system can be modeled as a hydrogen-like atom in which the relative motion of the electron and the hole can be described by an excitonic Bohr radius which is proportional to the square of the principle quantum number. Electronic parameters of II-IV bulk semiconductors used in this thesis have been given in table 1.1. Bohr exciton radius a_B in semiconductors is taken as an indicator of the size below which quantum confinement effects start manifesting. This can be expressed as

$$a_B = \frac{4\pi\varepsilon_0\varepsilon\hbar^2}{m_r^*.e^2} \qquad (1.8)$$

Where ε is the bulk optical dielectric coefficient, ε_0 is the permittivity in the vacuum, e is the elementary charge and m_r*can calculate as:

$$\frac{1}{m_r^*} = \frac{1}{m_e^*} + \frac{1}{m_h^*} \qquad (1.9)$$

where m_e*and m_h*are the electron and hole effective masses.

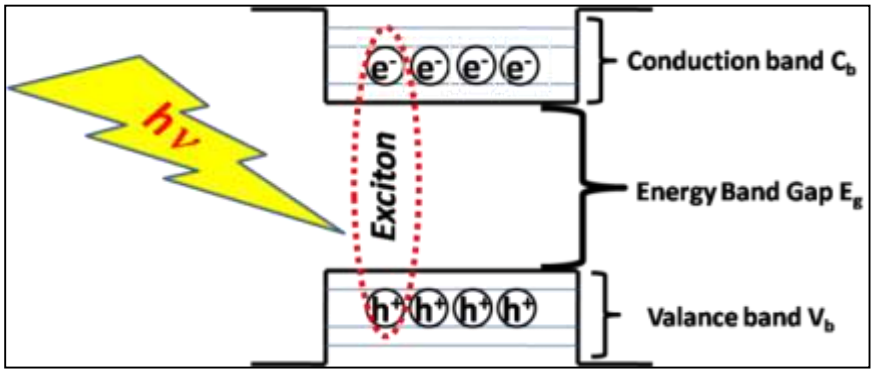

Figure 1.7: Exciton formations upon absorption of an incident photon. An electron (e^-) is excited from the valence band to a given level in the conduction band creating a hole (h^+) in the valence band.

When excitons are confined to a space smaller than the Bohr exciton radius, or the spatial separation between the electron and the hole left behind when it jumps the band gap, fewer states become available. This continues until excitons are confined in all three dimensions, at which point the energy levels become discrete. A schematic representation of the materials belonging to the categories - bulk (three dimensions), quantum well (two dimensions), quantum wire (one dimension) and quantum dot (zero dimensions) has been given in Figure 1.8.

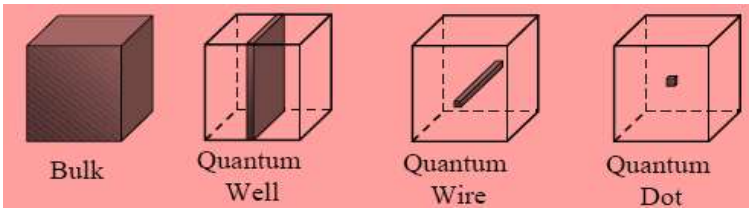

Figure 1.8: A schematic of the degree of confinement for bulk, quantum well, quantum wire, and quantum dot structures.

Table 1.1: Electronic parameters of II-IV bulk semiconductors used in this thesis (Source: Landolt–Börnstein - Group IV Physical Chemistry (Springer); Volume 19, Sub volume B2, 2004).

Materials Name	**Band gap E_g [eV]**	**Electron effective mass m_e^***	**Hole effective mass m_h^***	**specific dielectric constant(κ)**	**Bohr exciton radius a_B [nm]**
CdS	2.45	0.18	0.60	9.28	3.6
ZnS	3.62	0.20	0.80	8.30	2.8
PbS	0.37	0.080	0.075	17.2	18
PbSe	0.27	0.047	0.041	25	47

1.1.10 Quantum confinement effect

There are a variety of ways to experimentally observe quantum confinement. If a material is experiencing quantum confinement there should be a shift of the band gap edge toward the blue wavelengths. There is a clear shift in the band edge toward shorter wavelengths as the size of the dot decreases. The amount of blue shift due to size effects is a material dependent phenomenon. Tunable band gap in quantum dots have point of the concern which originate by the quantum confinement. To understand quantum confinement, first of all we need to understand how energy bands changed from bulk level to atom level. Atoms have degenerate, discrete energy levels at which electrons can be located, allowing more than one electron to be located in a single energy level. When two or more than two atoms are brought together, the electrons of these atoms starts to interact with each other and generate states that split into different energy levels. Once the interacting atoms reaches at the bulk level, the states are split into numerous energy levels that the states can be considered continuous because the spacing between energy levels is very small. (Figure1.9). Confinement regime occurs in the QDs where the size of the QDs becomes comparable to or smaller than the Bohr exciton radius,

$$a_B = \frac{\hbar^2 \varepsilon}{e^2}\left[\frac{1}{m_e^*} + \frac{1}{m_h^*}\right] \qquad (1.10)$$

The QDs acts as a quantum box for the quasi particles with infinitely high energy walls. It can be shown that size quantization gives discrete k values for the electrons and holes. This implies the carriers are quantized in one-dimension, i.e. in the direction perpendicular to the interfaces. This is known as quantum confinement.

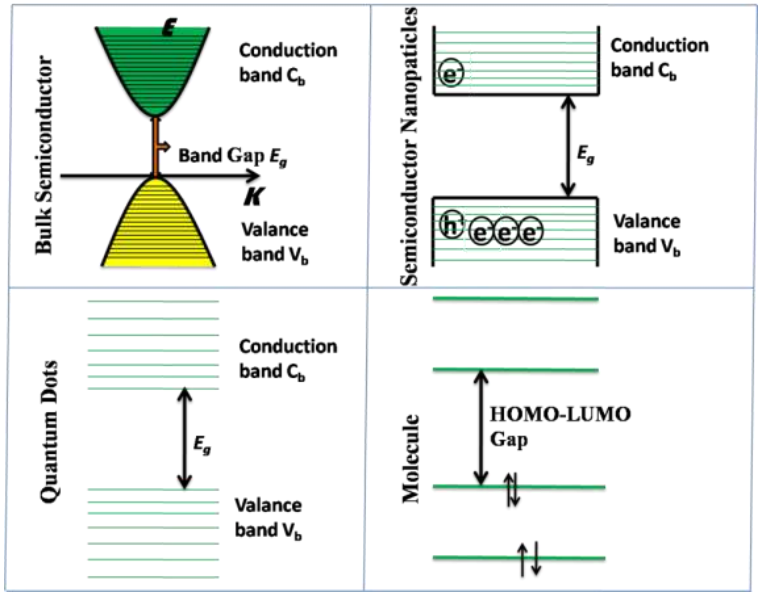

Figure 1.9: Energy bands of bulk semiconductors, semiconductor nanoparticles, quantum dots, and molecules.

The chemical composition, dimension of the layers, and the band gap energies vary the properties of QW. The confinement effect may be increased by nanostructuring as quantum wire and quantum dot. The width of the quantum well determines whether the confinement effect will be important. Usually, the carriers experience significant quantum confinement effects for well widths of order 100 A^o or less. The total number of discrete states depends on the well width and depth. In the case of wells with a finite height, the wave function does not vanish at the edge of the well, but decays exponentially in the classically forbidden (Figure1.9).The probability of finding a particle inside the well is always less than unity and decreases with increasing energy. As number of states are reduced then more confinement of the electron wave functions occurs , a part of the E(k) curve is replaced by discrete points as shown in Figure 1.10

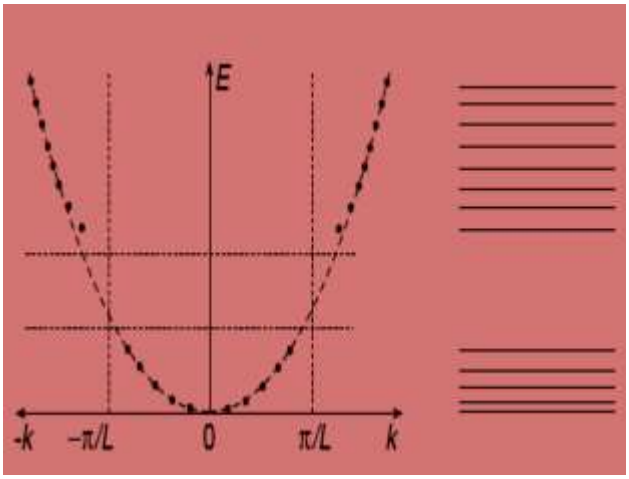

Figure 1.10: Due to the size-confinement of the semiconductor nanocrystal only the electron wave functions obeying R = nλ/2 can form standing waves; this and the reduced number of states lead to the formation of discrete energy levels instead of energy bands.

1.1.11 Theoretical models for describing quantum confinement effect

(i) Effective mass approximation

The effective mass approximation was extensively used to describe electronic motion in the presence of slowly varying perturbations. In a standard Effective mass approximation **(**EMA) model, electrons and holes are assumed to be non-relativistic spin less particles, behaving as free particles with their effective masses in a confining infinite spherical potential well, written as, in spherical coordinates (r,θ,φ) The effective mass approximation is based on the assumption of parabolic relation between the electron energy E and the wave vector k. The theoretical developments have been contributed by different authors; In general, the energy levels and wave functions can be obtained by solving the Schrödinger equation with a proper Hamiltonian [30-35]. Assuming that the many-body interactions among electrons are negligible, the motion of the electrons can be described by the one-electron Hamiltonian. The effective mass approximation for describing the band variation with size for nanocrystals, one needs to solve the Schrodinger equation for envelope function

$$\left[-\frac{\hbar^2\nabla_e^2}{2m_e^*}-\frac{\hbar^2\nabla_h^2}{2m_h^*}-\frac{e^2}{4\pi\varepsilon_0\varepsilon(r_{eh})}+V_0\right]\psi(r_e,r_h)=E\psi(r_e,r_h) \qquad \text{-------1.11}$$

where subscripts e and h refer to the electron and hole with m and r being the mass and position vector, respectively and r_{eh} =l r_e-r_h l ε_0 & ε are permittivity in vacuum and the relative dielectric constant of the material.

Assuming boundary conditions i.e. infinite potential outside the nanocrystals and zero potential inside, attempted to solve the equation (1.3) and proposed the following equation for the HOMO-LUMO gap of a Q-dot of radius R[30, 34, 36-38].

$$E(R) = E_g + \frac{\hbar^2}{2}\left(\frac{1}{m_e^*} + \frac{1}{m_h^*}\right)\frac{\pi^2}{R^2} - 1.786\frac{e^2}{\varepsilon R} \qquad (1.12)$$

where E_g is the band gap of the nanocrystalline semiconductor

The Brus model is an expression for the size dependent energy of the ground state of the electron-hole pair ($1s_e1s_h$ or first excited state), in which the second term describes confinement energy and the third the Coulomb electron-hole interaction. Some authors considered two limiting cases depending upon the ratio of the radius of the quantum dot to the Bohr exciton radius a_B of the bulk solid [34]

a. Weak confinement regime In this regime, electron-hole pair states consist of exciton bound states. The Coulomb interaction contribution to the exciton ground state should no longer be considered as a perturbation to the confinement energy, but is still treatable as a perturbation to the infinite confining potential well. However, the QD size allows a partial restoration of the long range Coulomb potential between the charged carriers, so that it is of the same order of magnitude than the kinetic energy in the electron-hole relative coordinates. Then, the leading contribution to the ground state energy of the exciton should be E^*, the ground state energy of a hydrogen-like atom of mass μ. Weakly quantized quantum dots (with $R \sim a_B$) enclose a large number of atoms; as a result Bragg reflection at the periodic lattice will lead to the formation of continuous energy bands. Only the levels at the top of the valence band and at the bottom of the conduction band, which correspond to the most delocalized electron wave function, will be discrete. Energy levels in bulk, macro particle and in nanoparticle have been shown in Figure 1.11. In this limit the character of exciton as a quasiparticle is well conserved. This is the regime

when the dominant energy is the Coulomb term and there occurs a size quantization of the motion of the exciton.

b. Strong confinement regime In this regime, the Coulomb potential is treated as a perturbation with respect to the infinite confining potential well in a variational procedure. In thse kind of semiconductor quantum dots energy levels are extremely quantised (with $R<<a_B$) and sometimes called artificial atoms because they exhibit a discrete optical spectrum determined by their size (see Figure 1.11(c)). The electron and hole, confined in a space with dimensions smaller than the Bohr radius of the exciton, hole and electron considered as dependent particles and occupy same eigen states of the quantum well. The Coulomb term is now small and can be either ignored of treated as a perturbation. The exciton mass is replaced by the reduced mass μ which is given by.

$$\mu = \frac{m_e^* m_h^*}{m_e^* + m_h^*}$$

Where m_h^* and m_h^* are effective masses of the electron and hole respectively. The EMA has been used to calculate the HOMO-LUMO gap for various semiconducting nanocrystals. For larger sizes of the nanocrystallites the infinite potential (IP)-EMA gives a good description of the HOMO-LUMO gap variation with size. However, it grossly overestimates the change in the band gap for smaller nanocrystals. Even though, Brus model does not describe the properties of real quantum dots explains the effect of quantum confinement. Some expansion in EMA with an infinite barrier was made when used a configuration interaction approach for the electron and the hole treating it like a two-electron atom [39]. They also used the Hylleraas functions and a perturbation expansion in R to obtain band gap energies slightly better than those described by the single particle EMA. The effective mass approximation while giving a good understanding of the blue shift of the optical absorption threshold fails to account for the size dependence particularly for small quantum dots. One of the reasons for the failure of the EMA is that the assumed parabolic E-k relationship may not be so in the small size regime. The screened attractive Coulomb interactions between electrons and holes absorb a phonon of appropriate energy [33-37, 40]. In small size regime ($\leq a_B$) the electron hole pair energy levels within a quantum dot cannot be treated using the Hydrogen atom model. The lowest energy level of the

exciton is now delocalized over the entire quantum dot [41]. The Coulomb interaction is completely neglected and the electron and hole are taken as free particle in a dot.

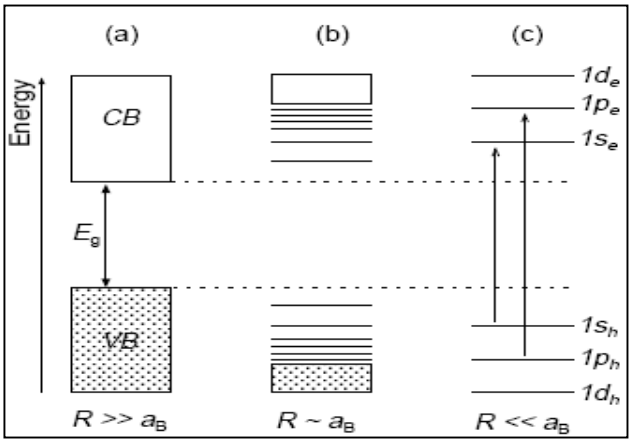

Figure 1.11: The effect of size on the electronic structure of a semiconductor crystal for three different size-ranges (a) a macro crystalline semiconductor ($R>>a_B$) with continuous energy bands; the filled valence band (V_B) and empty conduction band (C_B) and the bandgap energy (E_g) are shown (b) semiconductor nanocrystal with a weak size-quantization ($R\sim a_B$) (c) highly quantised dot ($R<<a_B$) with discrete atomic-like energy levels and optical transitions.

Additional improvements to the EMA led to the emergence of the multi-band EMA (MBEMA) theory. In most semiconductors the conduction band is non-degenerate and the electron effective mass can be well described by the single band theory. On the other hand, the top of the valence band is often degenerate. Hence, to describe the hole, one should consider various bands that contribute to the valence band edge. In CdSe nanocrystals, the size dependence of up to 10 excited states in the absorption spectra is successfully described by uncoupled MBEM [42, 43]. This includes the valence band degeneracy but does not couple the valence and conduction band. Wang et al & Nosaka et al were proposed the modification in "effective mass approximation" [44, 45].

(ii) Hyperbolic band model

Wang et al developed this model for PbS semiconducting nanocrystals [44]. The hyperbolic band model is used to overcome the shortcomings of parabolic band approximations. Pejova et al were also experienced this model in case of ZnSe nanocrystals [46]. In hyperbolic band model there

was approximations, according to first approximation, it is presumed that the lowest (in energetical sense) lattice excitation of a semiconductor of the binary type involves a charge transfer from the anion to the metal cation, at a cost in energy equal to the bulk band gap energy Eg. The second approximation to this model is that the hyperbolic band model for the calculation of the band gap energy accounts only for two relevant bands which at the point of the Brillouin zone (related to the band gap itself) correspond to the highest occupied valence band and the lowest unoccupied conduction band. On the basis of these assumptions, the following analytical formula has been derived for the size dependent band gap energy E(R) within the hyperbolic band model [44].

$$E_g(R) = \left[E_{gBulk}^2 + \frac{2\hbar^2 E_g \pi^2}{m_0 R^2} \frac{1}{2}\left(\frac{1}{m_e^*} + \frac{1}{m_h^*} \right) \right]^{1/2} \qquad (1.13)$$

Size dependent blue shift $\Delta E(R)$ predicted by hyperbolic band model were not significantly different for the one predicted by Brus model. In this model, the hole and electron bands are hyperbolic, but approach the parabolic behavior at the Γ point of the Brillouin zone. The main improvement of the hyperbolic band model with respect to the Brus model is the inclusion of the effect of electron and hole band non-parabolicity.

(iii) Tight binding approach

We consider now a regular lattice of atoms which are well separated such that their atomic orbitals have small overlaps only. Therefore, in a good approximation the electronic states are rather well represented by localized atomic orbitals, the tight binding approximation (TBA) approach utilizes the linear combination of atomic orbitals (LCAO) to calculate the electronic structure of periodic solids [47]. To calculate the eigen value spectra of nanocrystals one needs to know the ε's for the various orbitals and the t's for the interactions. The calculation of eigen value spectrum starts with the generation of the nanocrystal in real space by specifying the coordinates of the atoms. Then ε's and t's are assigned to the various orbitals and pairs of orbitals respectively, thereby generating the Hamiltonian matrix. The TB Hamiltonian matrix generated is then diagonalized to obtain the eign value spectra. This approach works well for

small sized matrices however diagonalization of the matrix becomes almost impossible for larger nanocrystal. The TB method was first used by Lippens and Lannoo to calculate the electronic structure of CdS and ZnS nanocrystals [48]. This method has also been used by several other researchers. Hill and Whaley employed a time-dependent TB approach to determine the electronic structure of CdS and CdSe nanocrystals [49]. They compared the effect of passivating CdSe surface with oxygen and removing the dangling orbitals. The TBA scheme has been employed by a number of researchers over the past decade, the parameters for CdS and ZnS used in the calculation are tabulated in table 1.2 [50].

$$\Delta E = a_1 e^{-\frac{R}{b_1}} + a_2 e^{-\frac{R}{b_2}} \qquad (1.14)$$

Table 1.2: Parameters used in TBA calculations.

Parameters	ZnS	CdS
a1	7.44	2.83
a2	2.35	8.22
b1	3.04	1.96
b2	15.30	18.07

Conde used sp^3s^* orbital basis TB method with the spin-orbit coupling for CdSe and CdTe nanocrystals [51]. The predicted blue shift with size obeyed $1/D^{1.42}$ dependence rather than $1/D^2$ relationship predicted by EMA. Another reports suggested, for zinc blende III-V and II-IV semiconductor nanocrystals was to use the nearest neighbor $sp^3d^5s^*$ TB model with the spin-orbit interaction included [52]. Such a model gives better description of electronic structure than sp^3s^* model. Electronic structure calculation using TB approximation and sp^3d orbitals for II-VI quantum dots was also reported by Sapra et al while incorporating the next neighbor interaction [53].

(iv) Empirical pseudopotential method

The band structure of CdS nanocrystals using the pseudo potential approach have calculated [54]. The calculated exciton energies of CdS clusters were in good agreement with the

experimental data over wide range of cluster sizes. Zunger et al employed the semi-empirical pseudo potential method to calculate the electronic structure of Si CdSe and InP quantum dots [55-58]. Unlike the EMA approach, this method based on screened pseudo potentials allows the treatment of the atomistic character of the nanostructure as well as the surface effects.

1.1.12 Semiconductor quantum dot materials

A quantum dot is a very small nanocrystal particle made of semiconductor materials that are small enough to show evidence of quantum mechanical properties and term "quantum dot" was originate by Mark Reed. When the excitons of that particular nanocrystal particle are confine in all three spatial dimensions. The electronic properties of these materials are intermediate between those of bulk semiconductors and of discrete molecules. Quantum dots were exposed in a glass matrix by Alexei Ekimov and Louis E. Brus were discovered colloidal quantum dots first time. These materials have some band gap and can be used to create fluorescent quantum dots. Quantum dots are typically made from II-VI and IV-VI groups' combination, such as CdSe, CdS, InP, and ZnS (Table II). Since the band gap of the material is extremely important to its properties, different materials are used when different properties are needed for an application. The first quantum dots were made primarily from II-VI semiconductors, such as cadmium and zinc chalcogenides. Semiconductor quantum dots refer to those semiconducting materials whose dimension lie in the nanometer range. The semiconductor quantum dots have great scientific and technological attention due to their possible application as luminescent applications in biological labels [59], quantum dot lasers [60, 61, and 1], and photo detectors [62]. Different semiconductor quantum dots with different type of combination with the values of excitonic Bohr radius have been listed in table 1.3. Most II-VI and IV-VI semiconductor materials have hexagonal wurtzite or cubic zinc blende form. A few of materials, for example ZnSe and CdTe, there is very little difference in energy between the zinc blende and wurtzite structures, and so they can exhibit combined behavior of wurtzite-zinc blende. Synthesis conditions provide the environment that may, these nanocrystals crystallize in either structure or both may coexist in the same nanoparticle. Lead chalcogenides crystallize in the rock salt structure, although it has been shown that CdSe quantum dots can also crystallize in this structure if the diameter exceeds 10 nm. For the most part, the choice of material for quantum dots is primarily focused on the optical properties of the material, but consideration also should be made for the preferred structure for

the application, toxicity (such as being free of heavy metals), and ability to coordinate ligands and functional groups to the surface.

Table 1.3: Calculated structures and type of band gap of II-VI and IV-VI semiconductors, bulk band gap E_g eV at 300^o K, lattice parameter in (A^0) and density (Kgm^{-3}) of semiconductor quantum dots.

Materials	**Structures and Type of Band Gap of II-VI and IV-VI Semiconductors**	**Bulk Band Gap E_g (eV) at 300^o K**	**Lattice parameter in (Å)**	**Density (Kgm^{-3})**
CdS	Cubic (Direct) Hexagonal (Direct)	2.42 2.53	5.832 6.710	4820
CdSe	Cubic (Direct) Hexagonal (Direct)	1.70 1.75	6.050 7.010	5810
CdTe	Cubic (Direct)	0.29	6.482	5870
ZnS	Cubic (Direct)	3.8	5.420	4090
ZnSe	Cubic (Direct) Hexagonal (Direct)	2.70 4.00	5.667 6.540	5266
ZnTe	Cubic (Direct)	2.39	6.104	5636
PbS	Cubic (Direct)	0.41	5.010	7597
PbSe	Cubic (Direct)	0.28	6.120	8260
PbTe	Cubic (Direct)	0.31	6.439	5219

1.1.13 Quantum dots stability factors

The critical issues that related to the quantum dot growth are size control stability and surface passivation. If the size of the quantum dot is small enough that the quantum confinement effects dominate, the electronic and optical properties are highly tunable. After the size, stability is the second important point in QDs formation. Because small Size QDs has very much high surface

energy and always trying to agglomerate to each other and this factor reduces the stability of the QDs. Temperature and environment also affect the stability of the QDs. So to maintain the high output, the QDs should be stable in all critical condition. Sometime QDs have contained some toxic materials, to stop the toxicity and maintain the size of QDs surface passivation is good way to protect the QDs.

(i) Size control: The properties of the quantum dots display size dependence behavior so it is necessary to control the size of the QDs with in a defined range. To control the size of QDs, it is necessary to optimize the growth rate concentration of stabilizing ligands precursor concentration and pH growth temperature etc. These all parameters affect the size of QDs at the time of formation.

(ii) Stabilization: Due to the small size QDs shows very high surface energy and the surface of QDs become more and more reactive. Besides this the smaller quantum dots have an inherent tendency to form larger agglomeration. Therefore by the use of some stabilization, QDs can be utilized according to the applications requirement. Generally two types of stabilization mechanisms are used to prevent agglomeration of nanoparticles: electrostatic stabilization and steric stabilization by adsorbed molecules.

(iii) Electrostatic stabilization: Electrostatic stabilization results from the interaction between the electric double layers surrounding the particles. Electrostatic stabilization of dispersion occurs when the electrostatic repulsive force overcomes the attractive van der waals forces between the particles. An unequal charge distribution always exists between a particle surface and the solvent. This method is very sensitive to the electrolyte concentration since a change in the concentration may destroy the electric double layer which will result in particle agglomeration [63].

(iv) Steric stabilization: Surfactant molecules can be absorbed on the surfaces of particles and their lyophilic chains will then extend into the solvent and repeling each other. Steric stabilization can occur in absence of the electric barriers. Steric stabilization is effective in both aqueous and non-aqueous media and is less sensitive to impurities or trace additives than electric stabilization.

(v) Passivation of surface states: The surfaces of quantum dots have many dangling bonds giving rise to a high density of surface states. These surface states interact very strongly with the electron/hole wave functions, produced radiative or non-radiative recombination processes at the surface of QDs. Obviously the optical and electrical properties unique to the quantum dot can be fully exploited only if the surface is passivated by a suitable material. Often the stabilization and passivation may be achieved by the use of an appropriate capping material, which is applied as a coating over the quantum dot.

1.1.14 Methods for synthesis of quantum dots

Nucleation and growth of QDs

Glass workers added cadmium, zinc sulfides and selenides to the melt to create glasses with rich yellow, orange, and red hues, producing very small concentrations of quantum dots. In 1980s, this process was controlled more directly, but still required very high temperatures and the control was very limited. So many other directions were developed by others researchers for quantum dot synthesis, especially focused on size control. QDs were synthesized by micelles, limiting their growth to the size of the micelle. Even as this method did not require high temperature, organic solvents, or complicated equipment, the size distribution was poor and the concentration was limited, as well as the quantum dots exhibiting poor crystallinity and a large degree of defects. The nucleation growth technique provides major breakthrough that made quantum dot synthesis easier and more controllable in high temperature. In nucleation and growth processes to make quantum dots, ionic sources of the constituent materials are needed, such as Cd^{2+}. QDs made of cadmium chalcogenides the reaction by the pyrolysis of organometallic precursors to produce monodisperse (less than 5% size dispersion). In this nucleation and growth process, an excess of organometallic precursors, such as dimethylcadmium and selenium-trioctylphosphine (SeTOP) were injected into a hot solution of coordinating solvent, such as a mixture of trioctylphosphine and trioctylphosphine oxide (TOP/TOPO) at over 280 °C, supersaturating the solution. During the first few seconds following the injection, particles nucleate homogeneously depleting the reactants, followed by particle growth, Ostwald ripening, and eventually saturation of the solution (Figure 1.12). This procedure was the first to result in quantum dots with sufficiently high quantum yield, between

10 and 20%, coordinated with organic ligands stabilizing the colloid, as well as producing monodispersity.

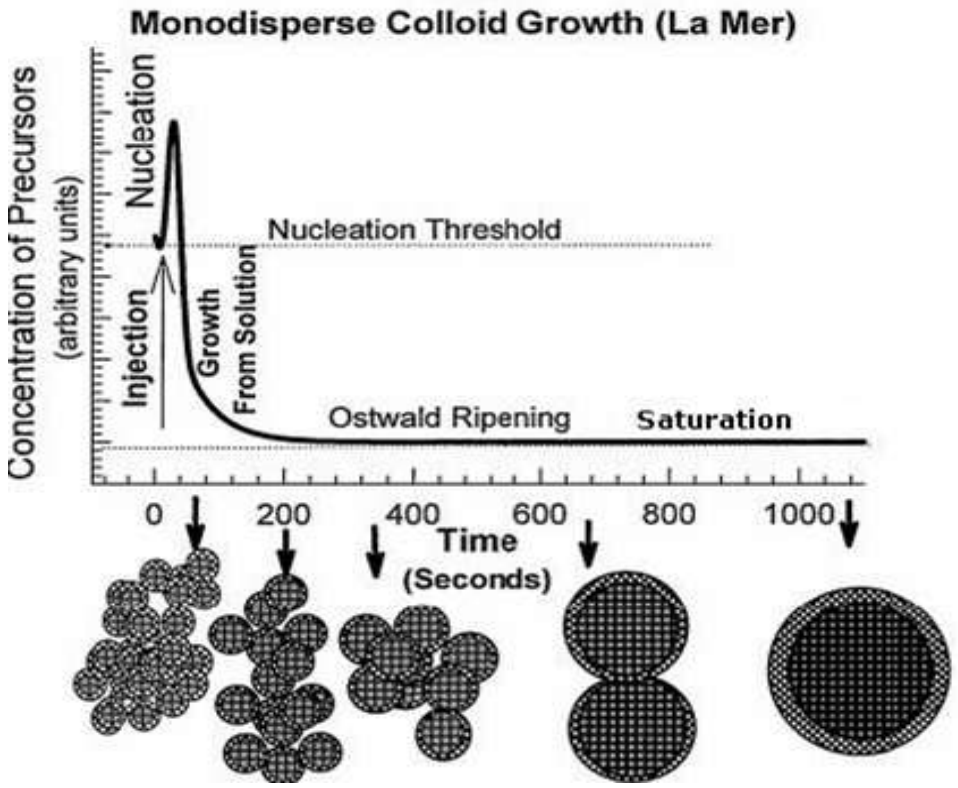

Figure 1.12: Nucleation and growth of nanoparticles in a solution of hot organic solvents.

There are various techniques for preparing wide band gap II-VI and IV-VI semiconductor QDs. Generally, these techniques can be categorized into two major classes: Chemical synthesis techniques and Physical synthesis techniques. Other procedures like Chemical bath deposition (CBD) and successive ionic layer adsorption and reaction (SILAR) are two well known in situ techniques and also can be used in large scale production. However, these techniques do not allow precise control of the particle size distribution of the QDs.

QDs can be produced using many different techniques, typically classified as bottom-up or chemical methods and top-down or physical methods. In the bottom-up approach, the structure of nanoparticles is constructed by atoms, molecules or clusters [64]. In top-down approaches, a bulk piece of a required material is reduced to nano sized dimensions using cutting, grinding and etching techniques, i.e., nanomaterials are prepared from larger entities

without atomic-level control [65], Chemical reduction [66], micro emulsion (colloidal) techniques [67], sonochemical reduction [68], electrochemical [69], microwave-assisted [70], and hydrothermal [71], syntheses are the main techniques for the synthesis of nanoparticles through the chemical approach. Biological or biosynthesis [72], techniques are also considered as bottom-up or chemical processes. Physical methods for nanoparticles synthesis are laser (pulse) ablation [73], vacuum vapor deposition [74], pulsed wire discharge (PWD) [75] and mechanical milling [76]. A wide range of nanoparticles can be produced using physical methods with little modification for different metals, but the main disadvantages of these methods are the quality of the product, which is interior compared to nanoparticles produced by chemical methods. Usually these methods require costly vacuum systems or equipments to prepare nanoparticles (plasmas). During the chemical synthesis process of the growth of QDs and morphology can be controlled by optimizing reaction conditions, such as surfactant's temperature and concentration, precursor, capping/stabilizing agent and the type of solvent. Using these optimum reaction conditions, a narrow size distribution during chemical synthesis can be achieved. Chemical synthesis methods are better than the physical synthesis method. Some chemical synthesis methods are discussing below:

(i) Controlled precipitation procedures

a. Arrested precipitation method

In this approach precipitation of the QDs may occur via either homo or heterogeneous nucleation as the ionic product exceeds the solubility product. The reaction parameters such as reactant activity, temperature, pH and the presence of catalyst need to be controlled to obtain a desired growth rate and particle size. The use of chemistry the preparation of materials can avoid three major problems - diffusion, impurities, and agglomeration." The reason being that the chemically prepared fine powder allows for only shorter diffusion distance and improved homogeneity, the chemical product can be easily refined to increase the purity and careful control of solvent removal from precursors will lead to the production of crushable agglomerate. However, the chemical preparative route generally involves more complex methods compared to the conventional ceramic routes and an improved level of skill is required for realizing the benefits. In an arrested precipitation method, often the reagents are mixed together by keeping in a

controlled atmosphere. The parameters like temperature, pH, concentration, etc. is to be controlled to control the nucleation rate and to eliminate the growth of the formed nuclei. The agglomeration of the particles can be eliminated by using a suitable stabilizer or capping agent. The capping agents are known to inhibit the growth of particles, since the polymeric chain is strongly bound to the metal ions near the surface of the QDs. This causes electrostatic repulsion between particles because of its charge. Moreover, this also helps in keeping the nanoparticles apart satirically because of the chain length. The controlled mixing of solutions containing the metal cations and the chalcogenide anions has been extensively used to generate small particles of II-VI semiconductors. A number of II-VI colloidal semiconductor quantum dots have been synthesized using this approach.

b. Organic stabilization method

The controlled development of ZnS and CdS semiconductor QDs were invented [Rossetti et al (1985)] [77] without using organic surfactant or by using stabilizers [Fojtik et al (1984) [78], Brus et al (1984)] [79]. A surfactant is usually added during growth of particles to control the size of QDs. The general approach is based on the chemical bath deposition technique reported by Chandra and Khare (1987) [80] for CdS. Brus et al (1984) [79] prepared CdS nanoparticles by mixing dilute aqueous solutions of $CdSO_4$ and $(NH_4)_2S$. Stable CdS nanoparticles with size 34 and 43 Å prepared by the use of acetonitrile, as a solvent, or the addition of styrene/maleic anhydride copolymer. Wageh et al (2003) [81] were formed ZnS QDs prepared by very small size particles of diameter 4 nm by mercaptoacetic acid as stabilizer. Karar et al (2004) [82] produced ZnS:Mn nanocrystals using polyvinyl pyroledone as capping agent. Tang et al (2005) reported water-soluble CdS nanoparticles using thio-glycollic acid as a cappent [83]. The absorption peak at 262 nm observed by them was attributed to ethylene-diamine modificated Cd-thiolate complex at the surface of as grown CdS nanoparticles. Self-organized cadmium sulfide quantum dots assembled using mercaptoethanol as a surfactant and varying the surfactant to thiourea ratio in the reaction matrix [84, 85].

c. Inorganic stabilization technique

In this approach, a solid A is grown on the surface of another solid B and later acting as a seed for the heterogeneous nucleation of the former. For this purpose presynthesized nanoparticle solutions are injected in to a reactant matrix containing precursors of the shell material. Growth of the shell of desired precursor occurs by heterogeneous nucleation over the injected nanoparticle surfaces. The core/shell structures so prepared can be finally stabilized using a suitable surfactant [86-96]. However, the relative solubility of the core/shell materials as well as lattice mismatch between the two phases restrains its use.

The preparation of structures of the type A/B/A termed as "quantum dot quantum well systems" are also interesting class of nanomaterials being investigated. CdS/HgS/CdS multishell QDS were prepared and reported with an interior of a CdS core, quantum well of HgS of 1-3 monolayers and a 1-5 monolayers of CdS as the outermost coating [21]. The synthesis involves the growth of HgS on CdS (52 Å diameter) by ion replacement, which is achieved by adding aqueous solutions of Hg $(ClO_4)_2$ to an alliquote of CdS particles. Substitution of Cd^{2+} for Hg^{2+} ions is thermodynamically favored, since the solubility products of CdS and HgS are $5x10^{-28}$ and $1.6x10^{-52}$, respectively. Also, there is a good match between the lattice constants for cubic CdS (5.818 Å) and cubic HgS (5.851 Å). Finally the re-precipitation of displaced Cd^{2+} ions on the surface of CdS/HgS particles is achieved by the drop wise addition of a dilute solution containing H_2S with the final particle diameter being estimated as 12 Å [97]. The band edge emission in CdS/HgS/CdS was reported to shift to lower energy values with increasing thickness of the HgS layer [21].

(ii) Sol-Gel

Sol-gel technology is a well-established colloidal chemistry technique, which offers possibility to produce various materials with novel, predefined properties in a simple process and at relatively low process cost. The sol is a name of a colloidal solution made of solid particles few hundred nm in diameter, suspended in a liquid phase. The gel can be considered as a solid macromolecule immersed in a solvent. The main benefits of sol–gel processing are the high purity and uniform nanostructure achievable at low temperatures. 2-7 nm ZnO nanoparticles by addition of LiOH to an ethanolic solution of zinc acetate have been prepared by some author [98]. A similar approach for synthesis of ZnO colloids was also used by Hilgendorff et al [99]. The absorption and

photoluminescence studies on CdS nanoparticles prepared using sol-gel technique reported [100]. The average radius of nanocrystals evaluated from the energy of the absorption edge and tight binding calculations was 1.5 nm. The applications of sol-gel derived products are numerous. Microscopic optical elements and active optical components as well as large area hot mirrors, cold mirrors , lenses and beam splitters all with optimal geometry can be made quickly and at low cost via the sol-gel route. This method have some drawbacks i.e., high cost, long processing times, volatiles production and development of stresses leading to fragmentation.

(iii) Sonochemical method

Sonochemical method is an attractive method for preparing novel materials with remarkable properties. The advantages of using sonochemical methods for sample preparation include high purity, narrow size distributions, controllable reaction conditions and the ability to form nanoparticles with uniform shapes and rapid reaction rate. This sonochemical processing method has also been proven to be useful in the preparation of CdS nanoparticles supported on sub-micrometric silica [101]. The ZnS nanoparticles prepared by this method typically have diameters of 1–5 nm and coat the silica surface as thin layers or nanoclusters, depending on the reactant conditions. Preparation of selenide nanoparticles such as ZnSe, CuSe, PbSe was described [102]. The formation, growth, and collapse of bubbles in a liquid following propagation of ultrasound drive the chemical reaction. In this method, a dispersion of a diacetate of the metal ions (Zn, Cu, or Pb) and selenourea was sonicated for 1 hr under argon atmosphere, while the temperature is gradually raised to 80^{o}C during the reaction. Ultrasonic processors that serve as homogenizers avoid agglomeration of particles to enhance stability and uniformity of a sample. Other major benefits of sonochemical reactions include as follows; Removal of contamination from soil and water, agglomeration potentially low possessing costs. It can be combined with bioprocesses and have good material as applications point of view.

(iv) Wet chemical /Solution growth method

This route used for producing nano and ultra-dispersed inorganic powders from aqueous and non-aqueous solutions. The term "wet chemical methods" emerged in contrast to conventional and solid-state synthesis methods of compounds and materials widely used also in ceramics

manufacturing. Today this term refers to a group of methods of powder and material production with liquid phase sol-gel process, hydrothermal synthesis, Pechini method, spray drying, aerosol spray pyrolysis, cryochemical synthesis, etc. The materials that formed by the wet chemical methods are possessing useful very usual properties like much smaller grains (crystallites) and, usually, lower temperature and shorter duration of phase formation.

The synthesis of nanoparticles is mostly covered by the two methods. First is the physical approach based upon vapour deposition and secondaly a chemical approach of solution phase synthesis. Solution or liquid phase syntheses requires the reaction of appropriate starting materials, e.g. the reduction of metal ions or the decomposition of a single organometallic precursor, in the presence of a surfactant or polymer that prevents the particles growing and aggregating into larger sizes. The nucleation and growth of the nanoparticles is depends upon the presence of the surfactant and the subtle manipulation of other reaction conditions including reaction time, temperature and concentrations. These conditions allows for control of nanoparticle size and shape, and thus properties. Among approaches to prepare nanocrystals, the direct solution chemical routes have widely been used for synthesis of semiconductor quantum dots because these methods allow us to create the quantum dots with a narrow size distribution. It is the most widely used method for the growth of single crystals, when the starting materials are unstable at high temperatures and also which undergo phase transformations below melting point [103]. Though the technology of growth of crystals from solution has been well perfected, it involves detailed work, much patience and even a little amount of luck. A power failure or a contaminated batch of raw material can destroy months of work. Materials having moderate to high solubility in temperature range, ambient to 100°C at atmospheric pressure can be grown by low-temperature solution method [104]. The mechanism of crystallization from solutions is governed, in addition toot her factors, by the interaction of ions or molecules of the solute and the solvent which is based on the solubility of substance on the thermo dynamical parameters of the process; temperature, pressure and solvent concentration [105]. The low temperature solution growth technique also allows variety of different morphologies and polymorphic forms of the same substance can be grown by variations of growth conditions or solvent. The proximity to ambient temperature reduces the possibility of major thermal shock to the crystal both during growth and removal from the apparatus. Growth of crystals from solution at room temperature

has many advantages over other growth methods though the rate of crystallization is slow. Since growth is carried out at room temperature, the structural imperfections in solution grown crystals are relatively low [106]. Among the various methods of growing single crystals, solution growth at low temperatures occupies a prominent place owing to its versatility and simplicity. After undergoing so many modifications and refinements, the process of solution growth now yields good quality crystals for a variety of applications.

1.1.15 Literature review of CdS and ZnS quantum dots

A number of reports on the synthesis and characteristics of nanocrystalline CdS & ZnS in aqueous medium have also been published [107-111]. The PL studies have generally exhibited long wavelength tails presumably due to size distribution and/or defects. Ravindran et al prepared Q-CdS by chemical capping method with thiophenol as capping agent using aqueous solution [112]. They studied the inhomogeneous broadening in the photoluminescence spectra of CdS nanoparticles. A band edge PL peak around 3 eV and a defect luminescence peak at 2.56 eV were reported by the authors. Benerjee et al synthesized CdS nanoparticles in the size regime of 0.7-10 nm using thiophenol as a capping agent [113].

A transformation from hexagonal wurtzite type structure to the cubic zinc-blende type structure was reported. The critical transformation size was about 4-5 nm. Results also indicated that the optical properties of nanocrystalline CdS are governed not only by the quantum confinement effects but also by the size induced structural phase transition. Two distinct absorption edges in CdS have been observed due to the presence of coexisting cubic and hexagonal phase. Wageh et al used mercaptoacetic acid as stabilizer to synthesize ZnS quantum-dots of diameter 4 nm [81]. The effect of refluxing time on the preparation of the samples was also investigated using UV-absorption and photoluminescence studies. Improved band edge emission was reported following use of larger refluxing time.

Photoluminescence enhancement and quenching for 580 nm emission induced by Zn^{2+} and Mn^{2+} introduction respectively in colloidal ZnS: Mn^{2+} nanoparticles has been reported [76]. The PL enhancement was related to the elimination of dangling bonds from the lone pairs on

surface S^{2-} anions. ZnS colloids that were rich in Zn^{2+} and poor in Mn^{2+} were reported to yield higher luminescence.

Milan Kanti Naskar et al describes the explanation the role of surfactants on the preparation of ZnS nanocrystals [114]. The non-ionic surfactants in the Span series, i.e. sorbitan monolaurate (Span 20) and sorbitan monooleate (Span 80) of hydrophilic–lipophilic balance (HLB) values of 8.6 and 4.3, respectively, have been used for the stabilization of emulsions. The role of these surfactants in controlling the size and properties of the ZnS nanoparticles has been discussed. A mechanism for the formation of TEA-capped ZnS nanoparticles from the surfactant-stabilized reverse emulsions has been proposed.

The mystery of non-heavy-metal ZnS quantum dots with bright blue photoluminescence by a one-step aqueous synthesis unlocked [115]. They examined the aqueous synthesis of non-heavy-metal ZnS quantum dots (QDs) using 3-mercaptopropionic acid (MPA) as the capping molecule at various pH and MPA:Zn:S ratios. At a lower pH (e.g. pH = 8), the room-temperature synthesized ZnS QDs exhibited no photoluminescence. Although further hydrothermal annealing at 100 °C could improve the photoluminescence of the ZnS QDs, the resultant emission was not as bright as that obtained at pH 12 at room temperature. The blue emission of aqueous ZnS QDs was likely the result of trap-state emissions involving the defect states of the QDs.

R. Seoudi et al (2012) [116] unfold the effect of the prepared temperature on the size of CdS and ZnS nanoparticle. Different nanoparticle sizes of cadmium and zinc sulfide were prepared by solvothermal route. The vibrational modes of CdS and ZnS were studied in the wave number range (600–150cm-1) using Fourier transform infrared spectroscopy

High quality manganese doped zinc sulfide quantum rods with tunable dual color and multiphoton emissions have been repoted by Zhengtao Deng et al (2011) [117]. Provide a versatile route to control the optical properties which may create new opportunities for photonic devices and bioimaging applications.

Jinzhong Niu et al (2012) [118] synthesized the CdS, ZnS, and CdS/ZnS core/shell Nanocrystals using dodecanethiol. A new route for synthesis of high quality of zinc blende CdS and ZnS nanocrystals. Solvent 1-octadecene, using dodecanethiol (DDT) molecules as both the

sulfur source and surface capping ligands. Only trap emissions of the nanocrystals were detected when the amount of DDT was excessive, this came from the strong quenching effect of thiol groups on the nanocrystal surfaces. After overcoating with ZnS shells, band-gap emissions of CdS nanocrystals were partially recovered.

Abbas Rahdar et al (2013) [119] studied the effect of 2-mercaptoethanol as capping agent on ZnS nanoparticles: structural and optical characterization. The effect of a capping agent on the structural and optical properties of nanocrystalline ZnS particles, which have been synthesized by co-precipitation method, has studied. Absorption spectra have been obtained using a UV-Vis spectrophotometer to find the optical direct band gap. Also found that the optical band gap (Eg) increases with the increase in molar concentration of the capping agent. This behavior is related to size quantization effect due to the small size of the particles.

Thanh Dinh Nguyen et al (2013) [120] provide a report on CdS QDs encapsulated in chiral nematic mesoporous silica. One-pot approach for liquid crystal self-assembly of semiconductor quantum dots into cellulose nanocrystal templated silica is developed. Subsequent removal of the cellulose template and organic stabilizers in the composites by controlled calcination generates new freestanding iridescent, luminescent chiral nematic mesoporous silica-encapsulated CdS films. CdS quantum dots undergo strong luminescence quenching when exposed to TNT solutions or vapor.

M. Taherian et al (2014) [121] recently studied the surface treated biocompatible ZnS quantum dots. The ZnS semiconductor QDs were successfully synthesized via an aqueous method utilizing glutathione (GSH), thioglycolic acid (TGA) and polyvinyl pyrrolidone (PVP) as capping agents. From photoluminescence spectra, it was found that the emission becomes more intensive and shifts towards the shorter wavelengths in the presence of the capping agent. Moreover, the emission mechanism of uncapped and capped ZnS was discussed in detail. Finally, the MTT results revealed the satisfactory (>94%) biocompatibility of GSH capped ZnS quantum dots which would be a promising candidate applicable in fluorescent biological labels.

Mark D. Peterson et al (2014) [122] explores the mechanisms for adsorption of methyl viologen on CdS QDs. The surface composition-dependent binding of the dichloride salt of

methyl viologen (MV^{2+}) to CdS quantum dots (QDs) enriched, to various degrees, with either Cd or S at the surface. Electron transfer-mediated photoluminescence quenching of the QDs by MV^{2+} serves as a probe for the binding affinity of MV^{2+} for the surfaces of the QDs. These findings suggest a strategy to maximize the adsorption of redox active molecules in electron transfer-active geometries through synthetic and post synthetic manipulation of the inorganic surface

1.1.16 Literature review of CdS/ZnS and ZnS/CdS core/shell systems

Inorganic stabilization technique with the development of nanostructures materials, one of the primary research goals, became to reach advanced properties and multifunctionality, in order to achieve better performances and novel applications. Logically, this has led to the discoveries of novel materials, but also brought the research attention to many other potential methods for combining two or more properties in one material. A very fine layer on small particles were found to substantially change their functionalities and properties, Up to now, concept of core/shell nanostructures has received a lot of research attention, bringing variety of solutions and systems with advanced properties. Even-though the motive for the investigation of various core/shell nano systems is different, this research field can be roughly classified into three perspectives. Most of the core/shell nanostructures are developed with the idea to combine two materials and thus two properties within one structure. Thus, the nano structure itself is characterized with the properties of both core and shell, offering variety of new possibilities and uncountable combinations. Such as, iron oxide nanoparticles covered with silica layer show magnetic properties arising from the core and luminescent optical properties arising from the shell. In this approach, a solid A (shell) is grown on the surface of another solid B (core). For this purpose pre-synthesized nano particle solutions are injected in to a reactant matrix containing precursors of the shell material. Growth of the shell of desired precursor occurs by heterogeneous nucleation over the injected nano particle surfaces. The core/shell structures so prepared can be finally stabilized using a suitable surfactant. Hines et al (1996) [94] described the synthesis of ZnS-capped CdSe semiconductor nanocrystals using TOPO/TOP by a two-step single-flask method. The efficiency of the ZnS capped clusters was shown to enhance dramatically alongwith a 50% quantum yield for band-edge luminescence. The fluorescence was also found to be stable over a period of months.

Liu et al (2000) [123] prepared CdSe nanoclusters over coated with CdS shell using mercaptoacetic acid as stabilizer. Band edge emission was found to red shift substantially with respect to absorption maximum. A model of formation of excimer with in nanoclusters was proposed to explain the large Stokes shift.

Optically detected spin and spin-orbital resonance studies of CdSe/CdS core/shell nanocrystals were reported by Gtozman [124]. Song et al (2001) [125] also reported synthesis and characterization of a highly luminescent (ZnSe) ZnS core/shell composite nanocrystals. The ZnSe dot surface was passivated with organic HAD/TOP. However no significant modification was observed by over coating the ZnSe dots with ZnS. Band edge luminescence was observed for both bare and coated ZnSe quantum dots.

Nikesh et al (2001) [126] used 1-thioglycerol as a capping material for synthesis of ZnSe quantum dots. Core/shell ZnSe/ZnS quantum structures were formed by growing a monolayer of ZnS or ZnSe nanoparticles. Both bare ZnSe and the corresponding core/shell were shown to exhibit absorption shoulder at the same wavelength. The optical absorption feature however got considerably broadened on coating ZnSe nanoparticles by ZnS. An increase in size distribution following coating by ZnS was assumed to give rise to the observed broadening. The relative PL quantum efficiency improved about 65% with respect to stilbene.

Valerini et al (2005) [127] investigated the photoluminescence properties of colloidal CdSe/ZnS core/shell Q-dots immobilized in an inert polystyrene matrix as a function of sample temperature in the range 45-295 K.

Zhao et al (2004) [128] reported electroluminescence and photoluminescence spectra of the CdSe/ZnS core/shell quantum dots covered by various organic ligands and incorporated into multilayered light-emitting diodes (LEDs).

The CdSe/ZnS core/shell system was one of the first type-I systems to be studied, and has been studied the most extensively (Figure 21). Due to the large difference in band gap between the CdS core (2.24 eV) and the ZnS shell (3.40 eV), the exciton is well confined to the core. The ZnS shell also passivates surface defects very well, greatly increasing the fluorescence quantum yield. Numerous reports are available regarding this method and analysis of core/shell QDs [129-

131, 87-96, 16, 3]. However, the relative solubility of the core/shell materials as well as lattice mismatch between the two phases restrains its use.

1.1.17 Literature review of multishell quantum dots

The preparation of structures of the type A/B/A termed as "quantum dot quantum well systems" are also interesting class of nanomaterials being investigated. CdS/HgS/CdS multishell QDS were prepared by using an interior of a CdS core, quantum well of HgS of 1-3 monolayers and a 1-5 monolayers of CdS as the outermost coating [21,132]. The synthesis involves the growth of HgS on CdS (52 Å diameter) by ion replacement, which is achieved by adding aqueous solutions of Hg $(ClO_4)_2$ to an alliquote of CdS particles. Finally the re-precipitation of displaced Cd^{2+} ions, on the surface of CdS/ HgS particles, is achieved by the drop wise addition of a dilute solution containing H_2S, with the final particle diameter being estimated as 12 Å [Towey et al (1990)] [133]. The band edge emission in CdS/HgS/CdS was reported to shift to lower energy values with increasing thickness of the HgS layer [Eychmu¨ller (1993) [21] & (1994) [132]].

ZnS/CdS/ZnS multishell quantum dots

In recent years, an increasing interest in semiconductor quantum well structures has led to the formation of physically and chemically prepared quantum well systems. The pioneering work of Mews et al. led to a variety of multishell QDs. The thickness of the core, well and the shell can be varied during the course of the synthesis. A chemical synthesis of multiple quantum wells in nanoparticle units could provide a low-cost pathway of preparation. Moreover, convenient handling of the quantum well units by wet-chemical modification and deposition from the solution at ambient conditions promises new applications. Recently, even more complex structures have been synthesized. In CdS/HgS/CdS/HgS/CdS double quantum well nanocrystals, two separated wells of HgS are embedded in CdS. A useful contribution to the structural analysis and complete description of such composite nanocrystals can be provided by photoelectron spectroscopy with tunable synchrotron radiation. By tuning the energy, it is possible to vary the surface sensitivity of the experiment and thus to reveal information about the nanocrystal surface and to analyze the composition of the nanoparticles as a function of depth.

Markus Braun et al (2001) [134] reported variation of the thickness and Number of Wells in the CdS/HgS/CdS multishell QDs on the first chemically prepared multilayer quantum well structure in a semiconductor quantum dot. The core and the capping material is also CdS. This system allows studying the interaction of quantum wells that are separated by different thicknesses of the CdS barriers. The radiative and relaxation dynamics of the new two-well system are compared with the dynamics of systems having a single-layer well and a double layer well system. Holger Borchert et al (2003) [135] also extended well like structure and repotted Photoemission Study of onion like multishell QDs.

Well Nanocrystals of CdS and HgS colloidally prepared CdS/HgS/CdS multishell QDs and CdS/HgS/CdS/HgS/CdS double quantum well nanocrystals stabilized with polyphosphates have been investigated by photoelectron spectroscopy with tunable synchrotron radiation. High-resolution spectra reveal in addition to a bulk species also a surface environment for CdS, where as different S species could not be resolved. Although a real layer thickness determination is not possible here anymore, the photoemission study at least supports the model of the double quantum well structure.

Reginald B et al (2001) [136] presented formation of multishell QDs hetero nanostructures with large lattice mismatch: ZnS/CdS/ZnS. Two-dimensional hetero structures have been exploited extensively in the synthesis of optoelectronic. The metastability of the ZnS/CdS/ZnS hetero nanostructures is attributed to low-temperature construction and small crystal size ~3 nm. The small particle size should produce large surface forces and ZnS core contraction. Also, the small particle size should accommodate strain, as a result of the ZnS/CdS interfacial curvature, which is not possible for planar systems. Furthermore, this new structure is kinetically stabilized against alloying by the large size difference between the Cd ion and Zn ions. David Battaglia et al (2003) [137] described colloidal two dimensional CdSe quantum shells and wells the experimental results of the inorganically passivated quantum shells reveal that even more complex systems can be conveniently built with the SILAR technique. High quality quantum shells and colloidal quantum wells are optically comparable to high-quality quantum dots and rods, with reasonably high PL quantum yields (over 20% for the CdSe quantum shells and over 40% for the CdS/CdSe/CdS colloidal quantum wells), relatively narrow emission bands, and tunable emission colors from about 520 to 650 nm.

Lixin Cao et al (2004) [27] presented a new method for ZnS/CdS/ZnS multishell QDs. ZnS/CdS/ZnS quantum dot quantum well was prepared in micelles successfully and was characterized by absorption spectroscopy and fluorescence spectroscopy. Luminescence in the region of 350–600 nm was observed. The luminescence from CdS was enhanced by the complete ZnS shell, which may be the result of the decrease in the defects on the surface of the CdS well, which were assumed to act as centers for radiation less recombination.

Lixin Cao et al also encored (2005) [28] the effect of layer thickness on the luminescence properties of ZnS/CdS/ZnS multishell QDs was prepared. The optical properties of ZnS/CdS/ZnS multishell QDs with different thickness of CdS well and ZnS shell were studied. The luminescence enhancement was caused by the relative reduce in the surface effect. The optical properties of ZnS/CdS/ZnS multishell QDs with different thicknesses of CdS well and ZnS shell were studied. Luminescence at 520 nm can be assigned to the bulk donor–acceptor recombination of the CdS. Increasing the thickness of the CdS well could lead to the enhancement of the luminescence. The luminescent intensity first increases and then decreases slightly with the ZnS shell thickening.

A. SalmanOgli et al (2011) [138] Investigation of electronic and optical properties of (CdSe/ZnS/CdSe/ZnS) multishell QDs. They probed the effect of carrier localization in layers of hetero nanocrystal on the photoluminescence intensity. Moreover, the effects of variation of radius layers such as CdSe core, shell, and ZnS barriers radius on the photoluminescence intensity are studied. Furthermore, by alteration of the shell radius of CdSe, the photoluminescence intensity severely decreased and we revealed that the relation of these decrements is because of trifle localization of carriers in the core region and small amount of overlapping between electron–hole pairs probability distribution.

Hua Qu et al (2011) [139] exposed the enhanced photoluminescence and post irradiation luminescence is reported from Ag^{+} doping ZnS/CdS/ZnS multishell QDs prepared via a reverse micelle process. Controlling the final mole ratio of water-to-surfactant in H2O/Heptane system, the size of a multishell QDs was estimated to be 6 nm. The quantum yield was increased from 2.63 to 9.31%, and the remaining luminescence intensity after 2 h ultraviolet irradiation was

increased from 71.2 to 94.7%. This improved quantum yield and post irradiation luminescence intensity for doped multishell QDs was ascribed to the introduction of Ag ions to CdS wells.

G. Murugadoss (2012) [29] introduced water soluble ZnS, CdS and multilayer coated ZnS/CdS/ZnS nanocomposites were successfully synthesized by chemical method in an air atmosphere. A significant red shift was observed by increasing the CdS thickness in ZnS/CdS/ZnS nanocomposites. The PL position of ZnS and CdS compound is tuned in the visible region by the way of alteration layer thickness. Manipulation of optical properties in these systems can be exploited for the fabrication of optoelectronic devices and designing of fluorescent sensors.

Xianghua Zeng et al (2014) [140] described charge transfer and optical properties of wurtzite-type ZnS/(CdS/ZnS)n (n = 2, 4, 8).The prepared samples with an average thickness of 30 nm for ZnS layer and 60 nm for CdS layer have a wurtzite- type structure. wurtzite-type ZnS/(CdS/ZnS)n (n = 2, 4, 8) super lattices have successfully prepared on sapphire substrate by pulsed laser deposition (PLD) at a low growth temperature of 100 8C. For these ZnS/CdS super lattices, the mismatch between their lattice parameters is only 3.0% regarded as the recombination of surface defects states to valence band of ZnS, and the emission band at 577 nm as the recombination of Cd–Cd centers, the strong emission at 496 nm is from the charge transfer of electrons from CdS electron to ZnS holes by excitation energy. Therefore, ZnS/ $(CdS/ZnS)_n$ super lattices are a promising optical material in the applications to various transparent green optoelectronic devices.

1.1.18 Literature review of PbS, PbSe quantum dots and PbSe/PbS core/shell quantum dots

Quantum dots of lead chalcogenides take up a unique place in the family of compound semiconductors. However, the relatively large Bohr radii of these materials (18-46 nm) compared to cadmium systems (4-10 nm), places them in the so-called “strong confinement” regime. In this domain, shape and size effects produce extreme changes to the physical and chemical properties, relative to the bulk. Consequently, these materials have found applications in many devices including, sensors, photometers, remote sensing of gaseous pollutants in trace gas sensing devices for analysis of toxic gases, for human breathe analysis in medical

diagnostics, electroluminescent devices non-linear optics, window coatings and thermoelectric. Recently, multiple exciton generation for PbX (X = S, Se, Te) QDs has been suggested and demonstrated experimentally with potential to lead to an entirely new paradigm in high efficiency and low cost solar cell technology. The significant features of lead chalcogenide QDs in comparison with other compound semiconductors are as follows:

1. In lead chalcogenides both valence band maximum and the conduction band minimum occur at the L points of the Brillion zone.
2. This unique feature along with small energy band gap leads to strong effective masses of electrons and holes and strong spin-orbit interaction. The band gap of IV-VI binary system depends on temperature.
3. The band gap of lead chalcogenides is also sensitive to hydrostatic pressure.
4. It decreases with the increase in hydrostatic pressure and vice versa. Lead chalcogenides can act as p-type or n-type semiconductor.
5. This property depends on the lattice structure of ultimately formed materials.

The vacancies and interstitial sites induced by the excess of either lead or chalcogenide controls the type of conductivity; an excess Pb^{2+} causes n-type conductivity and an excess of chalcogenide cause p-type conductivity. The dielectric constants of IV-VI binary system is unusually high as compare to other semiconductors. Important properties of bulk lead chalcogenide are given in table 1.4.

Joo et al synthesized the QDs of PbS using lead-oleylamine complex, prepared by the reaction of $PbCl_2$ with oleyamine at 90^{o}C resulting mixture was heated to 220^{o}C for 1h to produce PbS dots. The size of nanoparicles can be adjusted by simply varying the amount of starting materials. Highly luminescent PbS nanoparticles with quantum yield ~ 20% have band gaps tunable throughout the NIR region are also reported from a reaction between lead oxide and bis(trimethylsilyl)sulfide (TMS). The spectra of PbS QDs with a 1S transition spanning the range of 800–1800 nm are presented as well as narrow emissions with small Stoke shifts. A modification in the preparation of narrow size monodisperse particles of metal-chalcogenide by thermolysis is to employ single-source precursors in a suitable co-coordinating solvent. This approach provides both elements within a single molecule which allow the preparation of

semiconductor nanoparticles in one step. Different precursors such as dithiocarbamates, dithiophosphinates and thiobenzoates have been used to prepare PbS QDs.

Table 1.4: Selected physical properties of lead chalcogenides

Properties	**PbS**	**PbSe**
Bohr radius (nm)	18	46
Band gap (373K)(eV)	0.41	0.29
Density (g/cm^3)	7.6	8.3
Dielectric constant	169	204
Structure	Cubic	Cubic
Lattice spacing (A^o)	5.936	6.124

Vital et al have synthesized PbS particles by employing lewis-base catalyzed approach to decompose metal alkyl xanthates by using alkyl amines as a solvent to promote decomposition as well as capping ligand for the particles formed. Spherical PbS QDs of diameters 5-10 nm were obtained when long chain alkyl amines were used. Once bi-functional ethylenediamine was used instead, PbS dendrites were isolated from the same precursor at room temperature. Uniform six and four-armed dendrites were observed, with regular branches of ~20 nm in diameter.

Cheon et al have provided some close into factors underlying the ripening observed with the PbS QDs from a single-source precursor. By varying the injection temperature, the shape of the resulting particles evolved from rods to multi-pods to cubes. By varying the ratio of dodecanethiol ligand to the single-source precursor, the shape can be tuned from nearly spherical to tetra decahedrons to almost cubic.

Recently, decomposition of lead hexadecylxanthate on TOA has been reported to yield ultra narrow rods with diameter of ~ 1.7 nm and length of 12-15 nm. The strong quantum confinement is observed in the absorption and photoluminescence spectra. The absorption spectra is strongly blue shifted and indicates sharp excitonic band at 278 nm and a shoulder at 365 nm. These bands are of excitonic origin corresponding to 1Pc to 1Ph, 1Sc to1Ph, and 1Sc to

Sh transitions. The PL spectrum shows strong and sharp band-edge emission at 410 and 434 nm along with a shoulder at 465 nm, and a weak band at 500 nm.

Carlo Giansante et al (2014) [141] announce surface chemistry of arenethiolate-capped PbS quantum dots and application as colloidally stable photovoltaic ink. Consequently, smooth dense-packed thin-films of arenethiolate-capped PbS QDs obtained via a single solution-processing step are integrated in hetero junction solar cells: such devices generate remarkable photocurrent densities (14 mA cm^{-2}) and overall efficiencies (1.85%), which are outstanding for a single PbS QD layer.

Minwoo Nam et al (2014) [142] exposed the two strategies to enhance efficiency of PbS quantum dot solar cells: Removing surface organic ligands and configuring a bilayer hetero junction with a new conjugated polymer. The charge separation and subsequent transfer dynamics were examined, as were the resultant photovoltaic characteristics, according to the kind of polymer used. This indicates that the proposed techniques are very useful for improving the efficiency of inorganic QD-based solar cells.

The QDs of PbSe has also potential applications in thermal imaging and infrared detectors, operating at wavelengths between 1.5-5.2 μm. It does not require cooling, but performs better at lower temperatures. The peak sensitivity depends on temperature and varies between 4.0-4.7μm. PbSe nanocrystals have been prepared by a number of methods. Free-standing PbSe nanocrystals, including quantum wires, multipods, quantum rods, quantum dots, and cubes, were produced in a colloidal solution in the presence of alkyl-diamine solvent at 10−117 °C. Nanocrystal hetero structures represent unique systems in which the optical and electronic properties can be tuned by varying the chemical composition of their components and their mutual distance.

Esteban Pedrueza et al (2013) [143] studied the effect of quantum size confinement on the optical properties of PbSe QDs as a function of temperature and hydrostatic pressure. Study based on photoluminescence and absorption measurements as a function of temperature and pressure for PbSe QDs with sizes in the range 3–13 nm reveals the influence of size quantum confinement on the observed variation. The pressure variation is a clear inverse correlation

between the absolute value of the pressure coefficient and the nanocrystal size, a signature of quantum size confinement.

Ju Young Woo et al (2014) [144] recently repotted ultra stable PbSe QDs via in situ formation of atomically thin halide allayers on PbSe. The fast degradation of lead selenide (PbSe) QDs in ambient conditions impedes widespread deployment of the highly excitonic, thus versatile QDs. Conductive films made of halide-treated ultra stable PbSe QDs exhibit markedly improved air stability and behave as an n-type channel in a field-effect transistor. The wet chemical passivation scheme will enable broader utilization of PbSe QDs in ambient conditions in many optoelectronic applications.

In one study, formation of PbSe/PbS and PbSe/$PbSe_xS_{1-x}$ core/shell QDs with luminescence quantum efficiencies of 65% is reported. These structures showed chemical robustness over months and years and band-gap tunability in the near infrared spectral regime, with a reliance on the QDs size and composition. The fluorescence line-narrowing (FLN) spectra of these QDs indicate a negligible reduction of the full width at half-maximum (FWHM) of the resonance PL band with respect to the FWHM of the no resonance PL band, suggesting the minor contribution of an inhomogeneous broadening due to a size distribution. While Lifshitz et al reported the successful synthesized the PbSe/PbS QDs recently, a tributylphosphine/trioctylphosphine (TBP/TOP) ligand-based synthetic approach was adopted in their work, which produced PbSe cores of lower quantum efficiency(~40%) and less size-tunability (1.2–5.0 nm) than those prepared with the oleate ligand-based approach (~85%, 2–13 nm). In addition, no attempt was made to investigate the ligand dependence, chemical stability and processibility of the PbSe/PbS core/shell NQDs. The technique of successive ion layer adsorption and reaction (SILAR) [145], originally developed for the deposition of thin films on solid substrates from solution baths, has been adapted to the growth of high-quality PbSe/PbS core/shell nanocrystals. While Li et al has introduced the SILAR approach to the growth of wider band gap shells over II–VI NQDs (CdSe/ZnS) with the impressive success [146], it takes effort to apply the SILAR technique to the IV–VI NQD system due to the different compound families and coordinating ligands involved in the synthesis.

Recently, high quality PbSe/PbS core/shell and completely original PbSe/PbSexS1-x core/alloyed shell QDs structures were produced using a single injection process, offering the potential to tailor the crystallographic and dielectric mismatch between the core and the shell, forming a perfect crystalline hetero-structure. These structures present higher photoluminescence (PL) with respect to those of core/shell QDs and tunability of the band-edge offset with variation of the shell thickness and composition, eventually controlling the electronic properties of the QDs. During the past few years, considerable interests have been focused on the thermally activated processes of the ground-state exciton emission of PbSe core QDs. This study also shows that the temperature coefficient of the energy gap and the optical phonon coupling were reduced with the decrease of the diameter, while the acoustic phonon coupling grew with the decrease of the diameter. Since the first report of experimentally prepared PbSe/PbS core/shell QDs, some simple physical properties, such as electronic structure had been studied. The previous theoretical work predicted a variation of the electronic structure of PbSe/PbS core/shell QDs, pronounced in the variation of the carriers' radial distribution function, with the variation of the core radius/shell-thickness ratio, showing a significant separation of the electron and hole wave functions only when the shell-thickness becomes equivalent or larger than the core radius.

However, the electronic structure and optical properties of colloidal IV-VI quantum dots, composed of core/shell hetero structures with alloy components still lack systematic and in depth study.

Jian Xu et al (2006) [147] were explaining synthesis and surface modification of PbSe/PbS core/shell nanocrystals for potential device applications. The growth of PbS shells over colloidal PbSe QDs with monolayer-precision. The technique of successive ion layer adsorption and reaction (SILAR) has been adapted to the growth of high-quality core/shell nanocrystals. The reported results open up the possibility of incorporating semiconductor infrared QDs in the silicon matrix to develop all-inorganic light-emitting hetero junctions on silicon substrates.

A. Sashchiuk et al (2002) [148] described synthesis and characterization of PbSe and PbSe/PbS core/shell colloidal nanocrystals by a new colloidal procedure, for the synthesis of PbSe and PbSe/PbS core/shell semiconductor nanocrystals. (QDs), is reported. The synthesis

includes the reaction between tributyl-phosphine. HRTEM showed the formation of PbSe/PbS core/shell structures, with epitaxial shell layer with thickness varying between 1 and 4 ML. The last effect can be due to an electronic mixing of the PbSe and PbS conduction states. The PL measurements showed a substantial increase of the exciton emission in the core/shell structures, arising by an efficient chemical passivation of the PbSe core. This advanced synthesis of the colloidal PbSe QDs, and PbSe/PbS core/shell QDs capped with organic ligands as well as the solid thin films of these QDs is potentially useful for application in opto-electronic devices.

Jan W et al (2007) [149] exposed about the photo stability of colloidal PbSe and PbSe/PbS core/shell QDs in solution and in the solid state. The photo stability of semiconductor PbSe nanocrystals (QDs) under different storage conditions and the photoluminescence of PbSe nanocrystals films on Si substrates under vacuum and under different atmospheres were investigated. This blue shift is accelerated when the particles are stored in room light compared to when the particles are stored in the dark, which indicates that photo oxidation is an important process. To improve the photo stability of PbSe QDs, PbSe/PbS core/shell QDs using (TOP) trioctylphosphine) and TMS2S (TMS2) bis(trimethylsilyl)) as sulfur sources were prepared. However, PbSe/PbS core/shell QDs did not show an increased stability in solution upon irradiation with a xenon lamp when compared with PbSe core QDs. Either the PbS shell is not able to confine the charge carriers or there is incomplete shell passivation with the PbSe core, and as a result these core/shell QDs have comparable stability.

Diana Yanover et al (2014) briefly repotted temperature dependent recombination processes in small sized PbSe/PbS core/shell colloidal quantum dots [150]. The work focused on the optical investigation of temperature-dependent recombination processes in small-sized PbSe/PbS core/shell QDs with core diameter of (2 – 2.5) nm and the shell thickness of (0.5 – 1.0) nm under air-free conditions and after air exposure. The PbSe/PbS core/shell QDs are oxidation-stable towards time-limited air exposure. PbSe/PbS QDs have relatively narrow emission bands, a longer excited-state lifetime at low temperatures and higher tolerance to oxygen exposure for a limited period of time as compared to the corresponding PbSe core/shell QDs.

Diana Yanover et al (2014) [150] also reported significance of small sized PbSe/PbS core/shell colloidal QDs for optoelectronic applications The PbSe/PbS core/shell structure were

synthesized by a specially developed wet-chemistry method. Their electronic properties were determined by the comparison of theoretical calculations with continuous-wave and transient photoluminescence measurements conducted at various temperatures. The results revealed the formation of quantum dots characterized by a tunable band gap around 1 μm, lifetime exceeding 4.0 μs at room temperature, photoluminescence quantum yield >60% and resistance to oxidation for a relatively long period of time.

1.1.19 Applications of semiconductors quantum dots

Our technological modern life would not be possible without the semiconductor industry. Semiconductor nanocrystals, also known as quantum dots (QDs), have become an indispensable tool in biomedical research, especially for multiplexed, quantitative, long-term fluorescence imaging and detection [151-154]. Recent advances in nanoparticle surface chemistry have led to the development of polymer-encapsulated probes that are highly fluorescent and stable under complex biological conditions [155-157]. This new generation of water-soluble QDs solved the problems of quantum yield decrease, chemical sensitivity and short shelf-life previously encountered by the ligand exchange-based QD solublization method [158]. As a result, these particles, linked with bio affinity molecules, have raised new opportunities for ultrasensitive and multicolor imaging of molecular targets in living cells and animal models [159, 160].

Therefore, for nano-carrier development and optimization, QDs can become an excellent ‘prototype’, from which bio-compatible carriers of similar sizes and surface properties can be made for clinical uses. Current applications of QDs in drug delivery are focused on two major areas: using QDs as carriers and labeling therapeutics or drug carriers with QDs.

Besides their contribution in technological important devices, semiconductors also provided platform to explore fundamental questions of physics. Quantum Hall effect (QHE), tunneling effect (TE) and multiple exciton generation (MEG) are some noteworthy processes that have been studied in semiconductor structures. Figure 1.13 presents applications of various nanoparticles in diverse fields of applications at a glance.

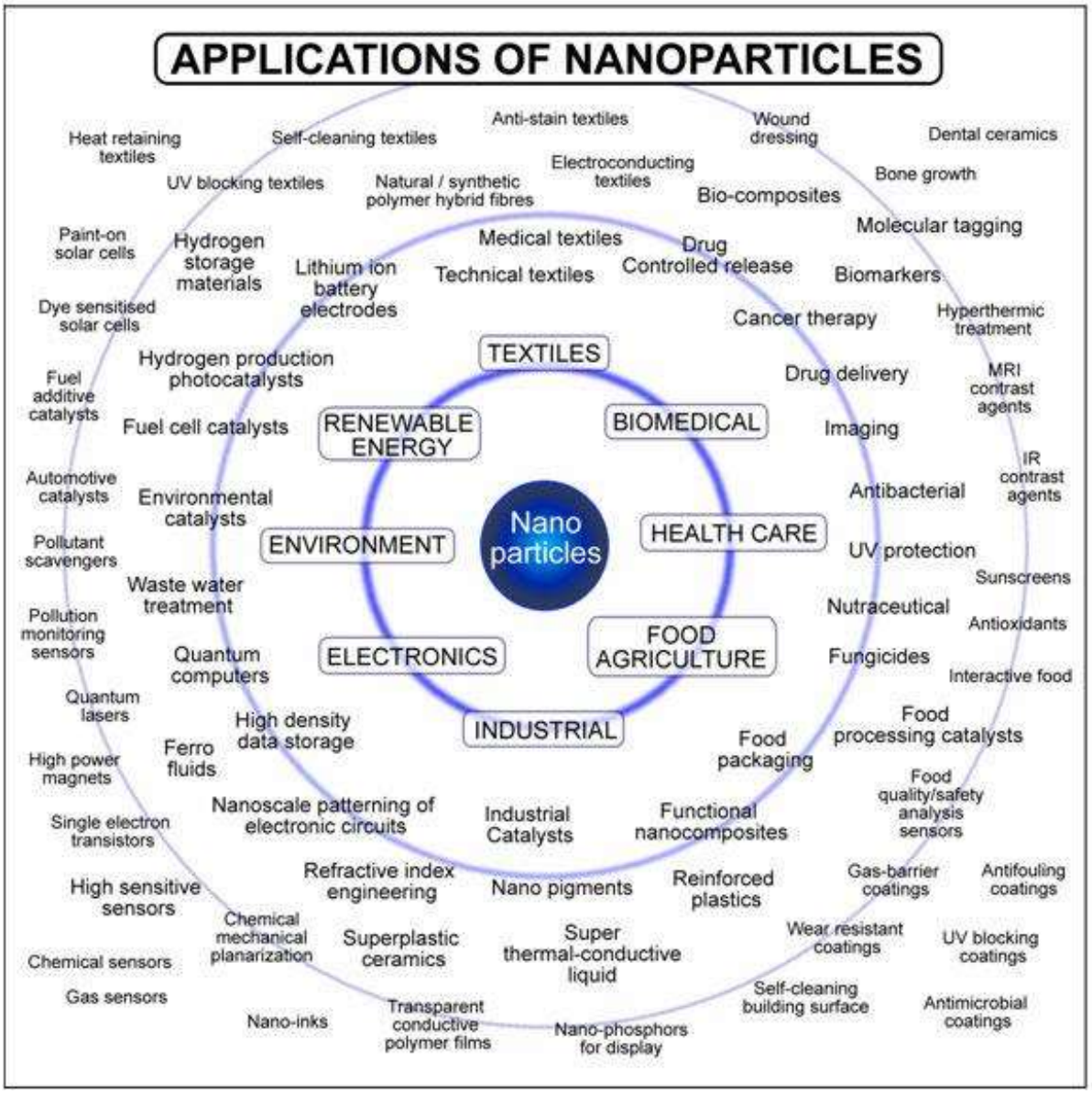

Figure 1.13: Presents applications of various nanoparticles in diverse fields of applications at a glance. http://www.nanowerk.com/nanotechnology-applications.php

1.1.20 Some specific applications of QDs in different fields

Nanocrystals of metals and semiconductors have potential applications in a number of fields including, in energy and power, health and biomedicine, electronics and computers, environmental applications, new engineering materials, consumer goods, personal care products, food and transportation. To perform these functions nanocrystals have to be synthesized,

passivated to control their chemical reactivity, stabilized against particle aggregation and functionalized to achieve specific performance goals [161-165].

(i) Photovoltaic devices

An increased attention is being directed towards the manufacture of efficient, low cost, large-area coverage and flexible photovoltaic modules. Since the first report of a QDs PV device attention has been focused on absorber optimization using quantum sized rods or tetrapods [166, 167]. However, less attention has been paid towards the infrared photovoltaic considering half of the sun's power reaching the surface lies in the infrared region [168]. One strategy for hybrid solar cells is to use blends of inorganic nanocrystals with semi conductive polymers as a photovoltaic. In 2004, Sargent and co-workers reported the photoconductivity in a nanocomposite containing a sensitized polymer poly [2-methoxy-5-(2'-ethylhexyloxy-*p*phenylenevinylene)] (MEH-PPV) with PbS QDs [169]. However, the system had a low internal quantum efficiency of 10^{-5}. Later, the same group has reported a three-order-of magnitude improvement in infrared photoconductive internal quantum efficiency of a solution-processed device [170]. This was also the first time that an infrared photovoltaic effect is observed in such devices. In another study, Zhang et al; have demonstrated a bulk hetero junction hybrid solar cell containing MEH-PPV blend and octylamine capped PbS QDs (λ abs = 935 and 1300 nm) [171]. This is a possible result of charge carriers being able to tunnel through the ligand barrier or to transfer directly from the polymer to NC structure sites left free by incomplete ligand exchange process. The device exhibited short-circuit current (250 nA) and an open circuit voltage (0.47eV). A bilayer photovoltaic device containing butyl amine capped PbS QDs (λ abs = 1260 nm) and poly-3(octylthiophene) (P3OT) showed an internal quantum efficiency of 11.3% and an external quantum efficiency exceeding 1% for a infrared photovoltaic response at λ = 720 nm. The overall power conversion efficiency of the device was, however, not reported [172]. In 2007, Klem *et al.* have reported hybrid photovoltaic devices infrared power conversion efficiencies of 1.3% [173]. Here in, the authors have used ethanedithiol as a multiple cross-linker and high-temperature sintering processes to achieve smooth films on rough ITO surfaces. Planar Schottky photovoltaic devices have been prepared from solution processed PbS QDs films with aluminum and indium tin oxide contacts [174]. These devices exhibited up to 4.2 % infrared power

conversion efficiency. More recently, hybrid bilayer photovoltaic devices based on PbS QDs on ITO substrates covered with a poly (3-hexythiophene-2,5-dilyl) (P3HT) layer has shown to enhance the interfacial layer and improve charge carrier separation and mobility, yielding better performing solar cells.[175] In 2006, Cui and co-workers have reported a bulk hetero junction solar cell containing oleic acid capped PbSe QDs in a P3HT matrix [176]. The device exhibited photovoltaic response only after being subjected to the strongly bound bidentate linker, benzenedithiol as it offers passivation of dangling bonds.

(ii) Light emitting diodes

Nanocrystals of semiconductors are useful materials to be used in Light emitting diodes (LED). Nanocrystals (LEDs) offer substantial advantages over organic LEDs (OLEDs) which make use of organic fluorophores to emit radiation. This is because OLEDs have poor photo stability and short lifetimes relative to nanocrystals LEDs. Significant cost [177] savings can be realized in the production of high quality white light from nanocrystals LEDs over OLEDs.

(iii) Biological applications

Nanocrystals of metals and semiconductors have received considerable interest due to their applications in the biological world [178]. Important applications include: fluorescent biological labels, drug and gene delivery, detection of pathogens, probing of DNA structure, tissue engineering and cancer detection. The use of nanocrystals as fluorescent biological labels is one of major application. Traditionally, organic dyes have been preferred materials for such type of applications. Infrared emitting nanocrystals (lead chalcogenide) are suitable materials for such applications. In the past few years, near-infrared (NIR) fluorescence imaging techniques have emerged that enable in vivo imaging of physiological, metabolic, and molecular function. The NIR window, also known as the diagnostic window (700–900 nm), can be explored for sensitive detection techniques. Nanoparticles, particularly semiconductor QDs of IV-VI group can be utilized for the purpose of optical imaging. NIR QDs with unique properties can be utilized as contrast agents for optical imaging, particularly for deep tissue imaging. Deep tissue imaging provides more information about the pathological status of the ability to simultaneously

distinguish emission profiles of multiple near-IR QDs will likely emerge as important tools for addressing fundamental questions in molecular biology and in medical sciences.

Table 1.5: Listing of the diverse reports on the applications of the QDs in different fields.

QDs	Applications	Research groups	References
CdS	Detection of acetylcholinesterase activity and inhibitors	G. Ibabe et al	doi: 10.1039/c3an01662e. Epub 2013 Nov 14
CdS	Precision optical bioimaging	S. Veeranarayanan et al	Int J Nanomedicine. 2012; 7: 3769-86
CdS	For bioimaging in breast cancer	P.Kumar et al	Adv. Mat. Lett. 2012,3(6),471-475
CdS	Quantum-Dot-Sensitized Solar Cells	S. Abdallah et al	Journal of Nanomaterials Volume 2012 (2012),
CdS	Pathogenic bacteria and their biosensing application	H. N. Abdelhamid et al	J. Mater. Chem. B, 2013,1, 6094-6106
ZnS/CdS	Light Emission in Blue Region	M. Sharma et al	AIP Conference Proceedings, Volume 1276, pp. 88-93 (2010).
CdS/ZnS	Blue Luminescence	S Jonathan et al	Angew.Chem.Int.Ed. 2004, 43, 2154–2158
CdS/ZnS	Highly luminescent blue emitting	X. Liu et al	Volume 130, Issue 3, 1 November 2011, Pages 909–914
CdS/ZnS	Effective and quantitative detection of urea	C.P. Huang et al	Biosens Bioelectron 2007; 22:1835–8.
ZnS	High performance liquid chroma- tography and chemiluminescence	C.H. Collins et al	J Chromatogr A 1999; 846:395–9.
ZnS	Detection of glucose	T. Uematsu et al	Chem Commun 2009:7485–7.
PbS	Application as colloidally stable photovoltaic ink	Carlo Giansante et al	Volume 560, 2 June 2014, Pages 2–9

PbS	Photovoltaic applications and ligand effects on device performance	D. Qilin et al	Appl. Phys. Lett. 102, 203904 (2013)
PbS	Application in Solution-Cast Photovoltaics	C. Giansante et al	J. Phys. Chem. C , 2013, 117 (25),pp 13305–13317
PbS	Solar cell applications	S. Sawanta et al	Dalton Trans., 2012, 41, 6130
PbSe	A Tunable Femtosecond Pump–Hyperspectral Probe Study	I. Gdor et al	J. Phys. Chem. C, 2013, 117 (49)
PbSe	Biological Applications	L. Etgar et al	J. Phys. Chem. C, 2007, 111 (17)
PbSe	high-index, low-melting-temperature glass for infrared laser applications	P. Kannanet al	Proc. SPIE 8621, Optical Components and Materials X, 862104 (20 February 2013); doi: 10.1117/12.2001079
PbSe	1.55 μm telecommunication wavelengths	Lei Zhang at al	Nanotechnology 2014, 105704 (25)
PbSe/PbS	photovoltaic applications	D. Yanover et al	Chem. Mater., 2012, 24 (22)
PbSe/PbS	potential device applications	Jian Xu at al	Nanotechnology (2006) 175428–5434
PbSe/PbS	Optoelectronic Applications	D. Yanover et al	J. Phys. Chem. C, 2014, 118 (30)

(iv) Photonic devices

In 2003, Ozin and co-workers have demonstrated the formation of NC solid arrays derived from the ordered packing of the mono disperse PbS QDs whose emission could be tuned from 1245 to 1625 nm with a FWHM of 65 meV with no trace of trap emission up to 2100 nm [179]. The photoluminescence life time of QDs under excitation of 1.064 μm was found to be mono exponential and longer (1.828 μs) than previously reported (1 μm). The lifetimes in the layered structures were found to be shorter and non exponential due to Forster energy transfer between neighboring QDs. It is also possible to couple PbS QDs dissolved in poly methyl methacrylate (PMMA) to photonic crystal cavities at room temperature [180]. Subsequently, QDs emission is

shown to map out the structure resonance. It is also possible to infiltrate PbS QDs into the photonic colloidal crystals [181]. The technique is based on capillary forces to load PbS QDs in the interstitial voids of the colloid crystals [182]. The shifts in the stop band from resulting infiltration of the colloidal crystal show that PbS QDs occupy nearly 100% of the volume of the interstitial space [183]. In 2003, PbSe NC/sol-gel composites have been used to develop a new optically detected band with a well defined threshold of 0.2mW and a clear super linear growth, which are signatures of amplified spontaneous emission [184]. The optical band of composite containing 4.8 PbSe QDs was observed to be tunable from 1450-1550 nm which is the important "telecommunication window". At the same time, it has been demonstrated that free standing silicon photonic crystal membrane micro cavities can exhibit Q factors as large as 106 [185]. Recently, fabrication and characterization of 1.55 μm Si-based photonic crystal micro cavity light emitters utilizing PbSe QDs is reported [186]. Enhancement of spontaneous emission is observed at 1550 nm at room temperature. Some other reports of application of different QDs in different field have been presented in a table 1.5.

1.1.21 Motivation of research work

Our aim is to prepare the material for number of applications broadly in the fields of Electronics and Biology. Route of preparation should be simple, low cost and ubiquitous at least for II-VI and IV-VI group compounds. Semiconductor quantum dots give the opportunity to play with them and to tune their properties according to the desired field of applications. It can be light emitter in LED, channel in Transistor, flurophore in Solar cell and emission properties of these quantum dots are very useful in biological labeling and *in- vivo* imaging. It is required that in the formation of core/shell and multishell quantum dot structures there should be the same route of preparation for core and shell quantum dots, as well as for II-VI and IV-VI group structures.

1.1.22 Objectives of the thesis

(i) Synthesis and characterization of CdS, ZnS quantum dots and their core/shell CdS/ZnS quantum dots structures.

(ii) Controlled development of inverted ZnS/CdS core/shell quantum dots structures and multishell ZnS/CdS/ZnS quantum dots structures.

(iii) Synthesis and characterization of PbSe, PbS quantum dots and their PbSe/PbS core/shell quantum dots structures.

This chapter concludes about the basic concepts and properties related to different types of quantum dots whether conventional quantum dots, core/shell quantum dots or multishell quantum dots. We have also given up to date literature review on each. However, there are so many reports (table 1.5) on quantum dot synthesis we have proposed a method by which it is possible to obtain II-VI group and IV-VI group quantum dots and their different structures where the use of minimal chemicals, synthesis parameters are easily controllable and results are highly reproducible are assured. These quantum dots have been designed to give highly specific optical properties specifically luminescence, where to enhance the luminescence and tune the luminescence emission are the highlights of the work. In order to analyze the synthesized quantum dots several characterization tools and techniques have been applied and discussed in the next chapter. Subsequently in coming chapters each and every objective will be presented and discussed in thoroughly.

CHAPTER – II

SYNTHESIS AND EXPERIMENTAL TECHNIQUES

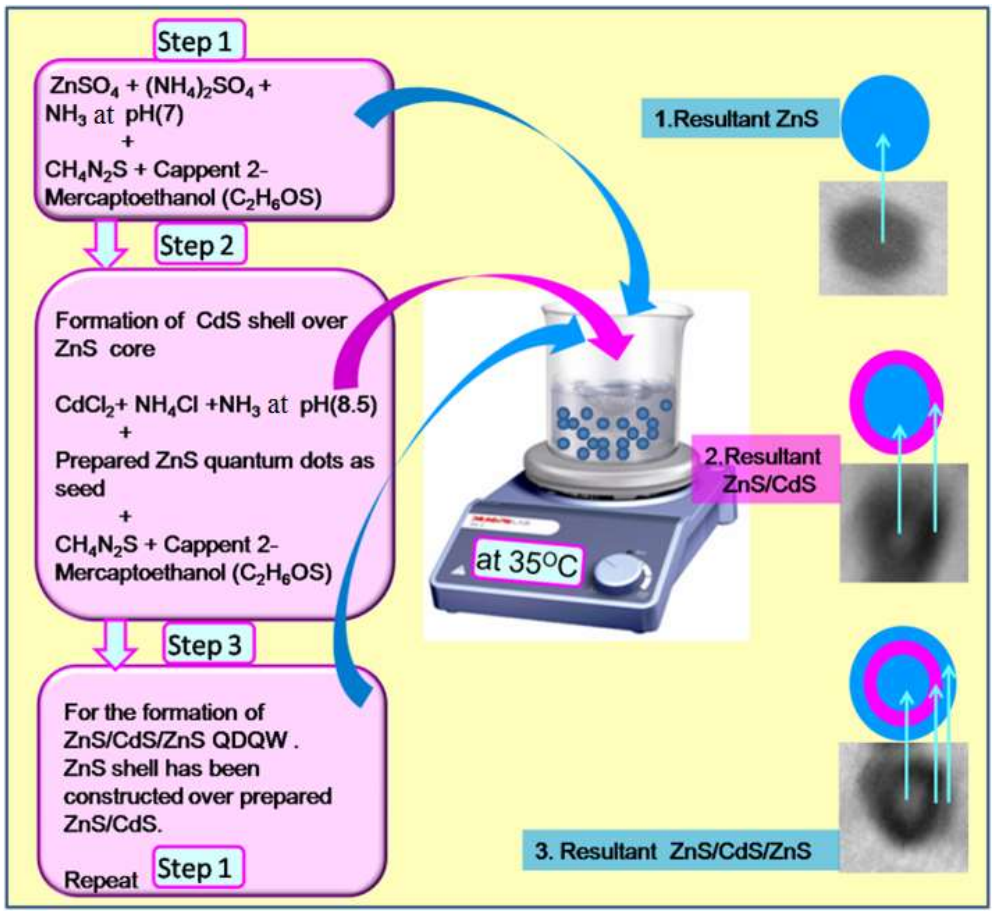

2.1 OVERTURE

This chapter presents the detailed information on the subject of the synthesis and experimental techniques that employed in preparation of all quantum dots (QDs). In this chapter we are explaining whole wet chemical mechanism for the synthesis of CdS, ZnS, CdS/ZnS, ZnS/CdS, ZnS/CdS/ZnS, PbS, PbSe and PbSe/PbS QDs. These all mentioned quantum dots (QDs) [CdS, ZnS, PbS and PbSe], core/shell quantum dots [CdS/ZnS and PbSe/PbS], Inverted core/Shell [ZnS/CdS] and quantum dots quantum well [ZnS/CdS/ZnS] were synthesized by wet chemical method. Structural, morphological, and optical properties of as grown QDs were studied by X-ray diffraction (XRD), Transmission Electron Microscope (TEM), UV-Vis absorption spectroscopy (UV-Vis) and photoluminescence (PL) spectroscopy. The experimental arrangements employed in our work have been described in this chapter.

QDs can be fabricated by many ways which differ in their application for either semiconductor physics or biological imaging: including methods such as e-beam lithography, x-ray lithography, molecular beam epitaxy (MBE), ion implantation, colloidal synthesis, sonochemistry and growth in size restricted environments however, out of this wet chemical route is simple to carry out synthesis of QDs. To form monodispersed (non-agglomerated) particles with a narrow size distribution all the nuclei must form at nearly the same time and subsequent growth must occur without further nucleation of particles [187]. Thus it is very important to stabilize the particles against agglomeration. This can be obtained by using suitable capping agent. Capping by molecules which form chemical bonds with or chemisorbs onto the particles provides an extremely useful method of stabilization. Thiols have been demonstrated to be highly suitable capping agents for semiconducting (CdSe, for example) nanoparticles. There are a number of other techniques to stabilize the surface of nanoparticles which have already been discussed in section 1.5 of chapter 1.

2.1.1 Wet chemical synthesis of II-VI and IV-VI group QDs (e.g. CdS QDs)

The wet chemical synthesis technique (solution growth method) is a very beneficial technique for the synthesis of ZnS and CdS nano particles for the last 8-10 years [188, 189]. The technique is very sensitive in terms of reproducibility of a particular size of particles. This is because various parameters (mentioned below) are involved in the synthesis and have to be reproduced

for obtaining a particular size. Another important task is to minimize the size distribution in order to achieve monodispersed particles. The wet chemical synthesis in general consists of the reaction of Cd and S compounds in the presence of the capping molecule. A solution of cadmium chloride or cadmium acetate is mixed with a solution of the thiourea followed by the addition of capping agent.

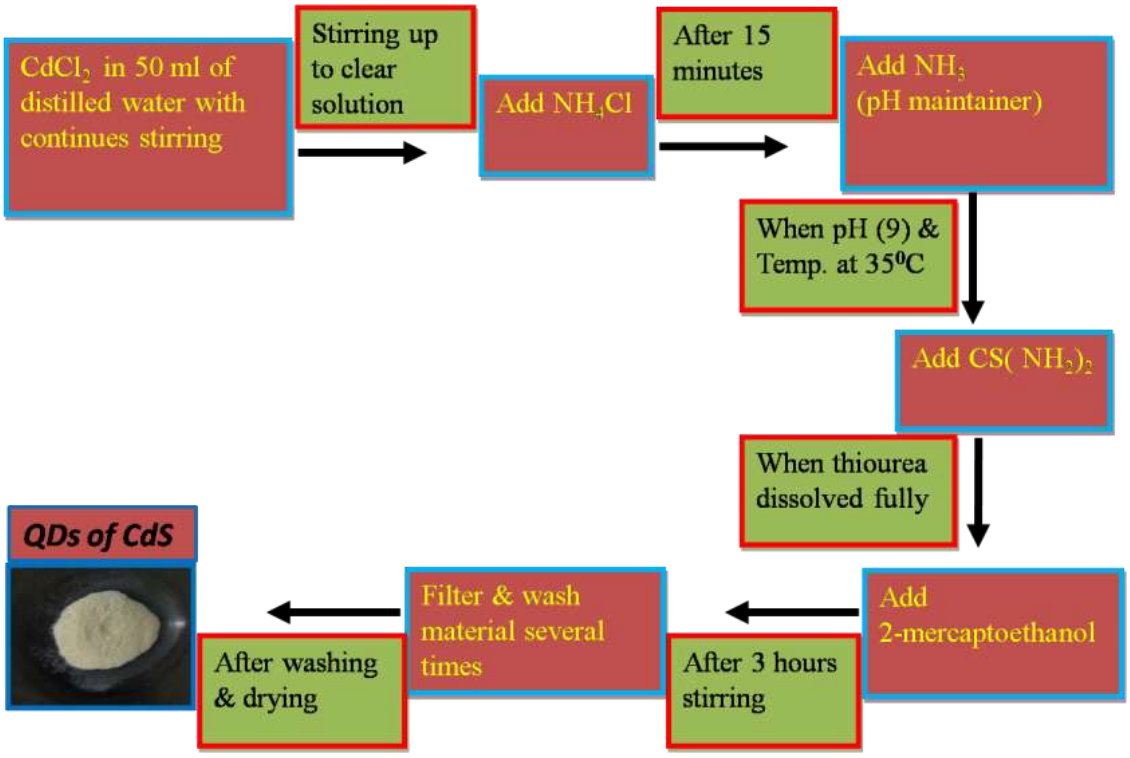

Figure 2.1: A flow chart for wet chemical synthesis of CdS nanoparticles.

The nanoparticles start precipitating immediately, when the addition of sodium sulfide is started. The solution becomes cloudy as the precipitation takes place. The stirring is done till the addition of sodium sulfide is finished and continued further for some specific time in order to facilitate complete precipitation. The nanoparticles are then separated by centrifugation and washed with water or ethanol to get rid of unreacted solvent. For drying, the particles are kept in a Petri dish for about 12 hrs. Then the free standing powder is collected and preserved in an airtight container. The synthesis procedure is illustrated in a flow chart (figure 2.1). A fixed concentration of $CdCl_2$ and thiourea compounds to obtain various sizes. The parameters of the synthesis, which can be fixed and optimized for the synthesis, are mentioned below. However, there are some additional parameters in the synthesis of each size which have to be identified and

tuned in order to get a particular size of interest. These are: volume of the reactants, stirring speed, rate of addition of thiourea, time of stirring after addition of thiourea, temperature and pH-value.

2.2 SYNTHESIS OF CdS QDs

2.2.1 Chemicals required for cadmium sulfide (CdS) synthesis

Cadmium chloride ($CdCl_2$) (Merck 99.9%), ammonium chloride (NH_4Cl) (Merck 99.9%), Aqueous ammonia (25%) (NH_3) (Merck 99.9%) AR-grade was taken as pH controller and thiourea $CS(NH_2)_2$, (Merck 99.9%), 2-mercaptoethanol ($HOCH_2CH_2SH$) (Merck 99.9%) capping agent. Capping agent caps the materials and controls the size of QDs.

2.2.2 Procedure

CdS QDs were synthesized by solution growth method at 35±1ºC and 2-mercaptoethanol has been used as capping agent. This method of preparation regularly uses a complexing agent to control the release of metal ions (Cd^{2+}) to produce the controlled homogeneous reaction in presence of sulphur ions (S^{2-}). Initial solution of CdS was prepared from anhydrous AR grade cadmium chloride ($CdCl_2$), ammonium chloride (NH_4Cl), ammonia (NH_3) and thiourea where as $CS(NH_2)_2$. $CdCl_2$ was used as cadmium and thiourea was used as sulphur source in this reaction. Ammonia was used as complexing agent. The reaction matrix employed in our study consisted of $CdCl_2$, NH_4Cl and thiourea in 1:1.5:3 molar ratios. The reaction matrix was prepared in two parts. In typical synthesis, cadmium chloride and ammonium chloride were mixed in 50 ml of distilled water. Ammonia was added to it until the formation of clear metallic complexes has been achieved, at this time the pH was 8.5. Then thiourea was added into 50 ml of prepared solution. Immediately an appropriate solution of 2-mercaptoethanol was added as a capping agent to control the particle size of CdS QDs and afterwards continuously stirred for 5 hours. Prepared samples of CdS were centrifuged at 3500 RPM for 20 minutes and washed several times with distilled water.

$$CdCl_2 \rightarrow Cd^{2+} + 2Cl^{-}$$

$$NH_4Cl_2 \rightarrow NH_4 + 2Cl^{-}$$

$Cd^{2+} + 2OH^{-} \rightarrow Cd(OH)_2$

$3NH_3 + 2Cl^{-} \rightarrow 2\ NH_4Cl$

$CS(NH_2)_2 + OH^{-} \rightarrow CH_2N_2 + H_2O + HS^{-}$

$HS^{-} + OH^{-} \rightarrow S^{2-} + H_2O$

$Cd^{2+} + S^{2-} \rightarrow CdS$

Throughout overall reaction:-

$CdCl_2 + (NH_2)_2CS + 2NH_4OH \rightarrow CdS + CH_2N_2 + 2NH_4Cl + 2H_2O$

The experimental arrangement employed for synthesis has been shown in figure 2.2.

Figure 2.2: Experimental arrangements employed for wet chemical synthesis of CdS QDs, right side picture shows different size QDs.

2.3 SYNTHESIS OF ZnS QDs

2.3.1 Chemicals required for zinc sulfide (ZnS) synthesis

Zinc sulfate $ZnSO_4$, (Merck 99.9%), ammonium sulfate $(NH_4)_2SO_4$ (Merck 99.9), aqueous ammonia (25%) (NH_3) (Merck 99.9%) AR-grade was taken as pH controller and CS $(NH_2)_2$, (Merck 99.9%). 2-mercaptoethanol ($HOCH_2CH_2SH$) (Merck 99.9%) used as a capping agent.

2.3.2 Procedure

The process for preparing ZnS QDs was similar to CdS QDs using wet chemical method at 35±1°C temperature. The reaction matrix employed in our study consisted of AR grade $ZnSO_4$, $(NH_4)_2SO_4$ and thiourea in 1:1.5:1.5 molar ratios. $ZnSO_4$, and $(NH_4)_2SO_4$ were mixed in 50 ml of distilled water. Ammonia was added to it until the formation of clear metallic complexes has been achieved at this time the pH of the solution was kept at 9.5. Then thiourea was added in 50 ml of prepared solution. After that an appropriate solution of 2-mercaptoethanol was added in solution for passivation then continuously stirred for 5 hours. Prepared samples of ZnS were centrifuged at 3500 RPM for 20 minutes and washed several times with distilled water.

$$ZnSO_4 + 2H_2O \longrightarrow Zn(OH)_2 + H_2SO_4$$

$$Zn(OH)_2 \longrightarrow Zn^{2+} + 2(HO)^-$$

Reduction of sulphide ion from thiourea.

$$(NH_2)_2CS + OH^- \longrightarrow CH_2N_2 + H_2O + HS^-$$

$$HS^- + OH^- \longrightarrow H_2O + S^{2-}$$

$$ZnS^{2+} + S^{2-} \longrightarrow ZnS$$

2.4 SYNTHESIS OF CdS/ZnS CORE/SHELL STRUCTURE

CdS/ZnS core-shell structures were synthesized by seed growth method. As the first step CdS QDs by wet chemical route at 35±1°C temperature have been synthesized. To synthesize CdS/ZnS core/shell QDs, a ZnS shell layer was grown on CdS core QDs using two aqueous solutions of Zn^{2+} and S^{2-} ions which were obtained by dissolving the compounds zinc sulphate dehydrate, and ammonium sulphate by mixing in 50 ml of distilled water. Ammonia was added to it until the formation of clear metallic complexes has been achieved at pH 9.5. After this processes 2.5 ml of prepared CdS solution was added. Then thiourea was added in 50 ml of prepared solution. After that appropriate amount of 2-mercaptoethanol solution was added in solution for passivation then continuously stirred for 5 hours. When the reaction was completed

CdS/ZnS core/shell nanoparticles were centrifuged, washed and dispersed in distilled water before storage.

2.5 SYNTHESIS OF ZnS/CdS AND ZnS/CdS/ZnS QUANTUM DOTS

2.5.1 Procedure (ZnS/CdS)

The reaction matrix employed in our study consisted of AR grade $CdCl_2$, NH_4Cl and thiourea in 1:1.5:3 molar ratios for CdS and AR grade ZnSO4, $(NH_4)_2SO_4$ and thiourea in 1:1.5:1.5 molar ratios for ZnS. ZnS/CdS core/shell structures were synthesized by seed growth method. In order to synthesize desired QDs, we prepared ZnS QDs as seed by solution growth method at 35±1°C with fixed amount of 2-Mercaptoethanol. This method of preparation usually uses a complexing agent to control the release of metal ions (Zn^{2+}) and sulphur ions (S^{2-}) to produce the controlled homogeneous reaction.

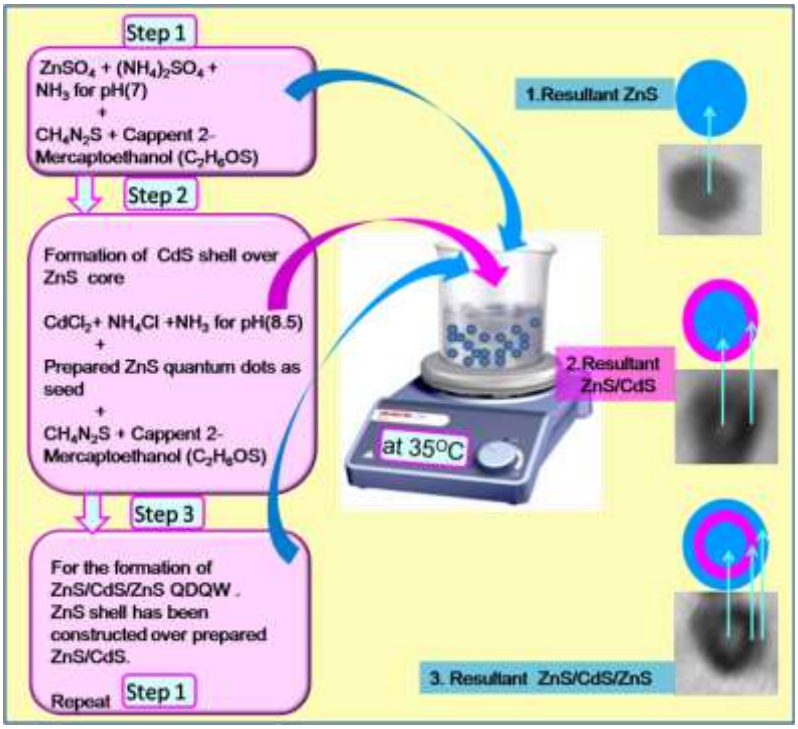

Figure 2.3: Schematic representation of the synthesis procedure to obtain ZnS QDs, ZnS/CdS core/shell QDs and finally ZnS/CdS/ZnS multishell QD structures.

The reaction matrix was prepared in two parts. The initial solutions were prepared from anhydrous zinc sulphate ($ZnSO_4$) and ammonium sulphate ($(NH_4)_2SO_4$) in 50 ml of water.

Ammonia (NH_3) was used as a complexing agent until the formation of clear metallic complexes and so the pH was kept at 8.5. Then thiourea CS $(NH_2)_2$ was added as the source of sulphur in the prepared solution. Immediately 2 ml of (5% solution) 2-mercaptoethenaol was added as a capping agent to control the particle size of QDs and continuously stirred for 5 hours. The process flow for the synthesis of ZnS/CdS/ZnS multishell QDs is presented in figure 2.3.

After synthesis prepared sample of ZnS were centrifuged (3500 RPM, 20 min) and washed several times with distilled water and dried. To synthesize ZnS/CdS core/shell QDs, a CdS shell layer was grown on ZnS core nanocrystals. The method of shell formation of CdS was same as seed ZnS QDs just the source for cadmium that is cadmium chloride ($CdCl_2$) and respective complexing agent ammonium chloride (NH_4Cl) have took place. As the additional step for the synthesis of core/shell structures inclusion of 0.1 g of prepared ZnS QDs was mandatory just before the addition of thiourea. After that required amount of 2-mercaptoethanol was added in solution for capping to obtain ZnS/CdS core/shell structures.

2.5.2 Procedure (ZnS/CdS/ZnS)

For ZnS/CdS/ZnS multishell QDs formation, now ZnS/CdS (0.2 g) has been used as seed and the remaining method is same as opted for ZnS QD synthesis. The size of ZnS/CdS core was kept fixed and varied the shell thickness of ZnS using varying cappent ratio. When the reaction was completed, purification of all core/shell nanocrystals has been performed. Then core/shell QDs were dispersed in distilled water and store.

2.5.3 Mechanism and effect of the 2-mercaptoethanol

2-mercaptoethanol is water soluble, used as capping molecules and also to stabilize the CdS and ZnS/CdS QDs. The SH part acted as the head group while the OH part acted as the tail group. The function of the 2-mercaptoethanol is double: (a) It controls the growth of the particles by forming passivation layers around the CdS shell via coordination bond formation between the S^{2-} atom of the 2-mercaptoethanol and Cd^{2+} ion, or/and (b) it prevents agglomeration by steric effect due to the repulsive force acting among the OH part. Therefore, the 2-mercaptoethanol wrapping creates a restricted environment around the CdS QDs. The Thiols group uses to bind the Cd ions on the surface of core/shell QDs. Figure 2.4 presents the whole mechanisms of binding of 2-

mercaptoethanol with CdS shell. Capping agents may form the binding on the nanocrystals surface, which will slow down the nucleation and growth process. A longer reaction time allows a more mature nanocrystals growth through Ostwald ripening, which may further change the nanocrystals size and concentration. Moreover, capping agent may create a highly packed ligand layer on the nanocrystals surface, hindering monomer diffusion to the nanocrystals surface and their subsequent reactions. The Thiols (–SH) group makes the chelating complex with Cd^{2+}. It is important to mention that the concentration of capping agent in the reaction medium regulates the quantum dots growth by specific adsorption on different crystal faces. Schematic diagram of ZnS/CdS inverted core/shell QDs is shown in figure 2.4.

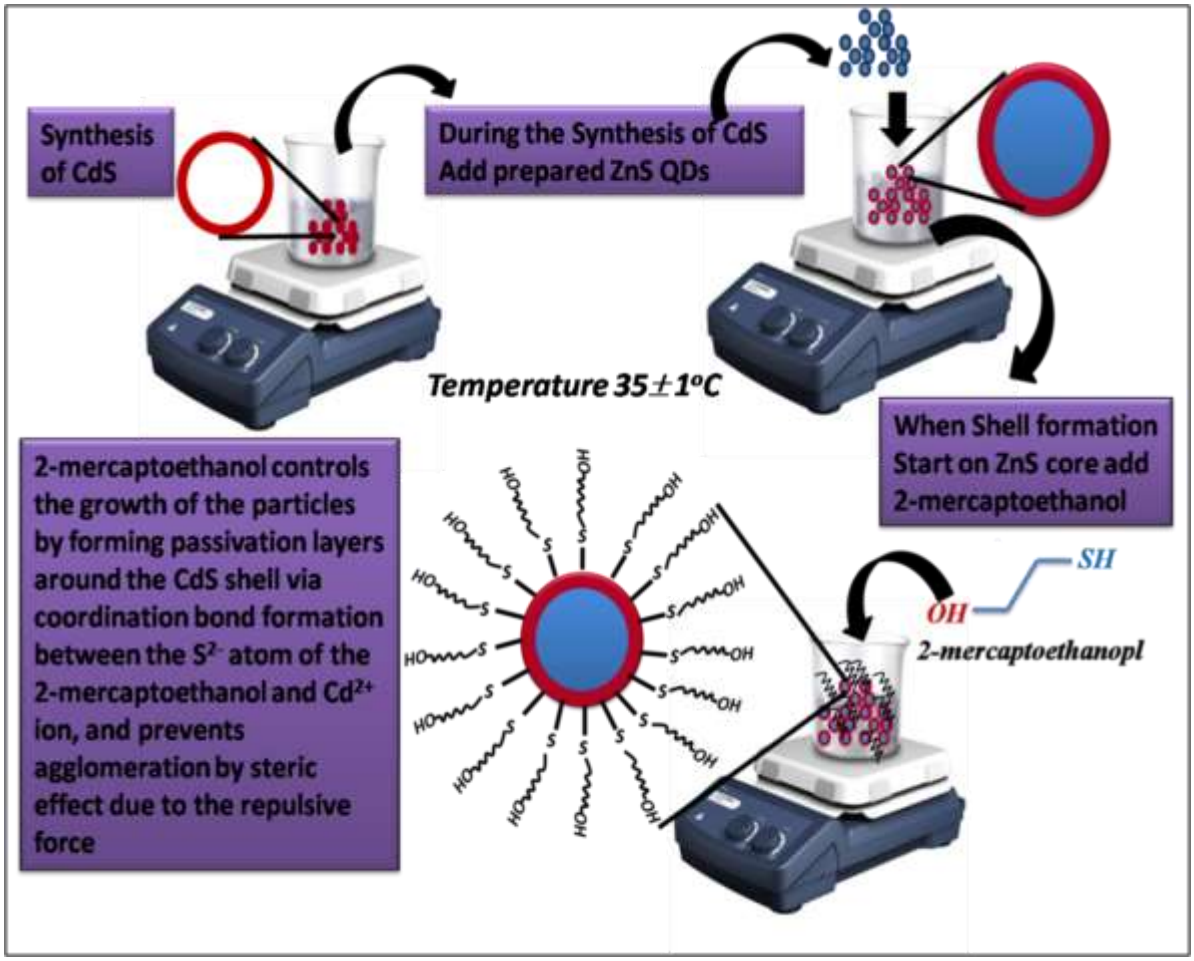

Figure 2.4: Schematic representation of the synthesis procedure to obtain ZnS/CdS inverted core/shell QDs.

2.6 SYNTHESIS OF LEAD SULFIDE (PbS) QDs

2.6.1 Chemicals required for lead sulfide (PbS) synthesis

Lead acetate Pb $(CH_3COO)_2$ (Merck 99.9%), triethanolamine (TEA) $C_6H_{15}NO_3$ (Merck 99.9%), aqueous ammonia (25%) (NH_3) (Merck 99.9%) AR-grade was taken as pH controller and thiourea CS $(NH2)_2$ (Merck 99.9%). 2-mercaptoethanol ($HOCH_2CH_2SH$) (Merck 99.9%) used as a capping agent or to control the size of the QDs.

2.6.2 Procedure

The method of preparation for PbS QDs was wet chemical method at low (35±1°C) temperature. The reaction matrix employed in our study consists of AR grade $Pb(CH_3COO)_2$, triethanolamine (TEA) and thiourea in 1:1.5:1.5 molar ratios. Lead acetate dehydrates, and TEA was mixed in 50 ml of distilled water. The pH was kept at 9.5 using ammonia. Then thiourea was added in 50 ml of prepared solution. After that an appropriate solution of 2-mercaptoethenaol (3 ml) was added in solution for passivation then continuously stirred for 5 hours. After synthesis prepared sample of PbS were centrifuged at 3500 RPM for 45 minutes and washed several times with distilled water.

Lead acetate first generated precursor in TEA solutions:

$Pb(CH_3COO)_2 \cdot 3H_2O + TEA \leftrightarrow [Pb(TEA)]^{2+} + 2(CH_3COO)^-$

$[Pb(TEA)]^{2+} \leftrightarrow Pb^{2+} + TEA$

with the addition of alkaline into thiourea aqueous solutions,

$[(NH_2)_2CS] + OH^- \leftrightarrow CH_2N_2 + H_2O + HS^-$

$HS^- + OH^- \leftrightarrow H_2O + S^{2-}$

mix two kinds of solution, then the formation of PbS can be written as:

$Pb^{2+} + S^{2-} \leftrightarrow PbS\downarrow$

2.7 SYNTHESIS OF LEAD SELENIDE (PbSe)

2.7.1 Chemicals required for lead selenide (PbSe)

Lead acetate Pb $(CH_3COO)_2$ (Merck 99.9%), triethanolamine (TEA) $C_6H_{15}NO_3$ (Merck 99.9%), Aqueous ammonia (25%) (NH_3) (Merck 99.9%) AR-grade was taken as pH controller and sodium selenosulfate (Na_2SeSO3) (Merck 99.9%). 2-mercaptoethanol ($HOCH_2CH_2SH$) (Merck 99.9%) used as a capping agent or to control the size of the QDs.

2.7.2 Procedure

The method of preparation for PbSe QDs was wet chemical method at low (35±1°C) temperature. The reaction matrix employed in our study consists of AR grade Pb $(CH_3COO)_2$, triethanolamine (TEA) and sodium selenosulfate (Na_2SeSO_3) in 1:1.5:1.5 molar ratios. Lead acetate dehydrates, and TEA was mixed in 50 ml of distilled water. The pH was kept at 9.5 using ammonia. Then sodium selenosulfate was added in 50 ml of prepared solution. After that an appropriate solution of 2-mercaptoethanol (3 ml) was added in solution for passivation then continuously stirred for 5 hours. After synthesis prepared samples of PbSe were centrifuged at 3500 RPM for 45 minutes and washed several times with distilled water.

$Pb(CH_3COO)_2 \cdot 3H_2O + TEA \leftrightarrow [Pb(TEA)]^{2+} + 2(CH_3COO)$

$[Pb(TEA)_n] \longrightarrow Pb2^{+} + n(TEA)$

$Na_2SeSO_3 + 2OH^{-} \longrightarrow Na_2SO_4 + Se^{2-} + H_2O$

Formation of PbSe can be written as:

$Pb^{2+} + Se^{2-} \leftrightarrow PbSe$

2.8 SYNTHESIS OF PbSe/PbS CORE/SHELL STRUCTURE

PbSe/PbS core-shell structures were synthesized by seed growth method. As the first step PbSe QDs by wet chemical route at 35±1°C temperature have been synthesized. To synthesize PbSe/PbS core/shell QDs, a PbS shell layer was grown on PbSe core nanocrystals by using two aqueous solutions of Pb^{2+} and Se^{2-} ions which were obtained by dissolving the compounds zinc sulphate dehydrate, and ammonium sulphate by mixing in 50 ml of distilled water. Ammonia was added to it until the formation of clear metallic complexes has been achieved at pH 9.5. After this processes 2.5 ml of prepared PbSe solution was added. Then sodium selenosulfate was added

in 50 ml of prepared solution. After that appropriate amount of 2-mercaptoethanol solution was added in solution for passivation then continuously stirred for 5 hours. When the reaction was completed PbSe/PbS core/shell nanoparticles were centrifuged, washed and dispersed in distilled water before storage.

2.9 CHARACTERIZATION TECHNIQUES

2.9.1 X-ray diffractometer

Figure 2.5 shows the photograph of X-ray diffractometer Shimadzu-6000 used for generating XRD data. This is the most important structural analysis tool in material science field. Figure 2.6 shows the arrangement of slits and geometry in the present set of analysis.

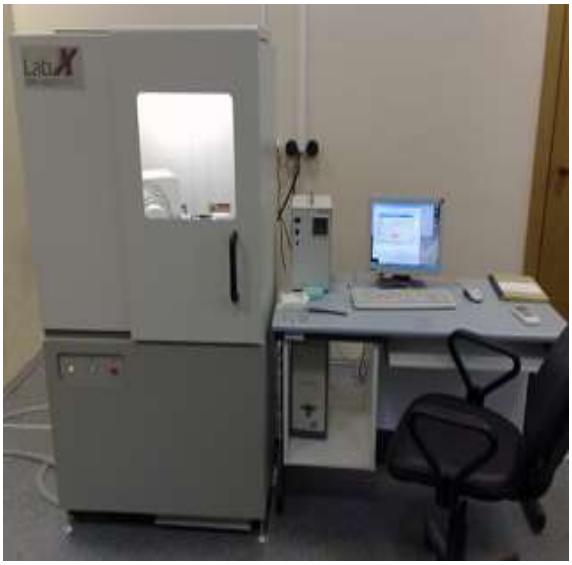

Figure 2.5: Shimadzu (XRD 6000) X-Ray diffractrometer employed for XRD experiments.

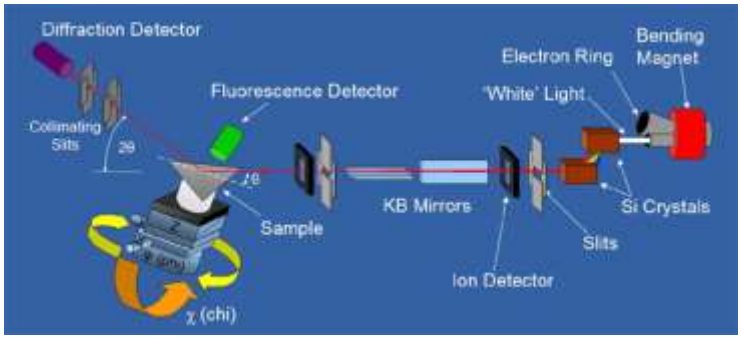

Figure 2.6: The XRD slit arrangement along Rowland circle deployed for experiments.

The XRD Shimadzu-6000 system consists of the equipment main unit and a data processing unit which controls it. The equipment main unit consists of the X-ray generator unit, goniometer unit and CPU which controls them. The generator unit and goniometer unit are controlled by the data processing unit. The block diagram of XRD Shimadzu-6000 has been shown in figure 2.6. In X-ray diffractometer, X-rays emitted from the X-ray tube undergo the limitation of the divergence slit and hit the sample loaded in the center of the Goniometer. The X-rays diffracted from the sample coverage on the receiving slit which is located in the position symmetrical with respect to the X-ray focus of the X-ray tube, viewed from the sample. These X-rays are captured by the scintillation detector, after elimination of noise components, are counted by the pulse height analyzer (PHA). The distance between the atomic planes where X-rays are diffracted can be obtained from the Bragg condition i.e $2d\sin\theta = n\lambda$, where θ=peak angle position of diffracted X-rays and λ is the wavelength of X-rays.

The distance between atoms varies regularly with kinds of atoms or ions. Therefore, if the distance between atomic planes is known, one can know kinds of constituents of the sample. During XRD scanning divergence was always restricted with the help of a 0.15 mm slit on the source side. Drive axis was 2θ for scan range of 20^o-60^o covered in 2^o/minute with step size of 0.02 degree. The instrument propagation error in the d-values was $0.003A^o$. The instrumental peak broadening as determined for Si single crystals from this diffraction was $\Delta 2\theta = 0.2$ degree.

2.9.2 Transmission electron microscopy

Transmission electron microscopy is used to study the microstructure of the samples with a magnification of $3x10^5$ to 10^6 and a resolution of 0.1 nm. Thus far since the wavelength associated with high-energy electrons is in the order of interatomic distances or even smaller, diffraction effects come into play as a result, an image is obtained which give information about the crystal structure and size. The ray diagrams of imaging mode and diffraction mode of operation in an electron microscope are shown in figure 2.7 .A transmission electron microscope is constituted of (1) two or three condenser lenses to focus the electron beam on the sample, (2) an objective lens to form the diffraction in the back focal plane and the image of the sample in the image plane, (3) some intermediate lenses to magnify the image or the diffraction pattern on the screen. If the sample is thin <200 nm and constituted of light chemical elements the image

presents a very low contrast when it is focused. To obtain amplitude contrasted image an objective diaphragm is inserted in the back focal plane to select the transmitted beam, the crystalline parts in Bragg orientation appear dark and the amorphous or the non-Bragg oriented parts appear bright. This imaging mode is called the bright field mode (BF). Figure 2.8 shows the photograph of the transmission electron microscope (TEM) (Hitachi (H-7500)) used for generating TEM images.

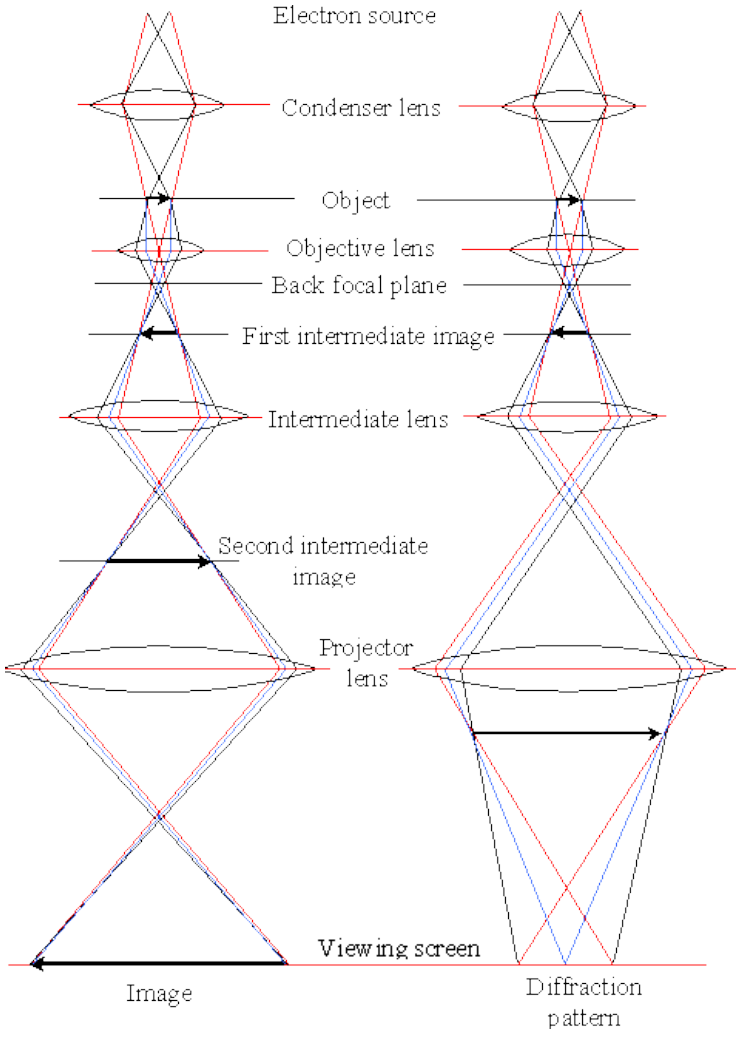

Figure 2.7: The ray diagrams of transmission electron microscope.

If the diffraction is constituted by many diffracting phases, each of them can be differentiated by selecting one of its diffracted beams with the objective diaphragm. To do that, the incident beam must be tilted so that the diffracted beam is put on the objective lens axis to avoid the off-axis

aberrations. This mode is called the dark field mode (DF). The BF and DF modes are used for imaging materials to nanometer scale.

Selected area diffraction (SAED): This mode is used to obtain image of a selected area of the sample or a precipitate. The spherical aberrations of the objective lens limit the area of the selected object to a few hundred nanometers.

Figure 2.8: Photograph of Transmission electron microscope (TEM): Hitachi (H-7500)

2.9.3 Field emission scanning electron microscopy (FESEM)

FESEM is a high-resolution microscope. It is logical method used in material science in order to study the topology, morphology, and composition of the material with much higher resolution. It has many advantages like it produces clear less electrically distorted images with spatial resolution 3-6 times better than that of conventional SEM. Figure 2.9 shows an image of the FE-SEM instrument used in this research.

It can provide beam voltages ranging from 0.2kV to 40 kV and beam currents from 10 picoamps to 10 microamps. This instrument recommends high performance and low noise at low accelerating voltages. Resolution of ca. 3 nm is attainable, and magnifications can be obtained ranging from 10 X to 300,000 X. The cathode is a high-brightness lanthanum hexaboride (LaB6) source. The SEM is equipped with two-inch and four-inch airlocks and a Faraday cup for beam current measurements. The sample stage is computer-driven. Figure 2.10 shows the ray diagram of the FESEM instrument.

Figure 2.9: Photograph of Field emission scanning electron microscopy (FESEM): QUANTA 200 FEG

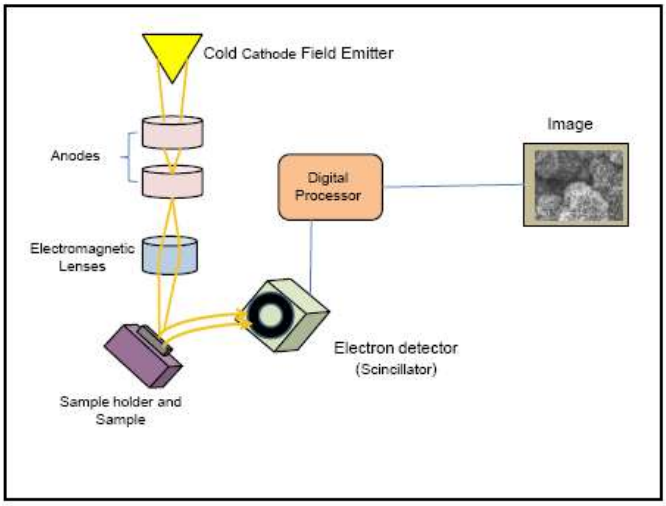

Figure 2.10: Main components of a FESEM instrument QUANTA 200 FEG (Adapted from Flewitt et al. 2003; NMT Materials Dept 2012).

2.9.4 Energy dispersive x-ray spectroscopy (EDX)

It is an analytical technique used for the elemental analysis of a sample. When high energetic electron beam incident on the sample it emits X-rays. By investigating the nature of X-ray generated from the sample we can analyze the elements of the sample and also the amount of content of each element present in the sample. All elements from atomic number 4 (Be) up to 92 (U) contained in the sample can be detected and analyzed simultaneously, but elements of low atomic number are difficult to detect by EDX. An atom within the sample contains ground state electrons in discrete energy levels. The elemental composition of the specimen is measured, because the energy of X-rays is characteristic of energy difference between the two shells and of the atomic structure of the elements present [190], an electron beam strikes the surface of a sample. The energy of the beam is typically in the range of 10-20 KeV. An EDX can be used in various fields like environmental testing, materials identification, home inspection metallography, etc.

2.9.5 Optical characterizations

2.9.5.1 UV-VIS-Spectrophotometer

In the absorption process, photons of a known energy excite an electron from a lower to a higher energy state. Thus by placing a semiconductor specimen at the output of a monochromator and studying the changes in the transmitted radiation, one can discover all the possible transitions an electron can make and learn much about the distribution of states.

Figure 2.11: Photograph of UV-VIS-Spectrophotometer: Perkin-Elmer Lambda 750.

The instrument automatically records a graph of absorbance versus wavelength within a spectral range of 200 to 1100 nm. UV-Vis Spectrophotometer photograph is shown in figure 2.11. Block

diagram of the optical system of the instrument is shown in the figure 2.12. For the absorption study of II-VI group QDs we have used Varian Cary 5000 UV-Vis-NIR Spectrophotometer. A beam of selected wavelength is passed through the sample. Visible, infrared or ultraviolet light from the lamp enters the monochromators, which disperse the light and select the particular wavelength chosen by the operator for the measurement. Light of selected wavelength strikes a rotating mirror, which directs the light beam alternately through the sample and along a reference path. The two light beams coverage on the detector. The relative intensities of the two beams which strike the detector provide a measure of the amount of light absorbed or transmitted by the sample. The absorption spectrum is obtained by an automatic recorder with a scan drive system which changes the wavelength setting of the monochromators and drives the recorder chart.

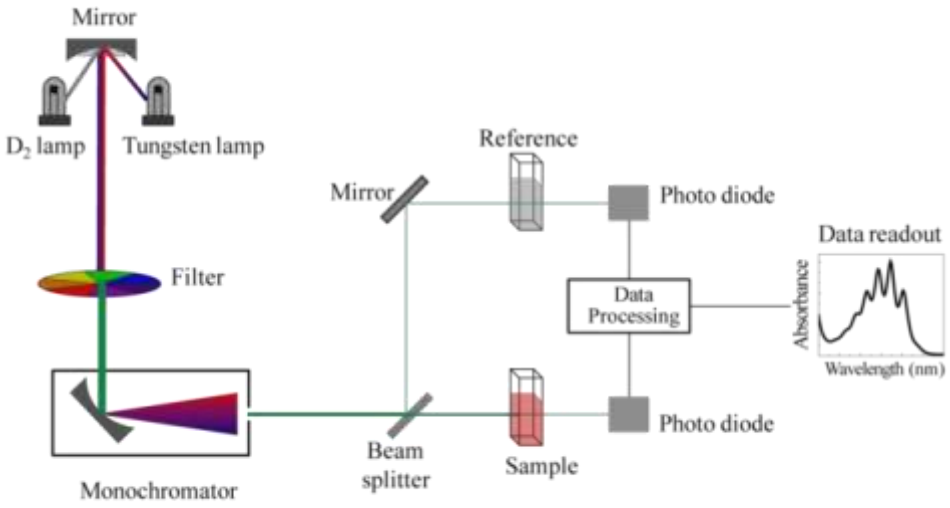

Figure 2.12: Ray diagram of UV-Vis-Spectrophotometer: Perkin-Elmer Lambda 750.

2.9.5.2 Photo Luminescence Spectrophotometer

Photoluminescence spectroscopy is one of the most common methods to reveal energy structure and surface states. This method is suitable for characterization of centers responsible for shallow donor and acceptor species which control the electrical properties of materials. In the simplest form, a suitable source for optical excitation, a spectrometer and a suitable detector for the emitted light are needed to set up the PL experiment. Block diagram of luminescence spectrometer is shown in figure 2.13. The excitation source is a special xenon flash tube, which

produces an intense pulse over the spectral range of the instrument. Energy from source strikes the excitation monochromator. The excitation monochromator consists of an entrance slit, a spherical mirror, grating and an exit slit.

A narrow wavelength band emerges from the exit slit, with the center wavelength being determined by the setting of the grating. The angle of which is controlled by a stepper motor .the majority of the excitation beam is transmitted to the sample while a small proportion is reflected by the beam splitter onto the reference photodiode. To correct the response of the reference photodiode a rhodamine correction curve is stored within the instrument. Rhodamine dye absorbs energy from 230 to 630 nm and fluoresces at about 650 nm with nearly constant quantum efficiency.

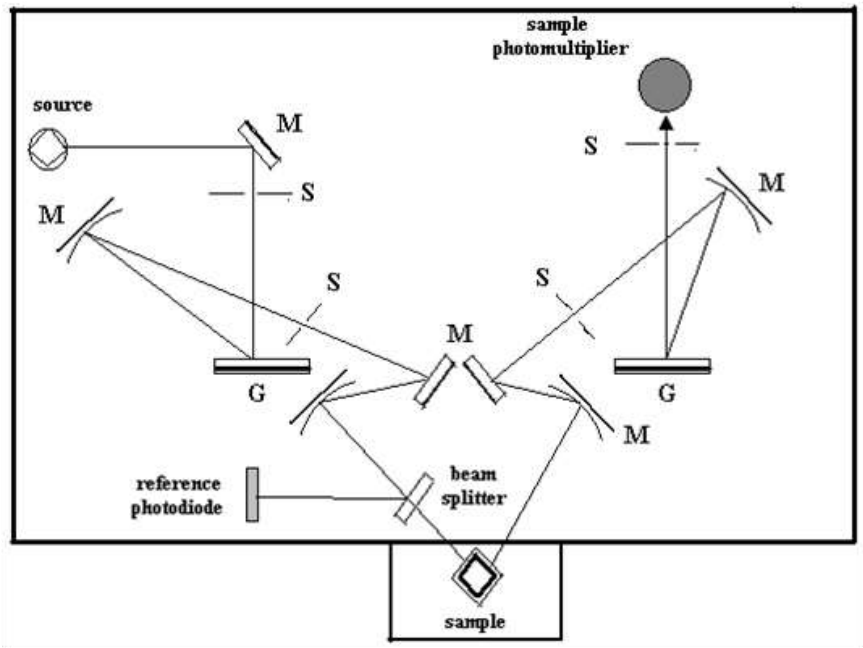

Figure 2.13: Block diagram of Luminescence Spectrophotometer: Perkin-Elmer LS 55.

Energy entitled by the sample during de-excitation is detected by the emission monochromator. Photomultiplier convert these radiations to the electric signals. These data signals undergo integration, conversion averaging and digital filtering before PC receives the data. A graph obtained between the intensity and the wavelength of emitted radiations reports transitions from which impurities can be identified. The photograph of Luminescence spectrometer is shown in figure 2.14.

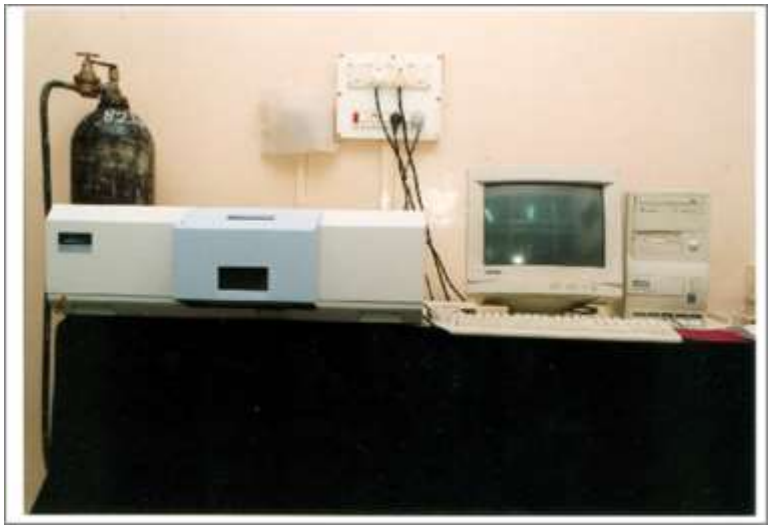

Figure 2.14: Photograph of Photoluminescence spectrometer: Perkin-Elmer LS 55.

2.9.6 Fourier transforms infrared spectroscopy (FT-IR)

Fourier Transform-Infrared Spectroscopy (FTIR) is an excellent technique which is mainly used to identify organic and in some cases inorganic materials. Infrared is a vibrational spectroscopy technique useful for determination of compounds functional groups at the surface of the materials. In terms of wave numbers, the vibrational infrared extends from about 4000 to 450 cm-1. In Infrared absorption process molecules are excited to a higher energy state when they absorb infra red radiation. Photograph of Fourier transforms infrared spectroscopy (FT-IR) is shown in figure 2.15.

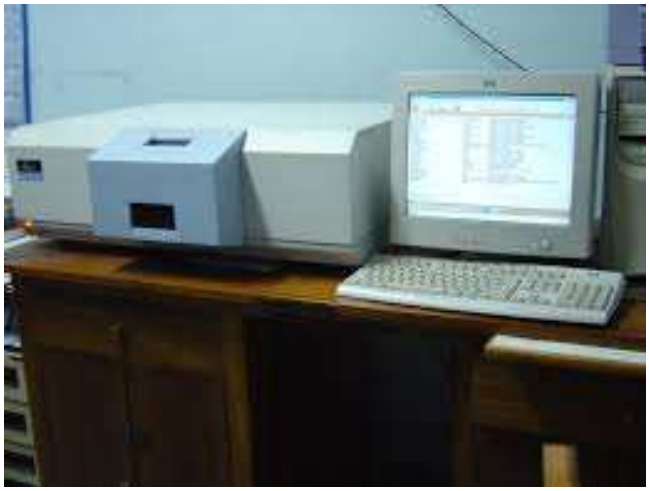

Figure 2.15: Photograph of Fourier transforms infrared spectroscope (FT-IR): RZX (Perkin Elmer)

Radiation in this energy range corresponds to the range encompassing the stretching and bending vibrational frequencies of the bonds in most covalent bonds. FTIR spectroscopy is a preliminary test to detect both organic and inorganic molecule in a compound. Many researchers have studied their compounds using FTIR spectroscopy. Many researchers have also reported IR analysis data viz. Alumina nanoparticles loaded with and without phenanthrene [191], iron oxide reinforced vinyl-ester resin nanocomposite [192], iron oxide nanocrystals [193, 194]. Block diagram of Fourier transforms infrared spectroscopy (FT-IR) is presented in figure 2.16

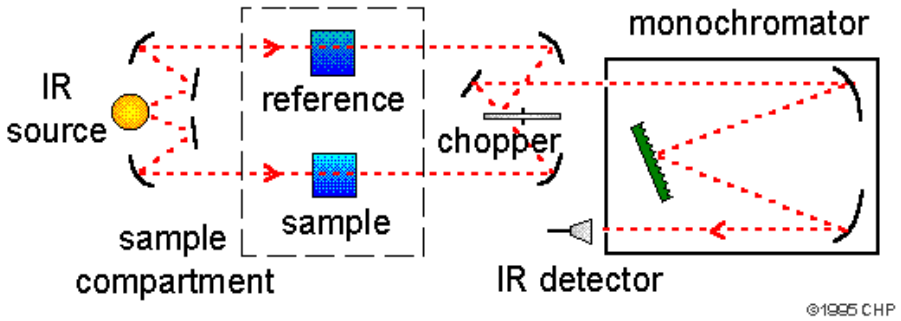

Figure 2.16: Block diagram of Fourier transforms infrared spectroscope (FT-IR): RZX(Perkin Elmer)

2.10 FORMULAE:

1. The crystallite size (D) of the QDs have been calculated using Scherer's formula

$$D=k\lambda / \beta \cos\theta \qquad (2.1)$$

where λ is the wavelength of the x-rays used, β the full width at half maximum of the preferred XRD peak, and θ the Bragg angle.

2. The lattice parameters `a' and 'c' of the unit cell have been calculated according to the relations

For cubic
$$\frac{1}{d^2} = \frac{h^2 + k^2 + l^2}{a^2} \qquad (2.2)$$

For hexagonal
$$\frac{1}{d_{hkl}^2} = \frac{4}{3}\frac{\left(h^2 + hk + k^2\right)}{\left(a^2\right)} + \frac{l^2}{c^2} \qquad (2.3)$$

where d is the interplanar spacing of the atomic planes.

3. The average texture coefficients (TC) of CdS, ZnS, CdS/ZnS QDs were calculated using following equation.

$$TC(hkl)_i = \frac{I(hkl)_i / I_o(hkl)_i}{\frac{1}{N}\sum_n \frac{I(hkl)_n}{I_o(hkl)_n}} \quad (2.4)$$

where *I(hkl)*, I_O*(hkl)* and *N* are the measured relative intensity of a diffraction peak, intensity of the standard powder diffraction peak and the number of diffraction peaks respectively. If *TC (hkl)* = 1, for all the (hkl) planes considered, indicates a sample with randomly oriented crystallite, while values larger than 1, indicate the abundance of crystallite in a given (hkl) direction. Values 1> *TC (hkl)* >0 indicate the lack of grains orientated in that direction.

4. The average strain (ε_{str}) of the CdS and ZnS nanoparticles using Stokes-Wilson equation

$$\varepsilon_{str} = \beta / 4\tan\theta \quad (2.5)$$

The dislocation density (δ) was also calculated from the relation.

$$\delta = 15\varepsilon_{str} / aD \quad (2.6)$$

where ε_{str} = average strain, *a* = lattice parameter and *D* = average grain size.

5. Specific surface area *(SSA)* is the per mass;

$$SSA = SA_{part} / V_{part} x \text{ Density} \quad (2.7)$$

where SA_{part} is surface area, V_{part} is particle volume and density is the value of density of respective QDs. Apart from using the above equation Park et al., 2006 were suggest a more convenient formula for SSA calculation of nanoparticles.

$$S = 6x10^3 D_p^* * \text{Density} \quad (2.8)$$

where *S* is the *SSA*, D_p is the size of the particles, and at last the density of prepared QDs.

6. Absorption coefficient depends on optical band gap, given by

$$\alpha h\nu = K(h\nu - Eg)^n \quad (2.9)$$

where E_g represents the optical band gap, *K* is a constant, and *n* depends on the nature of the transition which has values of 1/2, 3/2, 2, and 3 for allowed direct transitions, forbidden

direct transitions, allowed indirect transitions, and forbidden indirect transitions, respectively .

7. According to Beer–Lambert's relation

$$\alpha = 2.303A/d \tag{2.10}$$

where d is the path length of the quartz cuvette and A is the absorbance determined from absorbance spectra.

8. Optical energy band gap all QDs have been calculated using the formula

$$E_{eV} = hc/\lambda \tag{2.11}$$

where h = Planck's constant and E =energy band gap of the semiconducting QDs. λ is the wavelength.

9. Particle sizes were estimated from the band gap values using Brus equation by effective mass approximation (EMA).

$$E_R = Eg + \frac{\hbar^2}{2m_o R^2}\left[\frac{1}{m_e*} + \frac{1}{m_h*}\right] - \frac{1.8e^2}{4\pi\varepsilon_0\varepsilon_r R} - 0.248\frac{4\pi^2 e^4 m_0}{2(4\pi\varepsilon_0\varepsilon_r)^2 h^2\left(\frac{1}{m_e*} + \frac{1}{m_h*}\right)} \tag{2.12}$$

$$r = \frac{-\left(\frac{1.8e^2}{4\pi\varepsilon\varepsilon_0}\right) + \sqrt{\left(\frac{1.8e^2}{4\pi\varepsilon\varepsilon_0}\right)^2 + \left(E_g^{nano} - E_g^{bulk}\right)\frac{h^2}{2m_0}\left(\frac{1}{m_e^*} + \frac{1}{m_h^*}\right)}}{2\left(E_g^{nano} - E_g^{bulk}\right)} \tag{2.13}$$

where E_g is the bulk band gap. The second term is the kinetic-energy term containing the effective masses, m_e* and m_h*, of the electron and the hole, respectively. The third term arises due to the Coulomb interaction between the electron and the hole, and the fourth term due to the spatial correlation between the electron and the hole which is generally small compared to the other two terms.

10. The TBA scheme has been employed by a number of researchers over the past decade, the parameters for CdS and ZnS used in the calculation mention in table in respective chapter.

$$\Delta E = a_1 e^{-\frac{R}{b_1}} + a_2 e^{-\frac{R}{b_2}} \tag{2.14}$$

11. To overcome the short comings of parabolic band approximations the hyperbolic HBA has been proposed.

$$E_g(R) = \sqrt{E^2{}_g + \frac{2\hbar^2 E_g \pi^2}{m_0 R^2}\frac{1}{2}\left(\frac{1}{m_e^*} + \frac{1}{m_h^*}\right)} \quad (2.15)$$

$$R = \sqrt{\frac{2\pi^2 h^2 E_{gb}}{m^*\left(E_{gn}^2 - E_{gn}^2\right)}} \quad (2.16)$$

where R is quantum dot radius ($2R$ is the diameter and hence the particle size). E_{gb} is the bulk band gap, E_{gn} is quantum dot band gap, h is Planck's constant m^* is effective mass of specimen (1.82×10^{-31} kg for CdS and 3.64×10^{-31} Kg for ZnS).

Note: The above listed formulae will be discussed in detail in next chapters where used with corresponding references with reasons.

CHAPTER – III

SYNTHESIS AND CHARACTERIZATION OF CdS, ZdS QUANTUM DOT AND THEIR CORE/SHELL CdS/ZdS QUANTUM DOT STRUCTURES

This study reports a systematic analysis of size tunable, highly stable and luminescent wurtzite CdS, and quantum dots (QDs). Formation of non agglomerated wurtzite QDs with reduced particle sizes has been confirmed. Size dependent blue shifts have been observed and discussed on the basis of various theoretical models.

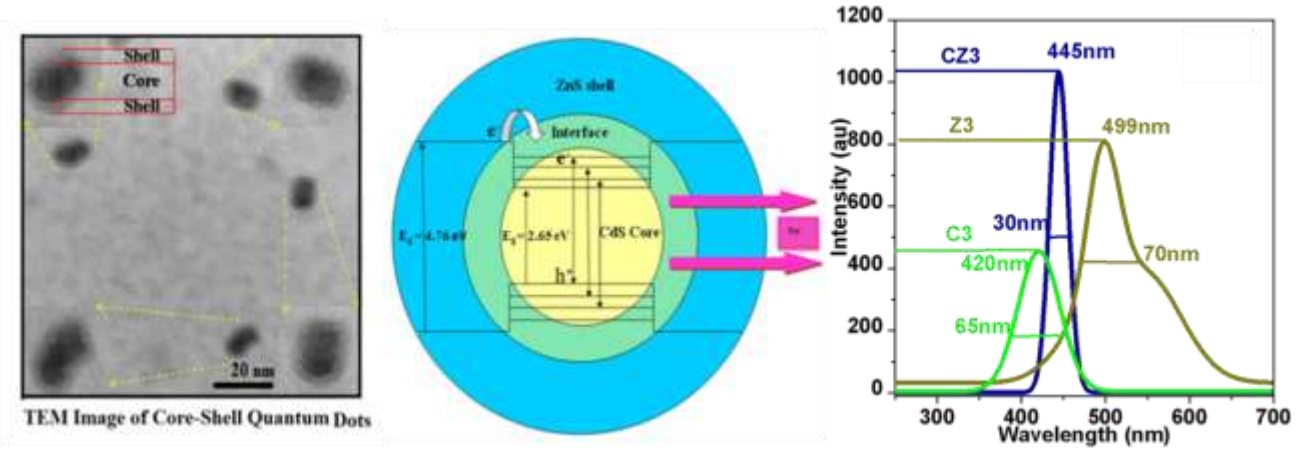

3.1 INTRODUCTION

Quantum dots (QDs) are well known for their tunable optoelectronic properties, which are independent of their chemical properties. For example the emission colors can be adjusted by changing the quantum dot size due to quantum confinement [195]. Among different kinds of QDs; CdS, ZnS and CdS/ZnS have numerous application in the field of low cost tuneable displays [196, 197], low power laser [198], solar energy conversion, light-emitting devices, chemical/biological sensors, bio labelling [59, 199-200] and photo catalysis [201-203] etc. Growing a shell of a wide band gap semiconductor around a nanocrystal core is a proven strategy for increasing both the stability to photo oxidation and increases the photoluminescence quantum yield [199, 20]. The surface modification of a wide band gap semiconducting shell around a narrow band gap core can alter the charge, functionality and reactivity of the materials which consequently enhance the functional properties due to localization of the electron–hole pairs [8, 17, 205]. A number of approaches have been used to synthesize CdS/ZnS quantum dots like micro emulsion [206-208], reverse micelle method [209] and also one pot synthesis and two step synthesis method with different capping agents [210, 211]. However, presently wet chemical growth method has been adopted for the preparation of QDs because of its several advantages like inexpensive raw materials, easy handling and capability of producing high purity samples. Moreover in the present method the agglomeration is less compared to the other methods [212], and they form particles of much smaller sizes with narrow size distribution and possess higher surface area than those reported by other methods.

The highlight and novelty of the present work is to synthesize and analyze their highly luminescent and stable wurtzite CdS, ZnS and CdS/ZnS QDs. In this work all the QDs have been prepared by wet chemical method at low temperature using 2-mercaptoethenol as a stabilizer. CdS/ZnS core/shell structures were formed by capping of CdS core with a thin ZnS shell. ZnS has a wider band gap than CdS, which allows the growth of a thin ZnS layer outside the CdS core. Low temperature wurtzite QDs possess excellent structural and optical properties due to known high stability of wurtzite structure. CdS/ZnS QDs are non toxic biocompatible due to the use of ZnS as a shell. Moreover QDs were capped by 2-mercaptoethenaol, which uses the thiols group to bind the Zn ions on the surface of core-shell QDs [213]. This chapter (3^{rd} chapter) fully describe systematic analysis of size tunable, highly stable and luminescent wurtzite CdS, ZnS and CdS/ZnS quantum dots (QDs) synthesized by wet chemical growth method. Formation of non agglomerated wurtzite QDs

with reduced particle size have been confirmed from x-ray diffraction and transmission electron microscopy studies. Size dependent blue shifts have been observed and discussed on the basis of various theoretical models. Significantly, enhanced luminescence and monochromaticity have been observed in QDs due to particle size reduction and on core/shell structure formation. Fourier transform infrared spectroscopy indicates that OH, CH_2 and C-O functional groups are present on the QDs surfaces and for this reason these QDs can be used in various biological applications.

We have attempted to use 2-mercaptoethenol as a capping agent giveing the opportunity to modify the surface of materials and due to this O-H, N-H, COOH and C-O groups are present on the surface of prepared QDs as confirmed by FTIR. These functional groups can be easily attached to bio molecules because of the similar functionalities available on most of the bio molecules. We have employed X-ray diffraction (XRD), UV–Vis spectroscopy, photoluminescence spectroscopy (PL), Fourier transform infrared spectroscopy (FTIR) and Transmission electron microscopy (TEM) techniques to characterize ZnS, CdS and CdS/ZnS core/shell QDs and results are being presented in this paper.

3.2 EXPERIMENTAL

Synthesis and characterization of 2-mercaptoethanol capped wurtzite CdS, ZnS and CdS/ZnS quantum dots

CdS QDs were synthesized by solution growth method at 35±1^{o}C and 2-Mercaptoethenaol has been used as capping agent. Same procedure of synthesis has also been followed for the synthesis of ZnS and CdS/ZnS core/shell QDs which is fully explained with all chemical reaction mechanisms in second chapter section (2.3 Synthesis of CdS QDs & 2.5 Synthesis of ZnS QDs). The prepared QDs were characterized by different characterization techniques. The structural investigation has been performed by XRD and the patterns were recorded in a Shimadzu powder x-ray diffractometer using Cu Kα1 radiation. The optical properties were studied by PerkinElmer Lambda2 UV–Vis spectrophotometer and absorbance spectra were recorded. Photoluminescence (PL) emission spectra and Photoluminescence (PL) Excitation spectra of the samples were recorded by a computer controlled luminescence spectrophotometer LS55 (Perkin-Elmer Instruments, UK) with accuracy= ±1.0 nm and λ reproducibility= ±0.5 nm. A 20 kW pulse <10 μs from a Xenon discharge lamp was used as the excitation source for recording photoluminescence emission spectra. A gated photo

multiplier tube was used as a detector. Prior to the PL experiments signal-to noise ratio was adjusted to 500:1, using the Raman band of water with excitation at 220 nm. The surface chemistry of the QDs has been studied using FTIR (Perkin-Elmer RX). Transmission electron microscopy (Hitachi H-7500) has been performed as the finest proof for the particle size and particle size distribution.

3.3 RESULTS AND DISCUSSIONS

The group II-VI compounds formed by the elements of group II and VI of the periodic table possess both zinc blende (cubic) as well as hexagonal (wurtzite) structure. Zinc sulphide may adopt two crystalline structures at room temperature namely wurtzite & zinc blende. The cubic form has a band gap of 3.6 eV at 300K where as the hexagonal form has a band gap of 3.91 eV [Lide and Frederikse (1996), Mandal et al (1999)].The structure shown in figure 3.1 has two cubic close packed arrays; one of sulphur atoms and the other of zinc atoms translated with respect to one another by ¼ the body diagonal of the usual cubic cell along a threefold axis. Each atom has 4 first neighbors of the other kind at the corners of a regular tetrahedron and 12 second neighbors of the same kind. Six of the second neighbors are in the same plane as the original atom at the corners of a regular hexagon; the remaining six are distributed three above and three below at the corners of a trigonal antiprism. Figure 3.2 illustrates the hexagonal picture of the arrangement of ZnS atoms in which the intermediate ring of alternate sulphur and zinc atoms contains the central sulphur atom.

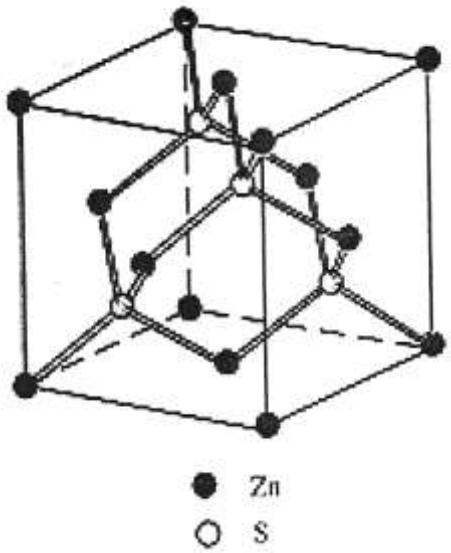

Figure 3.1: The zinc-blende crystal structure of ZnS showing cubic symmetry. The solid and hollow spheres represent zinc & sulphur atoms respectively.

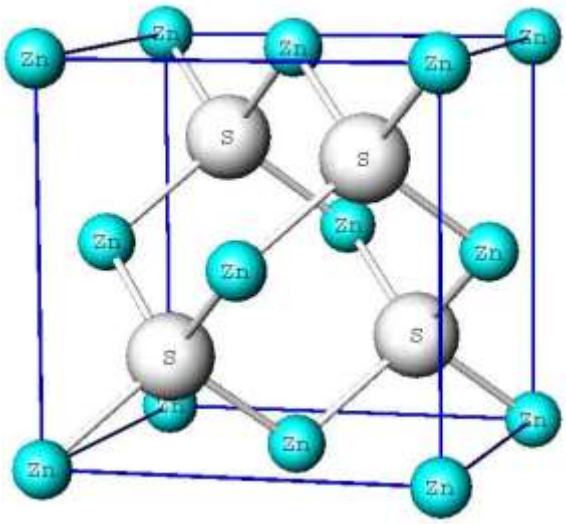

Figure 3.2: ZnS hexagonal lattice. The small and big balls respectively denote Zn & S atoms.

The CdS compound also exists in both zinc blende (fcc) and wurtzite (hexagonal) structures. Size dependent structural transition has also been reported in CdSe. The large size nanocrystals of CdS possess hexagonal structure whereas small nanocrystals seem to be in cubic phase (Hernandez et al [2005], Trojnek et al [2000]). The cubic structure was observed by Gorer et al (1994) with both small (diameter of 5 nm) and large (diameter of 18 nm) nanocrystals. The hexagonal phase in larger nanocrystals obtained by heat treatment was observed also by Bawendi [1989] and Brajesh [1997].

A unit cell of CdS zinc blende crystal is shown in figure 3.3. The solid spheres in the diagram denote S atom and hollow spheres denote Cd atoms. Cubic CdS structure results when Cd atoms are placed on one fcc lattice and S.

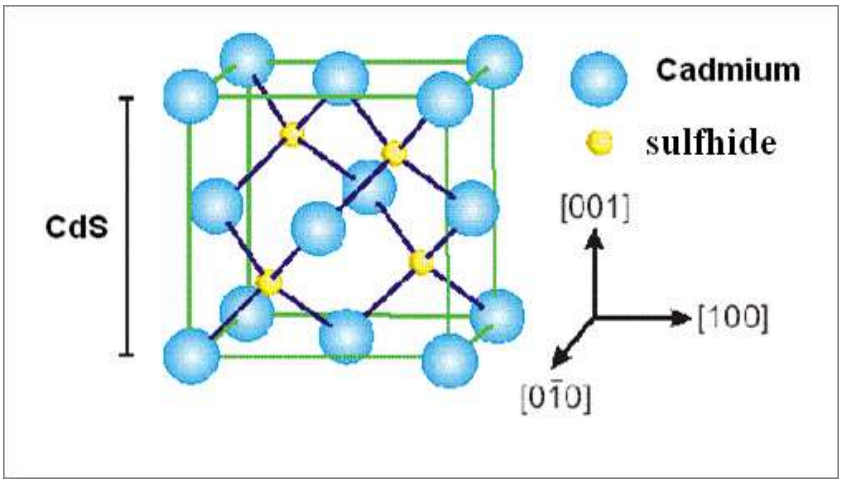

Figure 3.3: Unit cell of CdS zinc blende crystal.

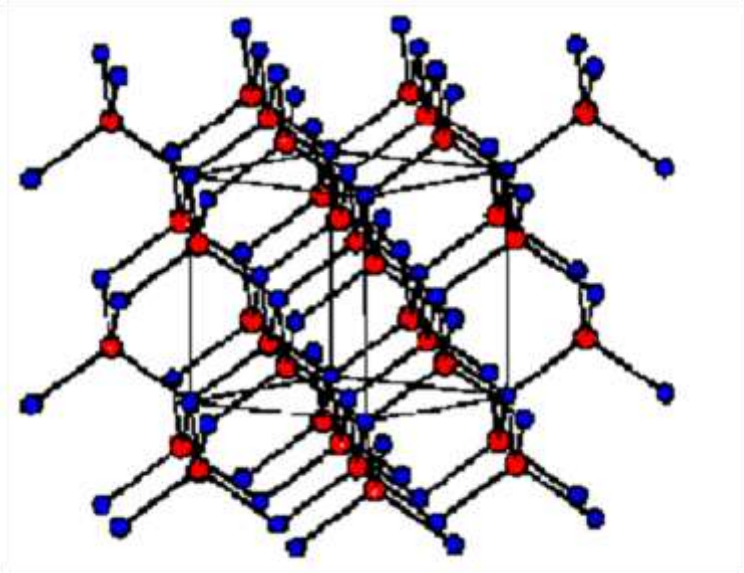

Figure 3.4: Crystal structure of CdS wurtzite structure (hexagonal).

The atoms on the other fcc lattice as shown in figure 3.4 (a). The conventional unit cell is a cube. This structure is almost identical to the diamond structure except that the two interpenetrating fcc sublattices are of different atoms and are displaced from each other by ¼ of the body diagonal. Hence the general position of the atom is a/4, a/4, a/4 parallel to the central axial mirror plane i.e. glide plane. Wurtzite structure of CdS crystal has been shown in figure (3.4).

3.3.1 Structural analysis

X-ray diffraction spectra of 2-mercaptoethanol capped CdS (C1, C2, C3), ZnS (Z1, Z2, Z3) and core/shell CdS/ZnS (CZ1, CZ2, CZ3) QDs have been shown in figure 3.5 (a, b and c). All the QDS were synthesized and capped by varying concentration of 2-mercaptoethanol (1 ml, 2 ml and 4 ml) for samples 1, 2 and 3 in each set respectively. It has been reported that CdS exists in two crystalline forms, viz face centered cubic (fcc) and hexagonal closed packed (wurtzite) phases. Both these structures are closely related and share several common inter-planar (d) spacing with periodic stacks of cadmium atoms that are tetrahedrally co-ordinated to sulphur atoms. The free energies of formation of both these structural modifications differ marginally and hence coexistence of a mixed phase of CdS has often been observed during CdS synthesis [214]. The prominent peaks (101), (110), (112) were shows in figure 3.5 indexed to the wurtzite structure and (311) as indexed to the cubic structure. The successive broadening in XRD peaks show that the particle size substantially

reduces with increasing concentration of the stabilizer. It means cappent appropriately cap CdS QDs which arrest the size. The crystallite size (*D*) of the QDs have been calculated using Scherer's formula

$$D = k\lambda / \beta \cos\theta \qquad (3.1)$$

where λ is the wavelength of the x-rays used, β the full width at half maximum of the preferred XRD peak, and θ the Bragg angle. XRD broadening could be due to other contributions like strain effects which, will be discussed later. The average crystallite size obtained for CdS QDs is 2.9 nm, which was obtained from the width of the (111) peak.

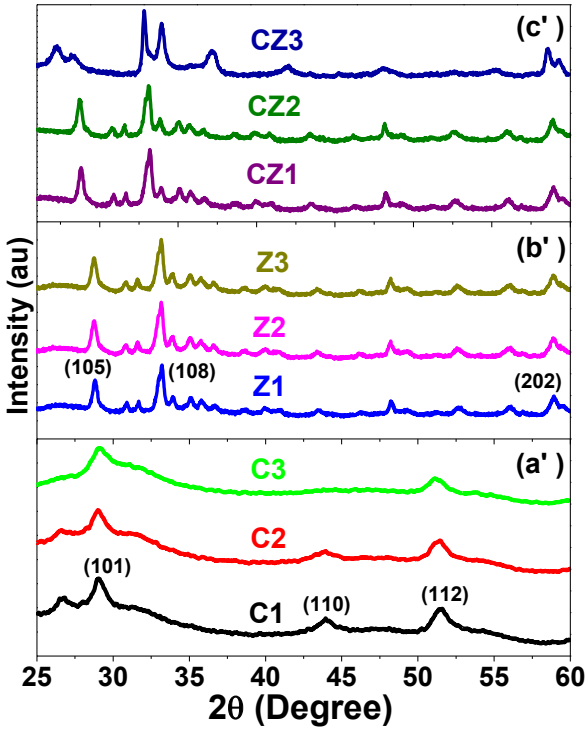

Figure 3.5: XRD pattern of 2-mercaptoethenol capped (a) CdS (C1, C2, C3), (b) ZnS (Z1, Z2, Z3) and (c) CdS/ZnS (CZ1, CZ2, CZ2) QDs.

The most prominent peaks in ZnS QDs (figure 3.5 (b)) were (105), (108), (202) and (222) indexed to the wurtzite structure. In ZnS samples the successive broadening of XRD peaks attributes the reduction in particle size. The average crystallite size of ZnS QDs was 5nm, obtained from the width of the (200) peak with crystallite size of 4.8 nm. No additional peaks due to any impurity phase could be detected in the samples as vindicated from XRD spectra. Figure 3.5 (c) shows the XRD spectra of CdS/ZnS nanoparticles (CZ1, CZ2, CZ3). The diffraction peaks were broadened prominently, which is the characteristic of

nanoparticles. XRD of core/shell structures clearly show that the prominent peak located at the centre of both CdS and ZnS spectra approximately. This is a clear indication of the formation of the corresponding core/shell structures .This shift in XRD pattern have been observed in many studies [118]. The full width at half maxima (FWHM), intensity, phase assignment and crystallite size as calculated have been tabulated in table 1. The lattice parameters `a' of the unit cell has been calculated according to the relations

For cubic
$$\frac{1}{d^2} = \frac{h^2 + k^2 + l^2}{a^2} \qquad (3.2)$$

For hexagonal
$$\frac{1}{d_{hkl}^2} = \frac{4}{3}\frac{\left(h^2 + hk + k^2\right)}{\left(a^2\right)} + \frac{l^2}{c^2} \qquad (3.3)$$

where *d* is the interplanar spacing of the atomic planes as determined from the position of the peak (111), lattice parameter values have also been presented in the table 3.1.

To quantitatively investigate the degree of preferred orientations, the average texture coefficients (TC) of CdS, ZnS, and CdS/ZnS QDs were calculated using following equation.

$$TC(hkl)_i = \frac{I(hkl)_i / I_o(hkl)_i}{\frac{1}{N}\sum_n \frac{I(hkl)_n}{I_o(hkl)_n}} \qquad (3.4)$$

where *I(hkl)*, $I_O(hkl)$ and *N* are the measured relative intensity of a diffraction peak, intensity of the standard powder diffraction peak and the number of diffraction peaks respectively. If *TC (hkl)* = 1, indicates a sample with randomly oriented crystallite. For the values larger than 1; indicate the abundance of crystallite in a given (hkl) direction. Values 1> *TC (hkl)* >0 indicate the lack of grains orientated in that direction. It can be observed that the highest *TC(hkl)* value is in (111), (200), (222) plane for all CdS, ZnS, CdS/ZnS QDs. TC values larger than 1 indicate a preferred orientation of the crystals/grains in the samples and the values found to be 1.63, 1.44 and 1.21 in CdS, ZnS, CdS/ZnS QDs respectively. The calculated values have been presented in table 3.2.

Crystals have generally two types of strains, uniform and non uniform. We concluded that in our samples, there is non-uniform strain that leads to systematic shifts of atoms from their ideal positions leading to peak broadening. This type of strain arises from any of the following sources viz, point defects, vacancies, site-disorder and poor crystallanity.

Table 3.1: FWHM, intensity, phase assignment, lattice constant and particle size of 2- Mercaptoethanol capped CdS, ZnS and CdS/ZnS QDs at room temperature.

Samples	2θ degree	d (Å)		FWHM (degree)	Intensity	hkl	Phase assignment	Particle size (D) (nm)	Lattice constant (Å)	Lattice Mismatch (%)
		Obs.	Stand.							
C1	26.85	3.34	3.36	1.56	60	(002)	Hexa		a = 3.9 C= 6.6	0.04 0.01
	28.99	3.06	3.16	5.86	100	(101)	Hexa	3.28	a = 4.0 C= 6.7	0.02 0.00
	32.77	2.88	2.90	2.61	40	(200)	Cubic		a = 3.8	0.07
	44.04	1.97	2.05	5.60	10	(110)	Hexa		a = 3.8 C= 6.6	0.07 0.01
	47.54	1.86	1.89	2.02	50	(103)	Hexa		a = 4.1 C= 6.7	0.00 0.00
	51.50	1.77	1.75	1.69	55	(112)	Hexa		a = 4.0 C= 6.5	0.02 0.01
C2	26.85	3.34	3.36	2.20	60	(002)	Hexa		a = 3.7 C= 6.4	0.09 0.04
	29.13	3.06	3.16	1.25	100	(101)	Hexa	3.08	a = 4.2 C= 6.7	0.02 0.00
	31.55	2.88	2.90	7.01	40	(200)	Cubic		a = 3.8	0.07
	44.05	1.97	2.05	5.62	10	(103)	Hexa		a = 3.9 C= 6.6	0.04 0.01
	51.15	1.77	1.75	3.55	55	(112)	Hexa		a = 4.1 C= 6.7	0.00 0.00
C3	26.85	3.34	3.36	3.14	60	(002)	Hexa		a = 3.9 C= 6.6	0.04 0.01
	29.13	3.06	3.16	2.52	100	(101)	Hexa	2.45	a = 4.0 C= 6.7	0.02 0.00
	31.55	2.88	2.90	5.10	40	(200)	Cubic		a = 3.8	0.07
	44.05	1.97	2.05	6.57	10	(103)	Hexa		a = 3.8 C= 6.6	0.07 0.01
	51.15	1.77	1.75	2.47	55	(112)	Hexa		a = 4.1 C= 6.7	0.00 0.00
Z1	24.31	3.71	3.70	1.41	3	(100)	Hexa		a = 5.4 C= 30.2	0.00 0.03
	28.90	3.10	3.12	1.34	80	(00,10)	Hexa		a = 5.4 C= 31.4	0.00 0.06
	30.08	2.70	2,70	2.84	100	(105)	Hexa	5.5	a = 5.4 C= 31.3	0.00 0.05
	34.79	2.55	2.52	2.55	25	(108)	Hexa		a = 3.7 C= 30.7	0.03 0.01
	48.22	1.87	1.91	1.21	12	(110)	Hexa		a = 5.4 C= 30.2	0.00 0.03
	52.74	1.76	1.75	1.24	16	(10,15)	Hexa		a = 3.6 C= 30.8	0.04 0.04
	56.04	1.85	1.89	1.35	45	(10,10)	Hexa		a = 6.1 C= 31.5	0.12 0.09
	58.98	1.56	1.56	1.34	42	(206)	Hexa		a = 5.4 C= 31.2	0.00 0.00
Z2	24.31	3.71	3.70	1.53	3	(100)	Hexa		a = 5.4 C= 30.6	0.00 0.01
	28.90	3.10	3.12	1.38	80	(00,10)	Hexa		a = 5.4 C= 31.2	0.00 0.00
	30.08	2.70	2,70	2.86	100	(105)	Hexa	5.0	a = 5.4 C= 31.4	0.00 0.06
	34.79	2.55	2.52	2.76	25	(108)	Hexa		a = 3.5 C= 30.7	0.08 0.01
	48.22	1.87	1.91	1.29	12	(110)	Hexa		a = 5.4 C= 31.3	0.00 0.05
	52.74	1.76	1.75	1.44	16	(10,15)	Hexa		a = 3.6 C= 30.7	0.04 0.01
	58.98	1.56	1.56	1.55	42	(10,10)	Hexa		a = 5.4 C= 31.1	0.00 0.03
						(206)	Hexa			
Z3	27.23	3.22	3.10	3.52	11	(102)	Hexa		a = 5.4 C= 31.3	0.00 0.05
	32.84	2.70	2.70	1.11	100	(107)	Hexa	4.8	a = 5.4 C= 30.8	0.00 0.02
	33.95	2.64	2.52	1.01	25	(108)	Hexa		a = 3.5 C= 30.5	0.05 0.90
	36.76	2.32	2.30	2.73	100	(101)	Hexa		a = 3.6 C= 30.4	0.04 0.02
	41.88	2.20	2.25	1.78	70	(10,12)	Hexa		a = 3.7 C= 30.7	0.00 0.01
	48.11	1.88	1.91	1.06	12	(10,10)	Hexa		a = 5.4 C= 31.1	0.01 0.03
	55.18	1.66	1.89	1.71	45	(202)	Hexa		a = 6.1 C= 31.2	0.12 0.00
	58.85	1.56	1.56	1.21	42	(202)	Hexa		a = 5.4 C=30.3	0.00 0.02
CZ1	23.24	3.71	3.70	1.53	3	(100)	Hexa		a = 4.0 c = 31.5	0.02 0.02
	28.64	3.10	3.12	1.38	80	(111)	Hexa		a = 5.4 c = 31.4	0.00 0.06
	31.36	2.70	2.70	2.86	100	(106)	Hexa	5.8	a = 3.6 c = 30.7	0.01 0.07
	33.23	2.61	2.64	1.08	31	(200)	Hexa		a = 5.2 c = 30.8	0.02 0.04
	35.25	2.55	2.52	2.76	25	(107)	Hexa		a = 3.7 c = 30.7	0.03 0.01
	40.20	1.87	1.91	1.29	12	(10 12)	Hexa		a = 5.4 c = 30.9	0.00 0.04
	56.18	1.76	1.75	1.44	16	(311)	Hexa		a = 3.6 c = 31.2	0.01 0.01
	48.30	1.88	1.91	1.21	30	(220)	Hexa		a = 5.3 c = 31.3	0.00 0.05
	59.18	1.56	1.56	1.55	42	(222)	Hexa		a = 5.4 c = 31.2	0.00 0.00
CZ2	28.64	3.10	3.12	1.38	31	(111)	Hexa		a = 5.4 c = 30.7	0.00 0.01
	33.17	2.61	2.64	1.08	100	(200)	Hexa		a = 5.4 c = 30.5	0.00 0.90
	35.25	2.55	2.52	2.76	25	(107)	Hexa	5.5	a = 5.4 c = 31.2	0.00 0.00
	40.20	1.87	2.01	1.29	12	(10 12)	Hexa		a = 5.2 c = 31.3	0.02 0.05
	56.18	1.76	1.78	1.44	16	(311)	Hexa		a = 3.7 c = 30.7	0.03 0.01
	48.30	1.56	1.62	1.55	42	(220)	Hexa		a = 5.4 c = 30.1	0.00 0.07
	59.18	1.57	1.60	1.54	42	(222)	Hexa		a = 3.6 c = 30.7	0.04 0.01
CZ3	26.70	3.71	3.70	2.24	3	(100)	Hexa		a = 5.4 c = 31.2	0.00 0.00
	32.82	2.61	2.64	1.00	100	(200)	Hexa		a = 5.4 c = 30.1	0.00 0.07
	34.00	2.55	2.52	1.54	80	(107)	Hexa	5.1	a = 3.6 c = 30.1	0.00 0.04
	35.55	1.87	1.91	1.00	31	(108)	Hexa		a = 3.6 c = 30.1	0.00 0.04
	36.90	1.76	1.75	2.03	25	(102)	Hexa		a = 3.7 c = 30.2	0.03 0.08
	58.70	1.56	1.56	1.21	12	(222)	Hexa		a = 5.4 c = 30.5	0.00 0.90

Table 3.2: Miller planes, standard intensity, observed normalized intensity and texture coefficient of 2-mercaptoethanol capped CdS, ZnS and CdS/ZnS QDs at room temperature.

Sample	Miller Planes	Standard Intensity I_N	Observed normalized Intensity and texture Coefficient	
			I_o	TC (hkl)
CdS	111/220/311	100/60/20	100/10/60	1.63
ZnS	111/200/222	100/10/2	80/87/42	1.44
CdS/ZnS	111/200/222	100/10/2	10/100/42	1.21

As already mentioned the XRD peak broadening could also be due to the strain in addition to the crystallite size of the particles. Stokes and Wilson (1944) first observed that strained or imperfect crystals containing line broadening of a different sort, than the broadening that arises from small crystallite size. Hence an attempt has been made to estimate the average strain (ε_{str}) of the CdS and ZnS nanoparticles using Stokes-Wilson equation.

$$\varepsilon_{str} = \beta / 4\tan\theta \qquad (3.5)$$

where β is the half with at full maxima value for each peak individually.

The dislocation density (δ) was also calculated from the relation.

$$\delta = 15\varepsilon_{str} / aD \qquad (3.6)$$

Where ε_{str} = average strain, a = lattice parameter and D = average grain size.

It has been found that crystals with larger dislocation densities were harder and this hardness factor more important in shape of nanoparticles. The values of dislocation densities for all QDs have tabulated in table 3.3. Results clearly show that as the value of grain size decreases the value of dislocation density increases gradually. This is due to the additional lattice mismatch which implies that lattice imperfection is more in small grains (2.26 nm). Dislocation density suggests that the prepared semiconductor QDs become less ordered and more hardened and as a result, the strength of materials increases with decreasing grain size [215, 216]. Specific surface area "SSA" is a property of solids which tells about the total surface area of a material per unit of mass solid or bulk volume.

It is used to derive value that can be used to determine the type and properties of a material. The SSA is increased as the particle size becomes small. So it is important to measure the specific surface area to evaluate the activity and adsorption capacity of materials (e.g. catalysis and adsorbent). The large SSA of nanoparticles is the origin of a number of

their unique applications. Catalysis is enhanced by high surface area per unit volume and the homogenous distribution of nanoparticles.

$$SSA = SA_{part} / V_{part} \text{ X Density} \quad (3.7)$$

where SA_{part} is surface area, V_{part} is particle volume and density is the value of respective QDs. Apart from using the above equation, Park et al, 2006 were suggested a more convenient formula for SSA calculation of nanoparticles i.e .,

$$S = 6 \text{ X } 10^3 D_p^* \text{ X Density} \quad (3.8)$$

where S is the SSA, D_p is the size of the particles, and at last the density of prepared QDs. The specific surface area of the particles is the summation of the areas of the exposed surfaces of the particles per unit mass. There is an inverse relationship between particle size and surface area. If the particles are assumed to be as spherical and have narrow size distribution, the specific surface area provides an average particle diameter in nanometer SSA values for all QDs have been tabulated in table 3.3.

Table 3.3: Particle size (nm), strain (ε_{str}), dislocation density (δ), specific surface area and surface to volume ratio of 2-Mercaptoethanol capped CdS, ZnS and CdS/ZnS QDs at room temperature.

Sample	D (nm)	ε_{str}	δ [nm]$^{-2}$	"SSA" m^2/g	Surface to volume ratio
C1	3.28	2.16	0.093	379	1.82
C2	3.08	2.58	0.105	404	1.95
C3	2.45	3.82	0.166	508	2.43
Z1	5.5	0.43	0.033	207	1.09
Z2	5.0	0.56	0.040	294	1.20
Z3	4.8	0.64	0.043	306	1.25
CZ1	5.8	0.15	0.029	253	1.04
CZ2	5.5	0.19	0.033	267	1.09
CZ3	5.1	0.21	0.038	287	1.22

3.3.2 Optical characterizations

3.3.2.1 Optical absorption studies

CdS/ZnS is type I core/shell structure: Band gap of the shell (ZnS) is larger than that of core (CdS). The conduction and valance band offset are such that the conduction band of shell is

higher than that of core, while the valance band of the shell has lower energy than that of the core. This leads to an effective confinement of electron and hole in the core material. The exciton behaviour mechanism on the core/shell system and the emission of the fluorescence is illustrated in figure 3.6. The optical band gap of CdS, ZnS and CdS/ZnS has been determined from the absorption spectra. The UV–visible (UV–vis) absorption spectra of CdS, ZnS and CdS/ZnS QDs have been presented in figure 3.7. The absorption edges occur at 475 nm (C1), 427 nm (C2), 420 nm (C3) for capped nano CdS and at 510 nm for bulk CdS QDs (figure 3.7(a)).

Absorption edges exist at 320 nm (Z1), 280 nm (Z2), and 240 nm (Z3) for capped ZnS particles compared to bulk ZnS (350 nm) (figure 3.7(b)). The (figure 3.7(c)) shows a broad blue-green emission in CdS/ZnS capped particles positioned around 300 nm (CZ1), 290 nm (CZ2) and 280 nm (CZ3) respectively. It has also been observed that the capped CdS and ZnS QDs absorb lower wavelength compared to the uncapped CdS and ZnS. It is well known that the band gap and surface area increases with the decrease in the size of the particle [217, 218] and hence the absorption threshold shifts to shorter wavelengths as a result of quantum confinement effect [219]. Also the absorption of light by CdS and ZnS increases by increasing its surface area. At nano sizes, quantum confinement effects can come into play and affect most notably the electronic properties [220].

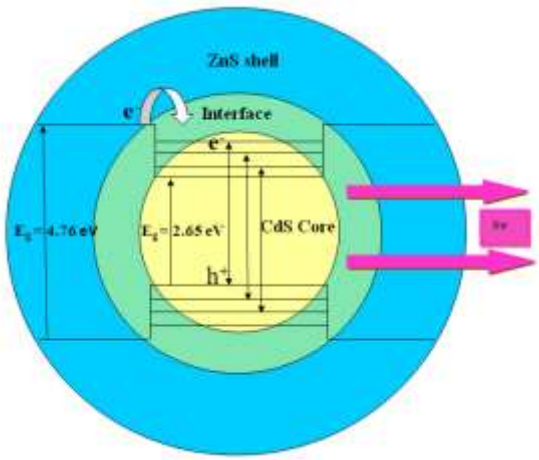

Figure 3.6: Schematic diagram of core/shell structure.

As the size decreases, the absorption of the surface states becomes more intensive and the absorption peak shifts toward blue. This indicates that the contents of the surface states increase as the size of the particles is decreased. As the surface/volume ratio increases, the size decreases and ions at the surface increase rapidly.

Thus the surface states (dangling bonds, defect sites, or traps) increase rapidly via this surface reconstruction. The absorption edges of CdS/ZnS core/shells show a blue shift as compared to CdS. This could be explained as the overall result of the size effect and the potential-well effect. Mismatch of ZnS and CdS results in an asymmetric internal electric field across the interface which affects the electronic states and absorption properties of core/shell nanoparticles.

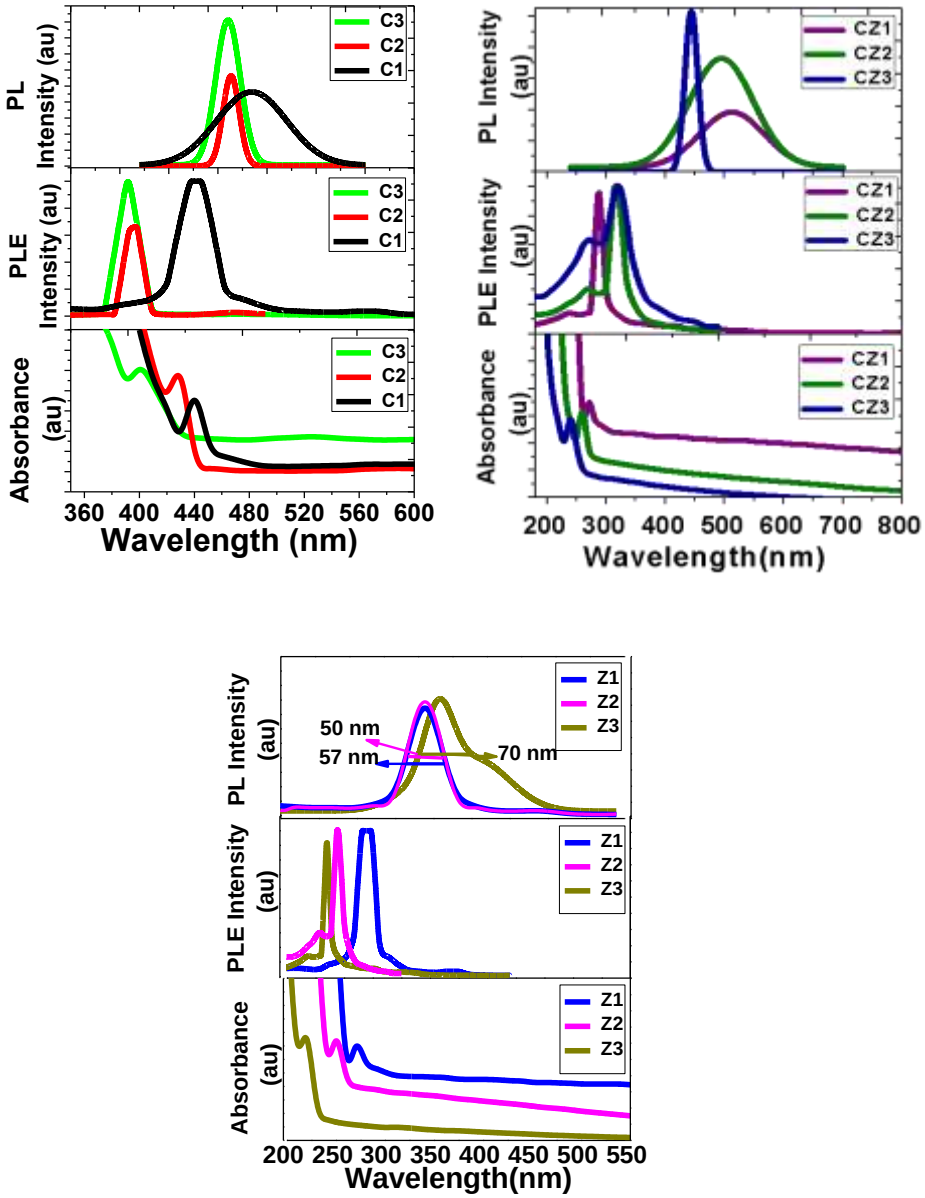

Figure 3.7: Absorption, photoluminescence luminescence excitation and Photoluminesincece spectra of (a) CdS (C1, C2, C3), (b) ZnS (Z1, Z2, Z3) and (c) CdS/ZnS (CZ1, CZ2, CZ2) QDs.

The optical band gap of CdS, ZnS and CdS/ZnS nanoparticles can be determined from the absorption spectra with the help of Tauc plot. In Tauc region (high absorption region) the absorption is due to inter band transition among extended states in both valence and conduction bands. The absorption coefficient depends on optical band gap [209] and given by

$$\alpha h\nu = K\left(h\nu - Eg\right)^{n} \qquad (3.9)$$

where E_g represents the optical band gap, K is a constant, and n depends on the nature of the transition with values of 1/2, 3/2, 2, and 3 for allowed direct transitions, forbidden direct transitions, allowed indirect transitions and forbidden indirect transitions, respectively.

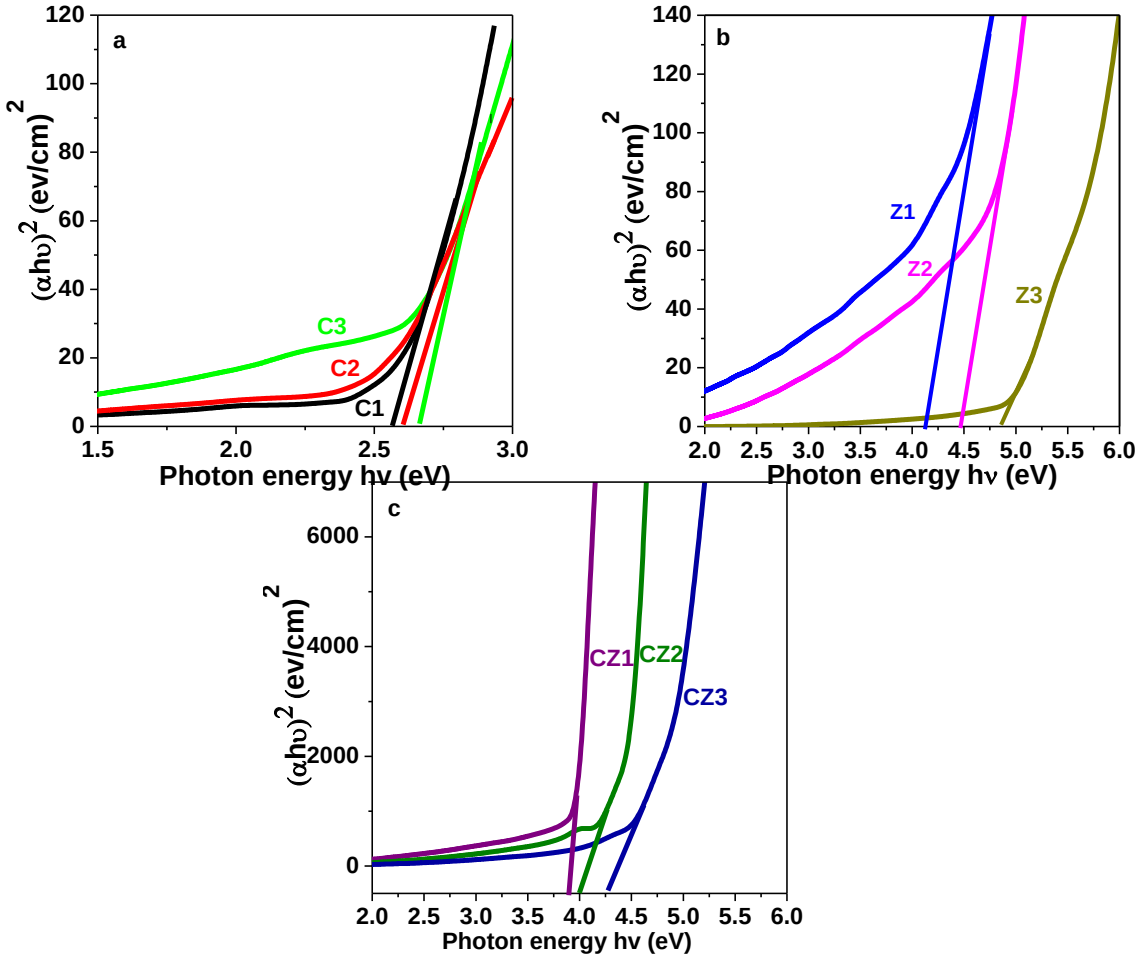

Figure 3.8: Tauc plot $(\alpha h\nu)^2$ vs hν of (a) CdS (C1, C2 and C3), (b) ZnS (Z1, Z2 and Z3) and (c) CdS/ZnS (CZ1, CZ2 and CZ3) QDs.

The absorption coefficient (α) was determined from the relation $A=I/Io=e^{(-\alpha d)}$, or can be calculated using the well-known relation deduced from Beer–Lambert's relation [221, 222].

$$\alpha = 2.303A/d \qquad (3.10)$$

where *d* is the path length of the quartz cuvette and *A* is the absorbance determined from absorbance spectra [223]. It is well known that the CdS and ZnS are direct band gap semiconductors; hence the direct band gap value can be estimated from the plots of $(\alpha h\nu)^2$ vs $h\nu$ and extrapolating the straight portion of the graph to $h\nu$ axis as shown in figure 3.8 (a, b, & c). The absorption edge of the optical energy band gap of CdS, ZnS and CdS/ZnS nanostructures have been calculated using the formula

$$E_{eV} = hc/\lambda \qquad (3.11)$$

where *h* = Planck's constant and *E* = energy band gap of the semiconducting nanoparticles . The optical absorption edge and the calculated band gaps have been shown in the Table 4. It has been noticed that the values of the band gaps are higher than that of bulk values of CdS (2.4eV) and ZnS (3.9 eV) [37] indicating the strong quantum confinement. The band gap energies gradually increase from 2.65 eV to 2.79 eV in case of CdS and from 4.23 to 4.73 eV for ZnS. These changes have been attributed to the crystallite size-dependent properties of the energy band gap. The increase in band gap with increase in molar concentration of the capping agent is attributed to size quantization effect due to the small size of the particles [224]. The estimated optical band gaps for CdS/ZnS core/shells were about 3.02 and 2.98 eV for low and high shell thicknesses respectively which show around 1.22 and 1.26 eV red-shift compared to ZnS core nanoparticles (E_g ~ 4.24 eV). Absorption edges of CdS, ZnS and CdS/ZnS QDs with their original and tuned band gaps are listed in table 3.4.

Table 3.4: Absorption edges of CdS, ZnS and CdS/ZnS QDs with their corresponding original and tuned band gaps.

Sample	**Absorption edge**	**Band gap in eV**	**Optical band gap**	**Increment in band gap eV**
CdS Poly	510	2.42	2.65	-----
C1	480	2.58	2.69	0.16
C2	465	2.66	2.79	0.24
C3	450	2.75		0.33
ZnS Poly	350	3.54		----
Z1	340	3.64	4.13	0.10
Z2	330	3.75	4.43	0.21
Z3	300	4.13	4.73	0.59
CZ1	300	4.13	3.91	
CZ2	290	4.27	4.00	
CZ3	280	4.42	4.30	

On the other hand, various theoretical approaches have been employed to account for the variation in the electronic structure of nanocrystallites as a function of their size viz effective mass approximation (EMA), the tight-binding approximation (TBA) and hyperbolic band model (HBA), In the present study data was fitted for three different models and the particle size has been calculated to show which electronic model fitted exactly to particular QDs. In most EMA calculations, the confining potentials for the electron and the hole have been assumed infinite. In the strong confinement regime: *R* the nanocrystal radius is much smaller than a_B (Bohr exciton radius). The results obtained in the case of core/shell systems have resemblance with ZnS QDs. And due to this effective mass of electron and hole of ZnS in all theoretical models been assumed in many other studies, use of average effective mass of electron and hole or according to the behavior of wave function were considered [225]. Particle sizes were estimated from the band gap values using Brus equation by effective mass approximation (EMA) [226]

$$E_R = Eg + \frac{\hbar^2}{2m_o R^2}\left[\frac{1}{m_e*} + \frac{1}{m_h*}\right] - \frac{1.8e^2}{4\pi\varepsilon_0\varepsilon_r R} - 0.248\frac{4\pi^2 e^4 m_0}{2(4\pi\varepsilon_0\varepsilon_r)^2 h^2\left(\frac{1}{m_e*} + \frac{1}{m_h*}\right)} \tag{3.12}$$

$$r = \frac{-\left(\frac{1.8e^2}{4\pi\varepsilon\varepsilon_0}\right) + \sqrt{\left(\frac{1.8e^2}{4\pi\varepsilon\varepsilon_0}\right)^2 + \left(E_g^{nano} - E_g^{bulk}\right)\frac{h^2}{2m_0}\left(\frac{1}{m_e^*} + \frac{1}{m_h^*}\right)}}{2\left(E_g^{nano} - E_g^{bulk}\right)} \tag{3.13}$$

where E_g is the bulk band gap. The second term (eq.3.12) is the kinetic-energy term containing the effective masses, m_e* and m_h*, of the electron and the hole, respectively. The third term (eq.3.12) arises due to the Coulomb interaction between the electron and the hole, and the fourth term is due to the spatial correlation between the electron and the hole which is generally small compared to the other two terms. The obtained results from EMA nearly matches with the size obtained from XRD and approve the results attained experimentally and theoretically.

The TBA scheme has been employed by a number of researchers over the past decade. The parameters for CdS and ZnS used in the calculation are tabulated in table 3.5 [48, 50].

$$\Delta E = a_1 e^{-\frac{R}{b_1}} + a_2 e^{-\frac{R}{b_2}} \tag{3.14}$$

The TBA method has the further advantage of being significantly less demanding in terms of computational efforts, besides providing a simple physical picture in terms of the atomic orbitals and hopping interactions defined over a predetermined range. The size of QDs that has been calculated by TBA is approximately not similar to experimental calculation shown is table 3.1.

Table 3.5: Used Parameters for TB calculations.

Parameters	ZnS	CdS
a1	7.44	2.83
a2	2.35	8.22
b1	3.04	1.96
b2	15.30	18.07

To overcome the short comings of parabolic band approximations, the hyperbolic HBA has been proposed. The main improvement of the hyperbolic band model over Brus model is the inclusion of the effect of electron and hole band non-parabolicity. In this model, the hole and electron bands are hyperbolic, but approach the parabolic behavior at the G point of the Brillion zone. The Coulomb corrections to the overall band gap shift are presumed to be small and are neglected within this model.

$$E_g(R) = \sqrt{E^2{}_g + \frac{2\hbar^2 E_g \pi^2}{m_0 R^2}\frac{1}{2}\left(\frac{1}{m_e^*} + \frac{1}{m_h^*}\right)} \qquad (3.15)$$

$$R = \sqrt{\frac{2\pi^2 h^2 E_{gb}}{m^*\left(E_{gn}^2 - E_{gn}^2\right)}} \qquad (3.16)$$

where R is quantum dot radius ($2R$ is the diameter and hence the particle size). E_{gb} is the bulk band gap, E_{gn} is quantum dot band gap, h is Planck's constant and m^* is effective mass of specimen (1.82 x 10^{-31} kg for CdS and 3.64 x 10^{-31} Kg for ZnS). The values of the average particle sizes calculated from XRD and EMA are in good agreement in case of exciton Bohr radius (a_B ~ 2.5 nm) for ZnS and CdS/ZnS QDs case but week confinement regime in CdS QDs. It has been found that only little number of reports is available on core/shell materials that have been analysed by EMA, HBM and TBA theoretical models [227-231]. It has been reported that EMA overestimates the size of particles smaller than 5.0 nm, but gives the true average particle size for larger particles size distribution [232-234].

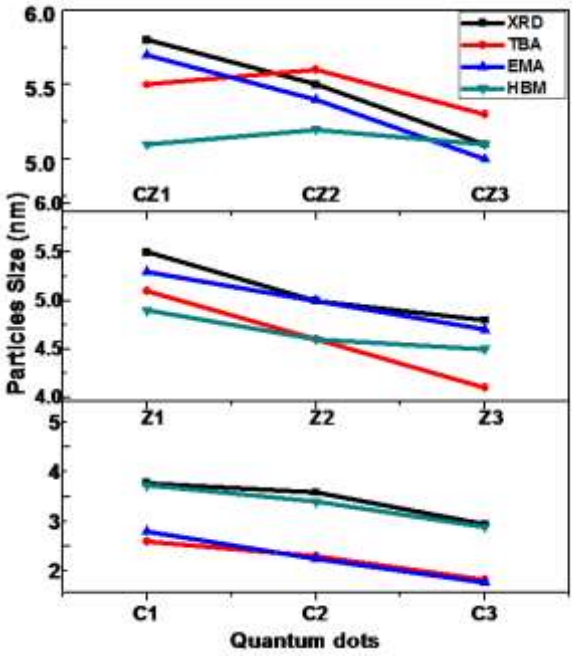

Figure 3.9: Best fitting of particle size calculated by XRD and different theoretical models such as EMA, TBA and HBA.

Nevertheless, particle sizes determined using EMA are in good agreement with the crystallite sizes obtained from XRD in ZnS and core/shell particles. The band gap of the CdS nanoparticles is a function of size in TBA as well as EMA. The experimental data agree well with effective mass calculations for diameters larger than 4 nm, where as TBA fit better for particles with diameters smaller than 4 nm [48]. Murakoshi et al have reported that the experimental data for the dependence of band gap with particle size agrees well with EMA with a finite potential well, even for smaller sizes [235]. The HBM gave smaller average particle sizes for the capped ZnS nanoparticles when compared to the particle sizes estimated from EMA. This variation in particle sizes has been reported elsewhere. All calculated values using different models resemble very closely with experimental data but fitted more precisely with TBA model. Particle sizes of all QDs calculated by three models are shown in (figure (3.9)).

3.3.2.2 Photoluminescence studies

The photoluminescence (PL) originates from electrons in the conduction band, excitonic states and recombination of charge carriers in deep traps of surface defect states [41,236]. Therefore, the appreciable attention has been paid to prevent the agglomeration of QDs in order to improve their photoluminescence properties [237]. Theoretical results point out that

a breaking symmetry process in the structure of various semiconductor associated to order–disorder effects is a necessary condition for the presence of intermediate levels in the forbidden band gap [238]. The main point for quantum confinement occurs is the presence of discrete levels in the band gap [239].The luminescence properties of 2-mercaptoetnanol capped CdS, ZnS, CdS/ZnS QDs examined by PL and PL excitation (PLE) and have been shown in figure 3.7 (a, b and c). PL spectra were recorded at an excitation wavelength of 220 nm, and PLE spectra were recorded at the wavelength of the fluorescence maximum. The PLE spectrum following the absorption of "large" particles shows a little red-shift from the average absorption of the whole particle distribution. We can see from the excitation spectrum that the excitation at the energy of the lowest excited state in CdS nanoparticle matrix is most efficient for the emission and the excitation efficiency decreases largely at higher energies. This indicates the efficient energy transfer from the lowest excited state of QDs. It is well known that surface defect states play important roles in the luminescence properties of nanoparticles, which act as radiative or nonradiative centers in nanoparticles [240]. The PL spectrum of the CdS nanoparticles was dominated by very strong and narrow emission peak at around 420 nm for C3 with larger fluorescence intensity. The strong emission was attributed to deep trap sites due to the sulfur vacancy. The fluorescence spectrum of capped CdS nanoparticles showed similar features as that of CdS nanoparticle for CdS (C2) at 430 nm and 475 nm for CdS (C1) with slightly small fluorescence intensity. In the case of CdS QDs, it was reported [35, 41] that the high energy emission band (350-500 nm) was due to the radiative recombination of free charge carriers or excitonic fluorescence while low energy PL peak (500-700 nm) was attributed to the recombination of charge carriers in deep traps of surface defect states. The fluorescence enhancement may be attributed to a much higher concentration of radiative recombination centers. The PL intensity of 2-mercaptoethanol capped particles is dramatically enhanced which indicates complete removal of the surface defect. In addition the surfactants capped particles significantly show blue shifted with respect to uncapped particles which is due to reduction of the particles size.

PL spectra for ZnS were recorded at an excitation wavelength of 220 nm and PL excitation spectra were normalized to the intensity of the first exciton absorption peak, which allowed a direct comparison between PLE and absorption (figure 3(b). For ZnS QDs cores, the PLE spectrum and absorption spectrum were highly consistent and exhibited similar

excitonic features. The peaks positioned around 423 nm, 430 nm, 480 nm and 510 nm are due to the shallow state near the conduction band and the sulphur vacancies present near the valance band [241]. It is observed that the photoluminescence efficiency of capped ZnS QDs with higher concentration of 2-mercaptoethanol show high intensity due to passivation of surfaces [242]. The blue emission at 485 nm is attributed to sulphur vacancies [243] and the emission peak at 465 nm is attributed to the zinc vacancies which is quite similar as reported by other workers [244, 245]. Further, the narrow emission bandwidth of the samples indicates a relatively narrow size distribution of the particles [246]. Obviously, the broad and Stokes-shifted emission band (so-called trapped luminescence) arises from the surface states. It can be seen that the surface emission becomes more intensive and shifts toward the blue as the size of the particles is decreased. The size dependence of the surface emission is in agreement with that of the long wavelength absorption band in figure 3(b). Excitation and emission spectra for as prepared CdS/ZnS QDs have been recorded (figure 3(c)) in which a broad emission band and a narrow gaussian excitation band have been observed. After the growth of ZnS shells on CdS, the PLE spectrum deviated slightly from the corresponding absorption spectrum especially at the short wavelength side of the first-order excitonic feature. This can be explained by the different shell contributions to PLE and absorption [247]. PL spectra of 2-mercaptoethenol capped CdS (C3), ZnS(Z3) and CdS/ZnS (CZ3) QDs under 220 nm excitation were shown in figure 3.10 for comparison.

The PL spectrum of the CdS shows a red maximum emission around 420 nm and a blue maximum emission for ZnS around 470 nm. The PL spectrum for the CdS/ZnS (C3, Z3, CZ3) presents the maximum emission around 445 nm. The blue-shift has been observed for the CdS/ZnS compared to CdS and could be explained for the possible presence of the ZnS disordered shell coated on the surface of CdS core. Another interesting effect in PL spectra is the enhancement in the emission for the CdS/ZnS which can be associated with an interband connection between the interface of CdS core and ZnS disordered shell. ZnS confines the photogenerated electron–hole pairs to the CdS core interface modified by the quantum confinement effect, leading to the passivation of non-radiative transitions and enhancing the luminescence intensity. Structures show much distortion in lattice and this phenomenon can be related to local, intermediate and long-range structural array–disarray [10]. The peaks are also assumed to originate from the radiative recombination of carrier at surface trap states resulted from the compounded effect of CdS at CdS/ZnS interface. The significant reduction in FWHM in emission peaks of smallest particle size in each set of samples *i.e* from 168 nm

to 41 nm in case of CdS, from 70 nm to 50 nm in case of ZnS and from 129 nm to 30 nm in case of CdS/ZnS QDs respectively.

The stability in prepared samples has been tested and presented by comparision of fresh and old samples. CdS, ZnS and CdS/ZnS samples were prepared initially in consecutive 2 days and were reserved in distilled water in a closed vial in normal atmospheric conditions in a clean bench away from direct sunlight. Fresh samples were prepared in summers (room temperature 35–37 ^{o}C), and PL spectra have been recorded immediately. To test the stability, the PL spectra of stored samples have been recorded again after 6 months at that time the room temperature was 25–30^{o}C. Six month aged samples of CdS, ZnS and CdS/ZnS as shown in Figure 3.10 have also been analyzed, and it confers approximately the same luminescence as fresh samples. It indicates that there is no more agglomeration exists in the QDs on ageing, and a stable wurtzite structure has been achieved. Also it is clear from the figure 3.10 that there is a negligible change in emission intensity in all the samples. Hence results indicate the effectiveness of the synthesis procedure and the use of capping agent to stabilize the QDs.

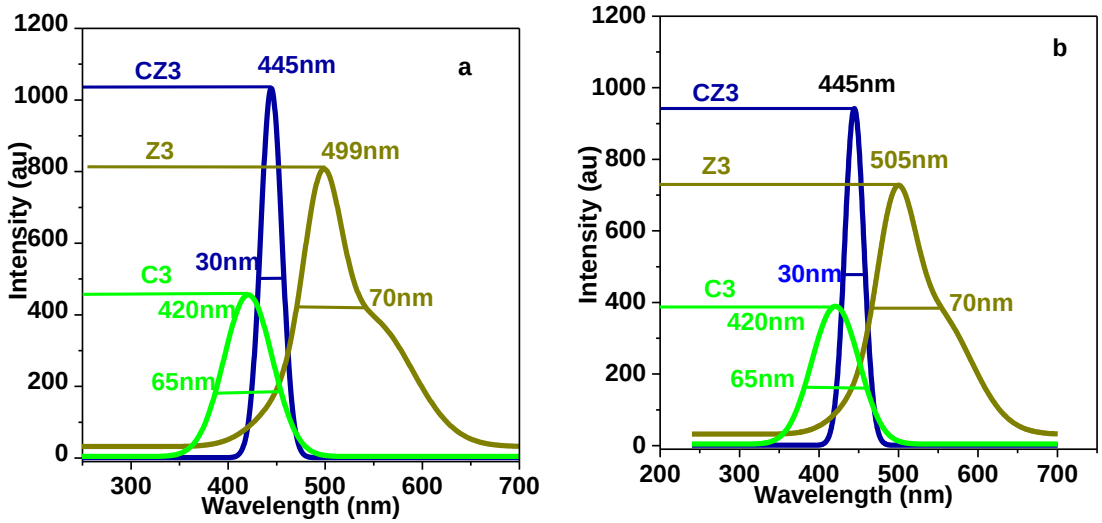

Figure 3.10: Comparative room temperature photoluminescence spectra of C3, Z3 and CZ3 QDs (a) fresh sample and (b) 6 months aged samples.

3.3.3 Fourier transforms infrared spectroscopy (FTIR) analysis

2-mercaptoethanol capped CdS, ZnS, CdS/ZnS QDs were examined by recording their FTIR spectra in the range 4500–100 cm^{-1} (figure 3.11). The broad peak at 2120, 1383 cm^{-1} and the

weak peak at 1614 cm^{-1} were assigned to C=C , C-H characteristic vibrations in the CdS sample as marked shown in the spectra. The sharp peak at 3365 cm^{-1} corresponds to (O-H) alcohols and 1119 cm^{-1} show (C-N) amines along with two small peaks at 1626 cm^{-1} for (N-H) amines and 1401 cm^{-1} for O-H means carboxylic acid in ZnS samples, similar peaks occured in CdS/ZnS QDs. These results shows how effectively ZnS covers the CdS core and reduce the toxicity of CdS materials as ZnS is nearly non toxic for bio molecules.

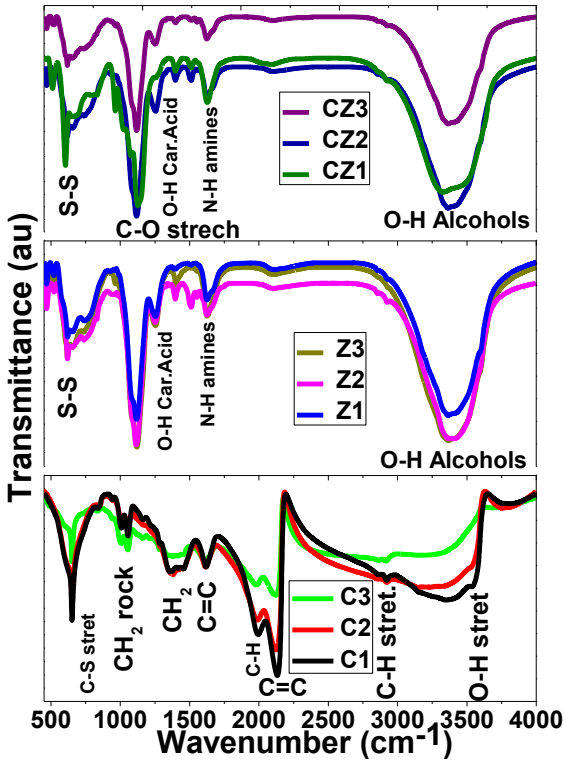

Figure 3.11: FTIR spectra of capped CdS, ZnS, CdS/ZnS QDs with their functional groups.

The functional groups that are present on the surface of the prepared samples can be easily attached with bio molecules. Generally OH (Hydroxyl), COOH (carboxylic acid) or amine functionalities are present on the bio molecules surfaces [248-250] and similar functional groups are also present in our as prepared QDs. So the prepared QDs have enough compatibility to attach with bio molecules. ZnS present at the shell which is nontoxic and gives more opportunity to apply CdS/ZnS structure for bio-application viz bio imaging etc. Here one important point is worth mentioning that: we have opted for aqueous medium to prepare luminescent QDs, as results there are always hydrophilic surfaces of QDs which are directly conjugable to bio molecules. This is a plus feature of our technique as the QDs prepared by high temperature organic synthesis routes are always possessing hydrophobic surfaces and needs to other additional surface processing steps before bioconjugation.

3.3.4 Transmission electron microscopy

The particle sizes of CdS (C3), ZnS (Z3) and CdS/ZnS (CZ3) QDs have been determined by TEM to make sure the effectiveness of stabilizer and the results are presented in figure 3.112.

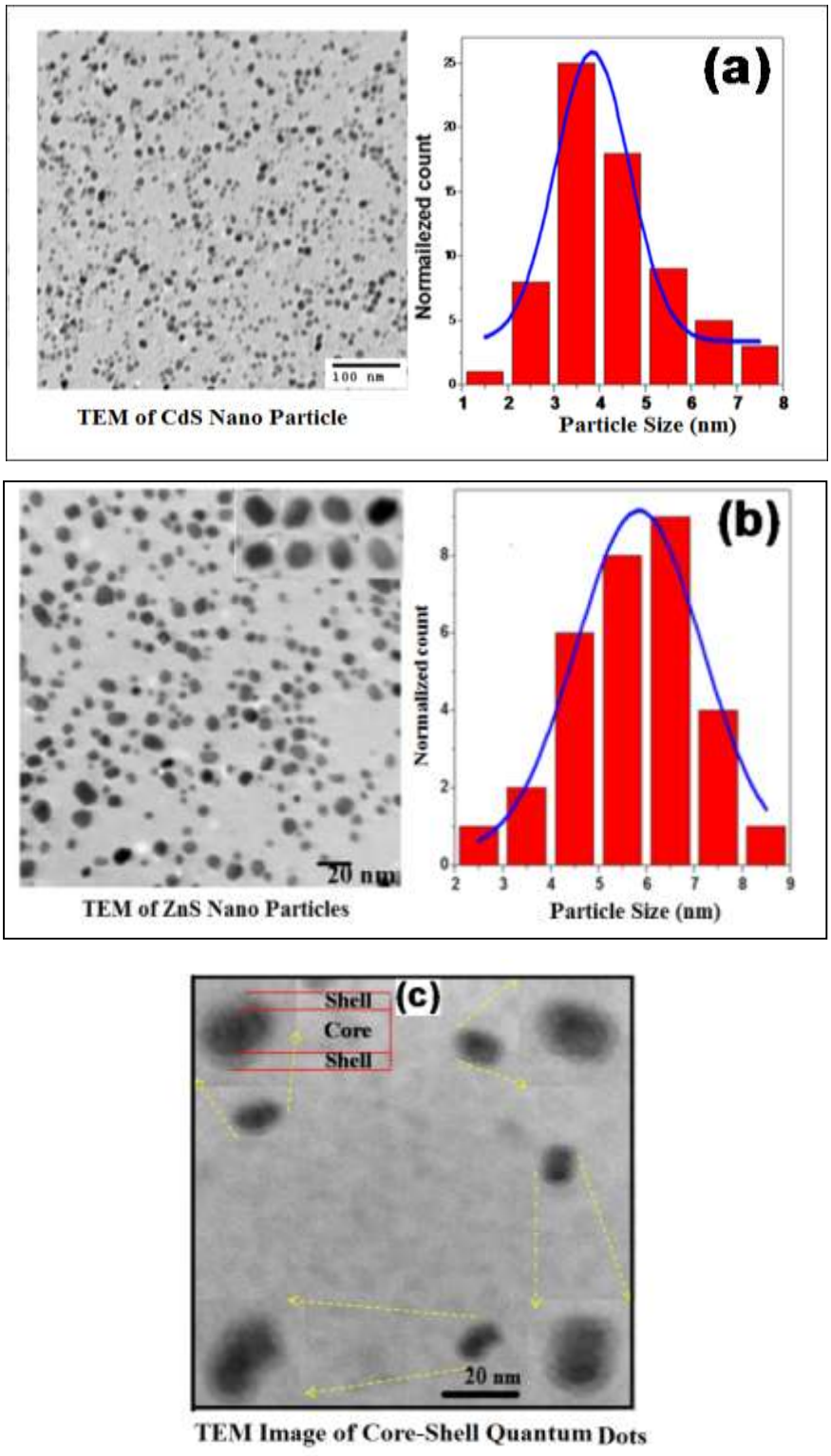

Figure 3.12: TEM images of capped (a) C3, (b) Z3 and (c) CZ3 QDs.

TEM image (figure 3.12(a)) of the CdS QDs shows highly monodispersed nanoparticles with average sizes of 3.8 nm as vindicated from the corresponding histogram. Similarly ZnS QDs (figure 3.12(b)) with 6 nm and CdS/ZnS QDs (figure 3.12(c)) have 6.2 nm particle sizes. It is also clear from the figure that there is no agglomeration of QDs and we can obtain either the fine solution or even powder of uniformly distributed nanoparticles for various applications. The particle size calculated from effective mass approximation using absorption data is comparable to the size obtained from XRD data, whereas the particle sizes obtained from TEM are slightly greater than the size obtained from XRD analysis. The size obtained by XRD and TEM has the correlation that the XRD size is usually equals or smaller than the size obtained by TEM [251].

When the particles are delineated by well-defined boundary or loose nanoparticles of materials XRD and TEM values are in good agreement. In bulk nanocrystalline materials produced by various methods and the XRD result is usually smaller than TEM size. On the other hand, in nanocrystalline materials, the term grain is used interchangeably with crystallite to refer to the smallest single-phase and crystallized regions separated by grain boundaries. Each crystallite is itself a "single crystal" as such; it can contain any or all of the zero-, one-, or two-dimensional defects except for grain boundaries, interphase boundaries and surfaces. .

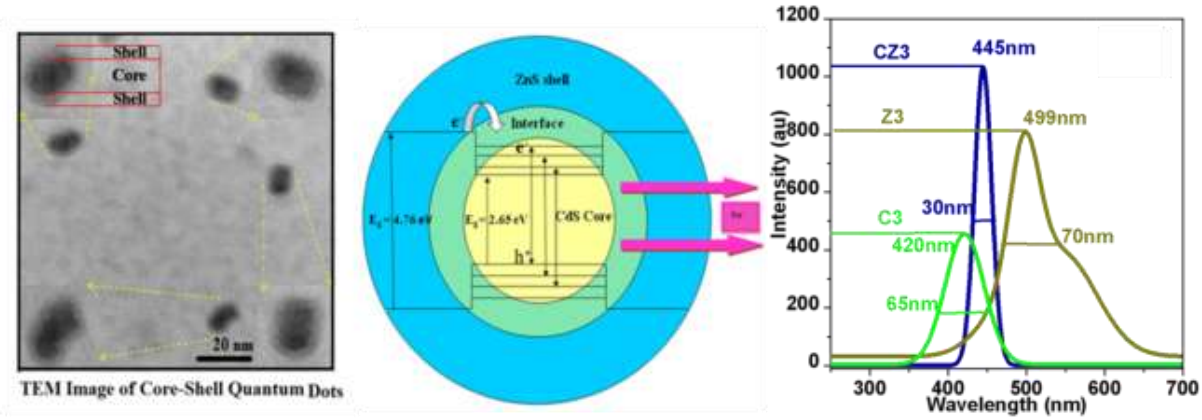

Figure 3.13: TEM image of CZ3, schematic and PL emission spectra of capped CZ3 QDs.

In the present work particle size of all prepared QDs have been calculated with XRD and TEM, and then verified by EMA (using absorption data). Moreover, the particle size also been computed with two another models TBA and HBM. In our previous study we have reported particle size calculated by XRD, TEM and William–Halls method and found analogous. On the basis of those findings we have concluded that the particle size obtained

from XRD, TEM and different models are comparable to other methods hence the reported results are adequate to confirm the particle size [251]. Consequence of size/shell thickness attained in wurtzite CdS/ZnS quantum dots (QDs); analysed for excellent luminescence with brilliant monochromaticity and bioconjugatable functional groups on QDs surface shows in Figure 3.13.

3.4 CONCLUSIONS

The CdS, ZnS and CdS/ZnS QDs whose emission spans most of the visible spectrum have been described which have been synthesized using wet chemical growth method. Their structural as well as optical properties have been investigated by XRD, UV-Vis spectroscopy, photo luminescence spectroscopy, FTIR and TEM. XRD results indicated that lower synthesis temperature resulted in lower grain size and less strained particles. The ZnS shell appears on CdS QDs properly covered and creates dislocations or other defects to accommodate the mismatch in lattice constants between ZnS and CdS. The influence of surface passivation on the optical properties has also been evaluated. The UV-Visible spectra show a large blue shift attributing the enhanced optical properties, this size dependent blue shift in absorption edge is attributed to the quantum size effect. PL measurements show effectiveness of capping and core/shell structure formation as there is clear vindication of drastically enhanced luminescence. In summary, highly luminescent, nearly monodispersed CdS, ZnS and CdS/ZnS QDs has been prepared. The particle sizes of CdS, ZnS and CdS/ZnS QDs as determined from XRD and TEM images were in good agreement. Core/shell semiconductor QDs that were prepared by our method are low-cost, safe, and environmental friendly. Color tunable CdS, ZnS and CdS/ZnS QDs were created which are monodispersed possessing high stability and; narrow PL spectra that indicate superior monochromaticity. This method can also be applicable to synthesize the other tunable, monochromatic core/shell semiconductor QDs.

CHAPTER – IV

CONTROLLED DEVELOPMENT OF INVERTED ZnS/CdS CORE/SHELL QUANTUM DOT STRUCTURES AND MULTISHELL ZnS/CdS/ZnS QUANTUM DOT STRUCTURES

Wurtzite ZnS/CdS/ZnS multishell quantum dots have been prepared with extended potential barrier by varying shell thickness at low temperature. These multishell quantum dot structures provide high luminescence with narrow emission width and effective tunability due to narrow size distribution of multishell quantum dots.

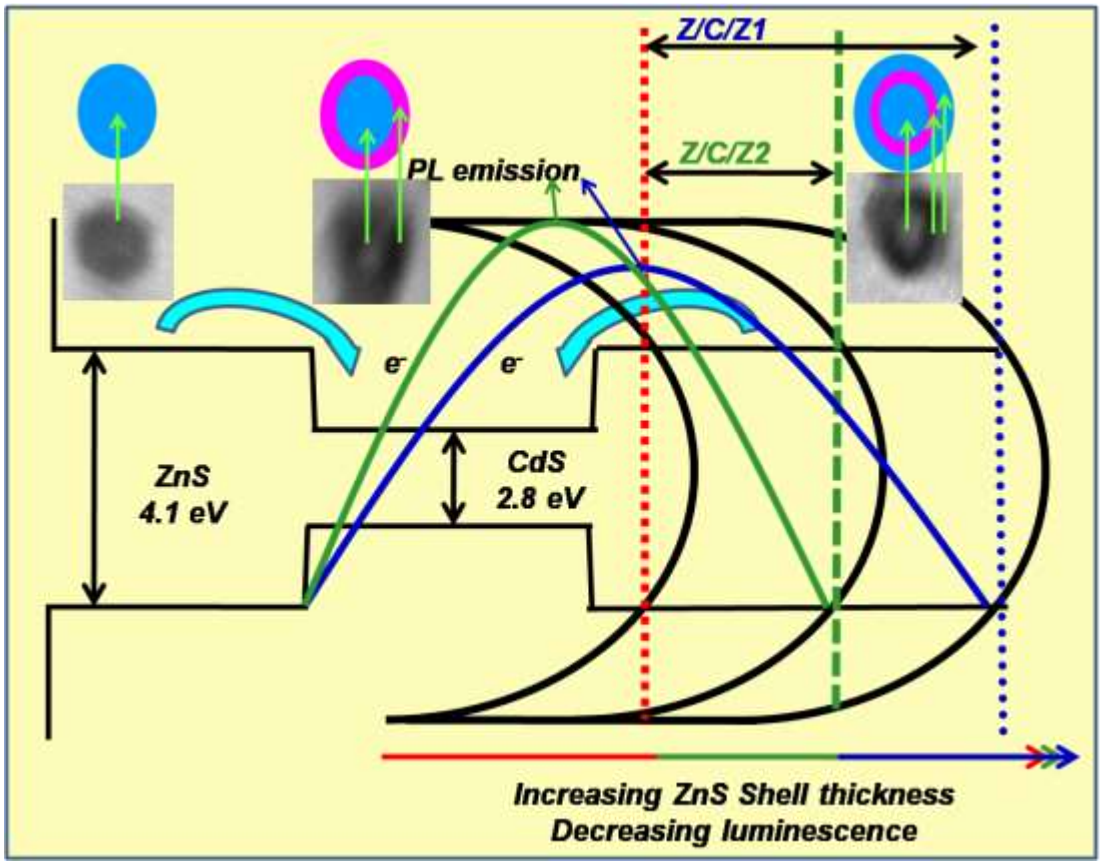

4.1 INTRODUCTION

Inverted quantum dots (QDs) synthesized using wet chemical route are a class of materials which are actively being explored because of their amendable optical and electronic properties. QDs are extremely valuable class of materials in various applications such as light emitting diodes, photovoltaic devices, lasers, biological labeling, etc. [4, 5]. The optical and structural properties of these materials can be modified by controlling the size of QDs [6]. In general in all types of core/shell QDs (e.g. CdS/ZnS), shell increases luminescence by passivating the surface trap states. Besides that the shell provides protection against environmental changes, photo-oxidative degradation, and another route for modularity. Strict control of the size, shape, narrows FWHM (Full Wave of Half Maximum); high fluorescent output, and good monodispersity achieved by core/shell QDs. These materials have found good applications in biological systems. In such core/shell QDs, the shell provides a physical barrier between the optically active core and the surrounding medium, thus making the core/shell less sensitive to environmental changes and giving rise to a strongly enhanced fluorescence. These effects are fundamental conditions for the use of core/shell QDs in applications such as biological labeling and light-emitting devices, which depend on their emission properties. Specifically in inverted core/shell structures a core of a wide-gap semiconductor is over coated with a shell of a narrower gap material. The core and shell enable the emission wavelength to be tuned over a wider range of wavelengths than with either individual semiconductor. These “inverted” QDs provide capabilities for controlling functionalities by a direct control of the distribution of electron and hole wave functions and the e-h overlap integral specifically, by increasing the thickness of the QDs shell for a fixed core size [7]. Enhancement in the PL emission intensity is due to localization of the e-h pair [8-10]. It implies that the wave function of electron and hole may be spatially separated in core and shell, reducing the probability of non-radiative decay in the surface states and trap sites [11]. This behavior of ZnS/CdS is attractive in terms of the localization of e-h pair which is relatively extraordinary from the other core/shell QDs. Several different combinations of core/shell QDs such as CdSe/ZnS, CdS/ZnS, ZnO/ZnS, ZnSe/ZnS, CdSe/CdS, CdS/PbS, and ZnSe/CdS have previously been studied by different groups [12, 13]. Some reports [252-255, 96] on inverted ZnS/CdS have also been available but few of them are completely theoretical and in remaining the method of synthesis and approach is different. The inverted hexagonal ZnS/CdS QDs will be

useful where enhancement and tuning of optical properties is needed along with eco-friendly and biocompatible properties [256]. A possible growth mechanism for these promising QDs is being proposed in this chapter.

Particularly, scientists give more attention to QDs; core/shell QDs and multishell QDs because these classes of semiconductor nanocrystals will lead to a series of novel optical and electronic properties [15, 16]. The core/shell CdS/ZnS structures [17, 18] and multilayer structures of CdS and ZnS (CdS/ZnS) [19-20, 257-258] have attracted much attention nowadays, since the optical properties can be enhanced and the band gap can be tuned by the surface chemical bonds and charge transfer in the surface/interface region of QDs and multishell structures. These kinds of structures with unique properties can be prepared by a chemical or physical process, and some new and enhanced physical properties were found due to the core shell interface effects [22, 23]. Numerous investigations have focused on forming the multishell QDs by sandwiching the low band gap material in the well between the layers of quantum dots of higher band gap material viz. ZnS/PbS/ZnS [24], CdS/HgS/CdS [259] and ZnS/CdSe/ZnS [25]. Literature states that when the low band gap material over coated with high band gap materials formed core/shell sort of QDs or multishell which exhibit high photoluminescence intensity as a result of elimination of surface nonradiative recombination [26]. The negative effects of defect states and passivating ligand are commonly eliminated upon coating of QD cores with an inorganic shell made of a material with a higher band gap. Here, we suggest a procedure for obtaining highly luminescent QDs based on charge carrier confinement engineering. Specifically, here we propose a novel multishell ZnS/CdS/ZnS QD structure, which benefits from both high confinement potential of the first monolayer thick ZnS layer and overall moderate shell thickness sufficient for reliable protection of excited carriers from the environment but not greatly increasing the QD diameter sufficiently [260].

In prepared structures, the size of core (ZnS/CdS) was kept fixed with variable shell thicknesses by controlling the size of shell using different cappent ratio of 2-mercaptoethanol *i.e.,* 1ml and 2ml. Surface modification of narrow band gap material (CdS) that is enclosed by wider band gap material (ZnS) can alter the charge, functionality and reactivity of the material. Consequently enhance the PL emission due to localization of the e-h pair [8- 9, 25, 10]. Thus it implies that the wave function of electron and hole may be spatially separated in core and shell,

reducing the probability of non-radiative decay in the surface states and trap sites [11]. One more interesting point of the presented work is that as we coat core ZnS/CdS with ZnS in presence of 2-mercaptoethanol, the introduction of ZnS can greatly passivate the CdS surface to protect it from oxidation and prevent CdS leaching into the surrounding medium [152, 261].

The highlight and novelty of the presented work is to form and analyze the structural as well as optical properties of luminescent wurtzite ZnS/CdS/ZnS multishell QDs. It has been found that few other also synthesized ZnS/CdS/ZnS with different method viz. PL), chemical method in an air atmosphere. Beside this, many authors have also been reported on ZnS/CdS/ZnS multishells but they have opted for different synthesis methods and the particles were of cubic structures [27]. Very few workers have reported the fabrication of wurtzite ZnS/CdS/ZnS, different structures and methods of were used on high temperatures [28, 29]. In this report we propose a simple and cost effective wet chemical method which is very effective method to form the wurtzite multishell with good size controllability. An attempt has been made to change the functional groups at the surface of prepared QDs which helps to accommodate these QDs in bio-application purposes. We have employed X-ray diffraction (XRD), UV–Vis spectroscopy, photoluminescence spectroscopy (PL), Fourier transform infrared spectroscopy (FTIR) and Transmission electron microscopy (TEM) techniques to characterize ZnS, CdS, ZnS/CdS core/shell and ZnS/CdS/ZnS multishell QDs.

4.2 RESULTS AND DISCUSSIONS

4.2.1 Luminescence and absorbance studies

4.2.1.1 ZnS/CdS QDs

Wet chemical method was adopted for synthesis of core and core/shell QDs. Size of core was retained steady with altering shell thicknesses (by controlling the size of shell QDs) in order to obtain series of inverted ZnS/CdS QDs. For convenience we named ZnS/CdS capped with 1 ml, 2 ml and 4 ml 2-mercaptoethanol as ZC1, ZC2, and ZC3 respectively. It is clear from the PL spectra of ZC2 and ZC3 core/shell QDs that there is increment in luminescence (shell thickness is of the order ZC1>ZC2> ZC3) with an effectively tuned PL emission (figure 4.1(a)).

In case of ZC1 where the shell thickness is maximum the emission intensity is minimum. While on reduction of shell thickness in ZC2 (intermediate shell thickness) and ZC3 (minimum shell thickness) the PL emission intensity increases but surface defects also increases. This is due to the delocalization of wave functions of electron and hole in ZC1 and PL spectra shows maximum emission at 466 nm in ZC1 QDs. In case of ZC2, the wave function of electron and hole most probably localized in shell and PL emission shown maximum intensity at 455 nm in ZC2 QDs. PL spectra of ZC3 shows overlap regime which indicates proper shell thickness can provide a mode for electron and hole distribution in whole system. This overlapping and localization of electron-hole in core/shell can lead to the better PL enhancement and fine tunability and PL spectra shows maximum emission at 430 nm in ZC3 QDs. PL spectrum of ZC3 shows approximately 2 fold enhancement in emission intensity in comparison to ZnS core with over all 70 nm spectral shift. So by the variation of shell (CdS) we can easily increase the quantum efficiency.

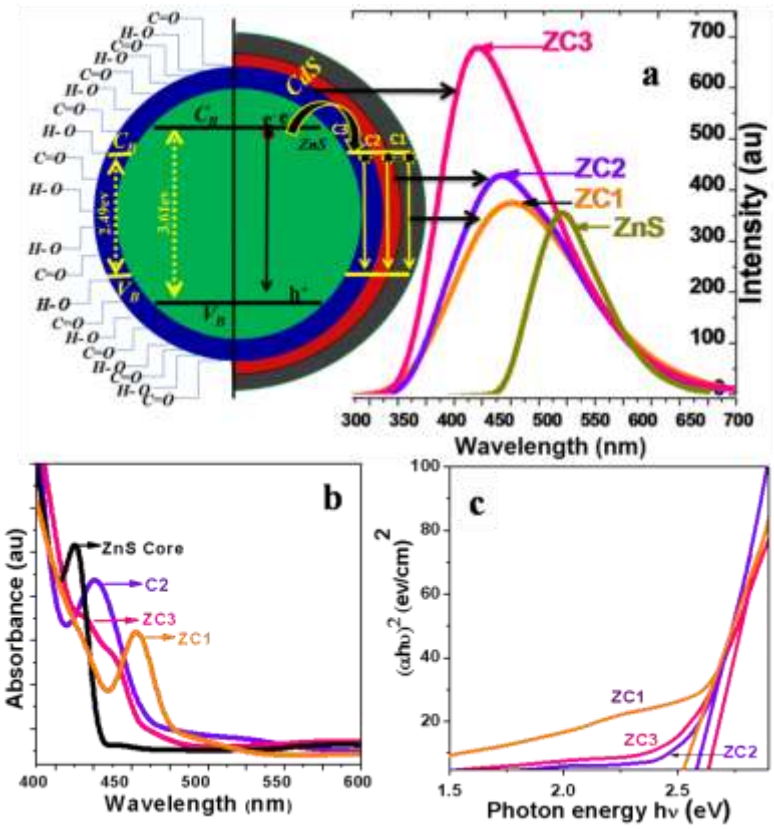

Figure 4.1: (a) Photoluminescence spectra for ZnS, ZC1, ZC2 and ZC3 QDs. (b) absorption spectra of ZnS core and ZC1, ZC2 and ZC3 QDs and (c) band gap plot for ZC1, ZC2 and ZC3 QDs.

In ZC1 and ZC2 the transition occurs only in the shell because the thickness is very high but in ZC3 the shell becomes very thin, due to this, core transition may play a Small role in transitions. Transition scheme and the functional groups present at the surface of prepared QDs due to the use of CdS shell and capping agent (2-mercaptoethanol) are presented in the figure (4.2). This kind of alteration in optical properties can only possible with shell of different sizes. Additionally in particular by increasing the thickness of the shell one can continuously tune the carrier localization regime [262]. ZnS/CdS QDs that were prepared by our method are cost effective, safe, and ecological. This method can also be valid to synthesize the other inverted core/shell semiconductor QDs.

The absorption spectra of 2-mercaptoethanol capped ZnS core and ZC1, ZC2, ZC3 (shell thickness is of the order ZC1>ZC2>ZC3) is being presented in (figure 4.1(b)). The absorption edge of core/shell QDs shift toward the red region in comparison to ZnS QDs as the QDs size increases due to reduced cappent ratio. The corresponding band gaps for all the core/shell QDs are being shown in (figure 4.1(c)) and were calculated to be 2.58 eV, 2.60 eV and 2.63 eV for ZC1, ZC2 and ZC3 respectively. This blue shift in absorption onset of ZC1 to ZC3 is a clear indication of the quantum confinement effect, also blue shift in absorption onset of ZnS shows quantum confinement compared with onset of the bulk ZnS material [2]. In ZC3 absorption spectrum shows two solders that assumed to originate from the radiative recombination of carrier at surface trap states resulted from the compounded effect of CdS at ZnS/CdS interface. With increasing thickness of the shell material, all the coherency stress will be relieved which leads to trapped charge carriers, so the thickness of the shell layer is critical for the optical response. After inverted core/shell we demonstrate the optical absorbance spectra of CdS, ZnS, ZnS/CdS and ZnS/CdS/ZnS multishell QDs (figure 4.2). Bulk form of ZnS shows absorption edge at 340 nm (E_g = 3.6 eV).

After formation of ZnS/CdS shell, absorption peak had a red shift from ZnS to ZnS/CdS with a band gap 4.1 eV and 2.9 eV respectively. Similar observations of red shift due to shell growth have also been observed in other ZnS/CdS/ZnS1, ZnS/CdS/ZnS2 systems [89, 92]. On the formation of CdS shell on ZnS, the absorption peak has a red shift and indicates an increase in the effective volume of the exciton. As the shell thickness is further increased, we observe a gradual restoration of the sharp absorption peak (in ZnS/CdS/ZnS2, ZnS/CdS/ZnS1) is being

observed. It indicates that transition in only shell to shell localization characterized by the increased e^--h^+ overlap [204, 7]. Small shell thickness shows smaller shift and higher shell thickness shows larger shift in figure 4.2. There may be many reasons for this shift. Among them some prominent reason is increment in the effective volume of exciton; as the electronic levels come closer that accompanies an increment in the size and increases the leakage of the exciton into the shell [17, 6].

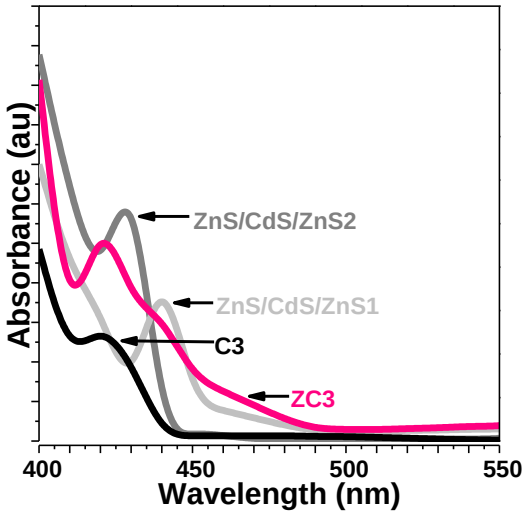

Figure 4.2: Absorption spectra of CdS, ZnS/CdS, ZnS/CdS/ZnS1 and ZnS/CdS/ZnS2.

4.2.1.2 ZnS/CdS/ZnS multishell QDs

Consequence of size and shell thickness has been investigated in this work. To identify the change in luminescence behavior, the core that is ZnS/CdS core/shell and ZnS/CdS/ZnS multishell structures have been studied and discussed on the basis of the model presented in (figure 4.3). It is easy to understand from the figure that how the luminescence is changing as the ZnS shell thickness varies. The experimental findings also resemble with the model presented here. The emission spectra of CdS, ZnS/CdS and ZnS/CdS/ZnS multishell QDs with different thicknesses of ZnS shell are presented in (figure 4.4).

A broad emission band for CdS with maximum at 546 nm is observed. Also a blue shift as observed compared to bulk CdS shifted to blue in comparison with the bulk CdS. The emission band at 430 nm corresponds to ZnS/CdS core/shell QDs. This can also be noted that the

luminescence intensity increased and shift to blue region side with respect to CdS (PL emission for ZnS around 320 nm with the lower intensity).

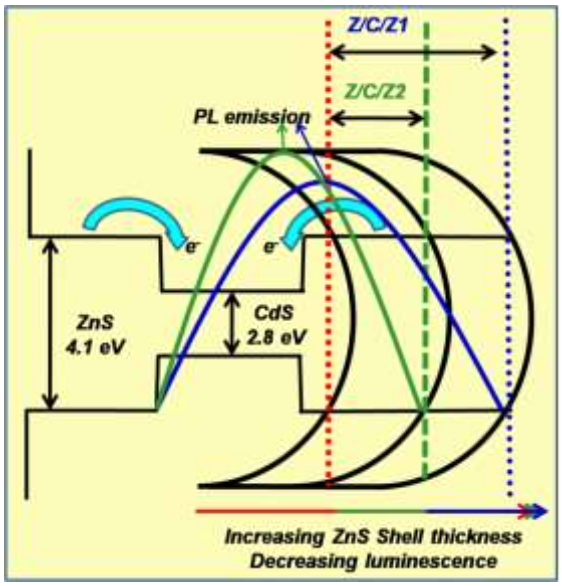

Figure 4.3: Schematic of ZnS/CdS/ZnS multishell QD structures with different ZnS shell thickness and corresponding PL behavior.

Because of the CdS shell formation on ZnS core the emission shifts to red region side as the shell formation increased the size of QD to some extent. Further in ZnS/CdS/ZnS there is an increment in luminescence intensity with an efficient tunability. This is because the wave functions of electron and hole in ZnS/CdS/ZnS1 are delocalized and in ZnS/CdS/ZnS2 the wave function of electron mostly localized in shell but hole's wave function localized preferably in core. Localization of electron-hole in the system can lead to the superior PL enhancement and fine tunability [211].

PL emission intensity was low when the thickness of ZnS shell was high where 1 ml capping agent has been used. On increasing the cappent to 2 ml, shell thickness decreased and PL emission intensity was increased, which is clearly illustrated from the emission of ZnS/CdS/ZnS2 [25]. The thinnest achievable shell of ZnS possesses the largest band gap and therefore, produces the maximum confinement potential for excited charge carriers. Conversely the conduction and valence bands move towards their bulk energies, resulting in the decrease in the effective energy barrier. In other way if the shell thickness increases it can physically extend

the tunneling length necessary for electron and hole interaction with the external medium which confines the photo-generated carriers inside the photo-luminescent core.

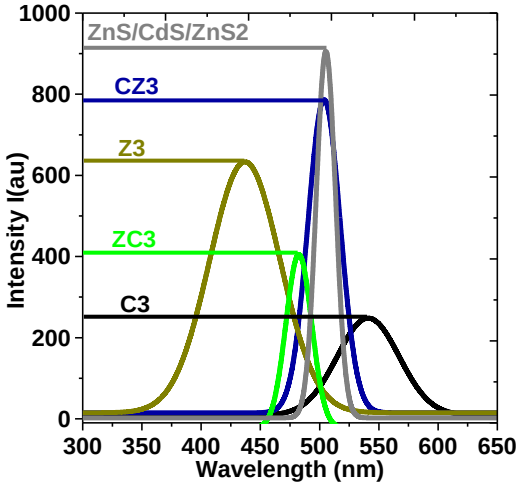

Figure 4.4: Photoluminescence spectra of CdS, ZnS/CdS, ZnS/CdS/ZnS1 and ZnS/CdS/ZnS2.

CdS creates a smaller interfacial strain, but its potential barriers are weaker compared to ZnS. Therefore, an approach combining the benefit of both the high potential barrier of ZnS and lattice compatibility of CdS is being proposed in this work [263]. The emission corresponds to the bulk donor–acceptor recombination of CdS. Surface states usually act as radiationless recombination centers. The ZnS shell compensates for most of the vacancies on the surface of the CdS well and the nonradiative recombination sites are passivated. These are responsible for the luminescence enhancement. The lattice parameters of CdS differ from that of ZnS by 7%. About one unitcell thick coating layers can accommodate the lattice misfit between CdS and ZnS by elastic strain exclusively [27]. If the shell thickness is more than the several order of one-unit cell, it can increase the strain due to the lattice mismatch resulting to direct formation of dislocations. Some reduction in the luminescent intensity is ascribed to the creation of misfit dislocations, which act as centers for radiationless recombination when the thickness of the shell increases [27].

4.2.2 Structural and morphological studies

In case of CdS and ZnS QDs the selection of precursors and synthesis parameters especially temperature plays an important role as it affects the crystal structure. It has been reported that the precursors $CdCl_2$ and Cd $(NO_3)_2$ give a mixture of cubic as well as wurtzite phases [8] and

references therein]. XRD patterns were recorded for CdS, ZC1, ZC2, ZC3 and ZnS samples to check the crystalline phase. It has been found that all ZnS/CdS QDs could be indexed to crystalline hexagonal phase of CdS in agreement with the respective JCPDS -1049 (figure 4.6). It is worth mentioning because hexagonal structure is known to be most stable phase [9]. The 2θ positions, (hkl) planes, phase assignments corresponds to CdS, ZC1, ZC2, ZC3 and ZnS QDs have been presented in table 4.1.

Table 4.1: Structural parameters such as 2θ positions**,** d-values, FWHM and intensity, hkl planes, phase assignment, particle size and lattice constant for all QDs.

Sam.	2θ (deg)	d (Å)		FWHM (deg)	Int	(hkl)	Phase assign	D (nm)	Lattice constant (Å)
		Obs.	Std.						
ZnS (Core)	28.68	3.10	3.12	1.34	80	(00,10)	Hexa	3.27	a = 5.4 c = 31.4
	32.22	2.55	2.66	2.55	25	(107)	Hexa		a =3.7 c = 30.7
	58.05	1.56	1.57	1.54	42	(206)	Hexa		a =5.4 c = 31.2
ZC1	29.08	3.06	3.16	2.32	100	(101)	Hexa	5.2	a = 4.0 C= 6.7
	33.11	2.88	2.90	1.72	40	(200)	Cubic		a = 3.8
	51.50	1.72	1.75	1.60	55	(112)	Hexa		a = 4.0 C= 6.5
ZC2	29.15	3.06	3.16	2.44	100	(101)	Hexa	4.8	a = 4.2 C= 6.7
	33.18	2.32	2.90	1.82	40	(200)	Cubic		a = 3.8
	51.62	1.71	1.75	1.65	55	(112)	Hexa		a = 4.1 C= 6.7
ZC3	29.23	3.06	3.16	2.52	100	(101)	Hexa	4.5	a = 4.0 C= 6.7
	31.22	2.69	2.90	1.87	40	(200)	Cubic		a = 3.8
	51.71	1.45	1.75	1.71	55	(112)	Hexa		a = 4.1 C= 6.7
CdS QDs (for ref.)	29.00	3.07	3.16	2.64	100	(101)	Hexa	-	a = 4.0 C= 6.7
	33.00	2.64	2.90	1.95	40	(200)	Cubic		a = 3.8
	51.46	1.77	1.75	1.87	55	(112)	Hexa		a = 4.0 C= 6.5

Calculated particle size using Scherer's formula and lattice constants values from XRD data have also been tabulated in table 4.1. The particle sizes for ZnS and ZC1, ZC2, ZC3 are 3.27 nm, 5.2 nm, 4.8 nm and 4.5 nm respectively. The particle sizes of core/shell QDs have been inspected by TEM to validate the effectiveness of cappent and the synthesis method; corresponding results are being presented in figure 4.5 for the Smallest QDs (ZC3) with XRD

spectrum. Particle size estimated by TEM is 5.5 nm, 5.2 nm and 4.6 nm for ZC1, ZC2 and ZC3 respectively that is slightly higher than the particle size obtained from XRD analysis [19]. We have further processed the TEM image to distinguish core (darker area) and shell (bright ring) precincts more visibly. This is the evidence of the occurrence of two different materials inside (ZnS core) and outside (CdS shell) in a single QD.

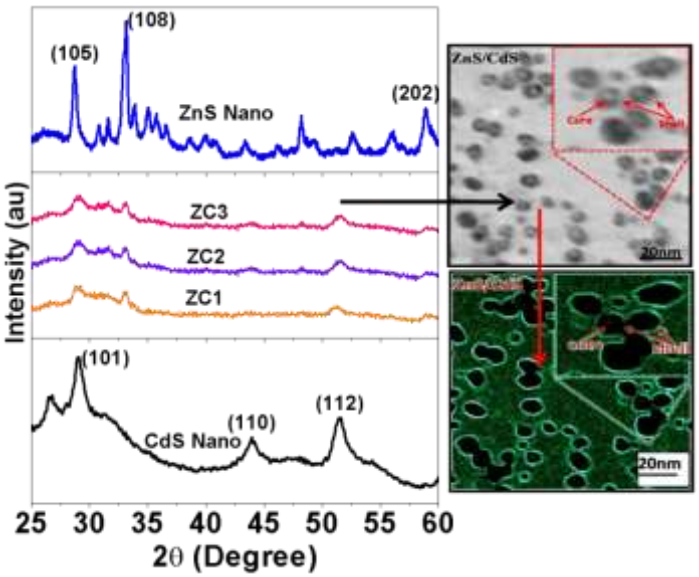

Figure 4.5: XRD spectra of CdS, ZnS, ZC1, ZC2, ZC3 QDs; and TEM image of ZnS/CdS (ZC3) QDs before and after processing.

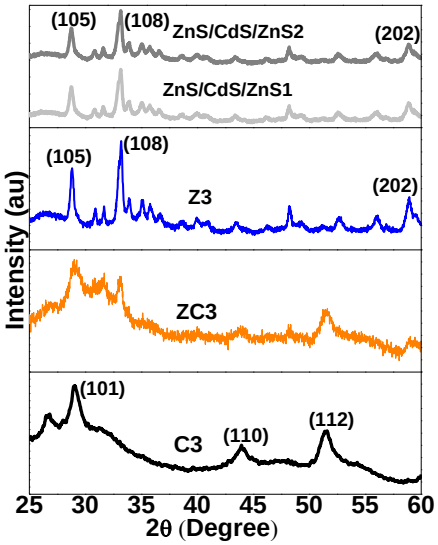

Figure 4.6: X-ray diffraction patterns of 2-mercaptoethanol capped CdS, ZnS, ZnS/CdS, ZnS, ZnS/CdS/ZnS1 and ZnS/CdS/ZnS2 QDs.

The selection of precursors and temperature plays an important role as it affects the crystal structure in case of CdS and ZnS QDs and ultimately helps to obtained desired wurtzite structures of QDs and multishell QDs [27]. X-ray diffraction (XRD) spectra of 2-mercaptoethanol capped CdS, ZnS/CdS, ZnS, and ZnS/CdS/ZnS QDs have been shown in (figure 4.6). Spectra of prepared QDs is in good agreement with JCPDS41-1049 for CdS and JCPDS 12-0688 for ZnS QDs. The prominent peaks (101), (110), (200) and (112) were indexed to the cubic/wurtzite structure in case of CdS and their core/shell structures. The prominent peaks in ZnS and their core QDs are indexed to (105), (108), (200) and (202) for wurtzite structure. In case of ZnS/CdS and ZnS/CdS/ZnS same peaks are prominent with Small shift in 2θ position which is again a clear indication for core/shell QDs. The crystallite size of all quantum dots (D) has been calculated by the three most prominent peaks by Scherer's formula. [262]. The calculated crystallite size from Scherer's formula is 2.3 nm, 3.1 nm, 3.5 nm, 4.3 nm and 3.9 nm for ZnS, CdS, ZnS/CdS, ZnS/CdS/ZnS1 and ZnS/CdS/ZnS2 respectively. As it can be seen (figure 4.6) in ZnS/CdS/ZnS1 the diffraction peaks of CdS and ZnS overlap each other and have intense peak. Whereas in case of ZnS/CdS/ZnS2 peak intensities decreased because ZnS shell put constraints on ZnS/CdS core. As the shell thickness reduced or the size of shell reduced, the core closed inside ZnS shell experience more compressive strain, due to this the intensity of peaks obtained in ZnS/CdS/ZnS2 get reduced.

4.2.3 Transmission electron microscopy

The particle sizes of QDs, core/shell QDs and multishell QDs have been determined by TEM to make sure the efficiency of cappent and the method of preparation. TEM images of the ZnS (figure 4.7(a)) and CdS (figure 4.7(b)) QDs show highly mono-dispersed nanoparticles with average sizes of 2.5 nm and 3.3 nm respectively. Figure 4.7 (c) indicates the micrograph for ZnS/CdS core/shell QDs and still there is indication of the formation of mono-disperse QDs with 4.2 nm particle size. Similarly ZnS/CdS/ZnS2 multishell (figure 4.7(d)) is having particle sizes 4.6 nm. It is also clear from the figure that there is no agglomeration of QDs even after the formation of multishell. It also indicates the capability to obtain either the fine solution or even powder of uniformly distributed nanoparticles for various applications. Clear formation of wurtzite ZnS/CdS QDs is depicted from (figure 4.5(TEM image to distinguish core and shell boundaries more visibly)) where light colored core (CdS) has been surrounded by the dark

colored shell (ZnS), conversely (figure 4.5(d)) shows the clear formation of wurtzite ZnS/CdS/ZnS2 multishell QDs. In this case one can observe the different shades on a single multishell which may be due to the presence of three different layers in a system and that is why difficult to differentiate between shells, well and shell. This result of wurtzite structure formation also supports our findings from XRD results. The particle sizes obtained from TEM are slightly greater than the size obtained from XRD analysis. The size obtained by XRD and TEM has the correlation that the XRD size is usually equals or smaller than the size obtained by TEM [251]. When the particles are delineated by well-defined boundary or loose nanoparticles of materials, XRD and TEM values are in good agreement. There is no big disparity in the particle sizes obtained from different techniques. Also it is clearly vindicated from the micrographs that the as prepared nanoparticles are of great quality (monodisperse, low agglomerations and have appropriate optical properties).

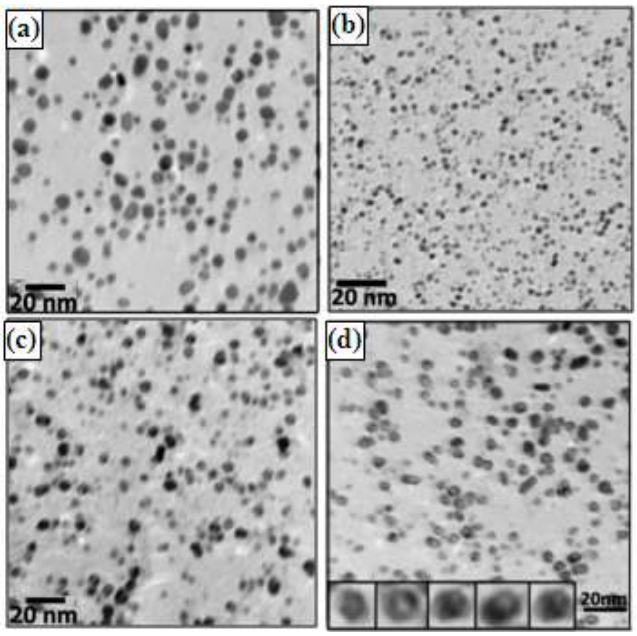

Figure 4.7: TEM micrographs (a) ZnS QDs; (b) CdS QDs; (d) ZnS/CdS core/shell QDs and (d) for ZnS/CdS/ZnS2 with smallest shell thickness.

4.2.4 Fourier transforms infrared spectroscopy studies

Prepared QDs were examined by FTIR in the range 4500–400 cm^{-1} (figure 4.8). The broad peak at 2120, 1383 cm^{-1} and the weak peak at 1614 cm^{-1} were assigned to C=C, C-H. The sharp peak

at 3365 cm^{-1} corresponds to (O-H) alcohols and 1119 cm^{-1} show (C-N) amines along with two Small peaks at 1626 cm^{-1} for (N-H) amines and 1401 cm^{-1} for O-H means carboxylic acid.

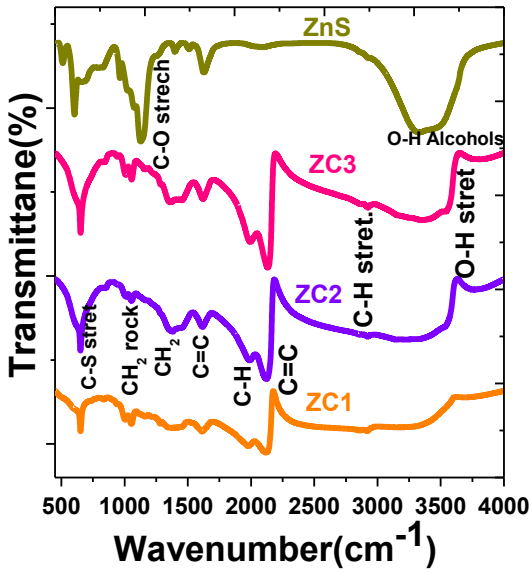

Figure 4.8: FTIR spectra of CdS, ZC1, ZC2 and ZC3 QDs.

Generally OH (Hydroxyl), COOH (carboxylic acid) or amine functionalities are present on the bio molecule surfaces and similar functional groups are present in prepared QDs [59, 264] and hence the prepared samples can be easily attached with bio molecules. Best remark of the studies is that as we have opted for aqueous medium to prepare QDs; there are always hydrophilic surfaces of QDs which are directly conjugatable to bio molecules. This is an additional benefit of our technique as because the QDs prepared by high temperature organic synthesis routes are always acquiring hydrophobic surfaces and there is need to further surface processing steps before bio-conjugation. Synthesized QDs are water soluble and biocompatible due to the use of 2-mercaptoethanol where the mercapto group has been used to bind Cd ions on the surface of CdS QDs. Also the carboxylic group of mercapto on the outer surface of QDs makes them biocompatible. As CdS present at the surface therefore there is possibility of leaching of Cd in to the surrounding medium. To protect QDs from Cd leaching encasing of QDs either with silica or other biocompatible polymers can be advantageous; but we are trying to control the leaching through binding of core-shell using biocompatible thiols group as capping agent [265].

4.3 CONCLUSIONS

A possible and distinctive growth mechanism for the formation of type-I "inverted hexagonal ZnS/CdS" quantum dots using wet chemical method at low temperature was proposed and accomplished. Red shift was observed in the ZnS/CdS QDs compared with that of the ZnS QDs. The PL spectra indicate a band edge emission with immense tuning. Structural analysis indicate that the ZnS/CdS were possessing hexagonal structure and hence highly stable. TEM indicated that the QDs were of 4.6 nm-5.5 nm size average in diameter. The presence of 2-mercaptoethanol on the ZnS/CdS QDs was confirmed by FTIR spectroscopy. The projected mechanism disclosed the importance and role of 2-mercaptoethanol to obtain stable inverted hexagonal ZnS/CdS QDs. Beside highly luminescent ZnS/CdS/ZnS multishell QDS with narrow PL emission width were successfully synthesized by wet chemical method at 35±1^{o}C. Strong carrier confinement in luminescent core using appropriate ZnS outer shell layer has been obtained and the outcomes reflect from the luminescence studies. Furthermore, PL spectra show a strong emission in multishell QD centered at 505 nm. The strong emission at 505 nm is from the charge transfer of electrons from CdS electron to ZnS holes by excitation energy. These ZnS/CdS/ZnS are a promising optical material in the applications to various transparent green optoelectronic devices and in imaging for diagnostics in medical applications.

CHAPTER –V

SYNTHESIS AND CHARACTERIZATION OF PbSe, PbS QUANTUM DOTS AND THEIR PbSe/PbS CORE/SHELL QUANTUM DOT STRUCTURES

We have developed the quantum dots, that emits from visible (II-VI group QDs as discussed in chapter 3 and 4) to near infrared (IV-VI group) region of the spectrum. Wet chemical methods have been used to produce IV-VI group PbSe, PbS quantum dots and PbSe/PbS core/shell quantum dot nanostructures. The prepared quantum dots can be useful in biomedical field i.e. bioimaging especially deep tissue imaging and in the field of photovoltaic where there is possibility to harness the multiple exciton generation capability of these IV-VI group quantum dots. The whole phenomenon is based on the quantum confinement and already been discussed in the earlier chapters.

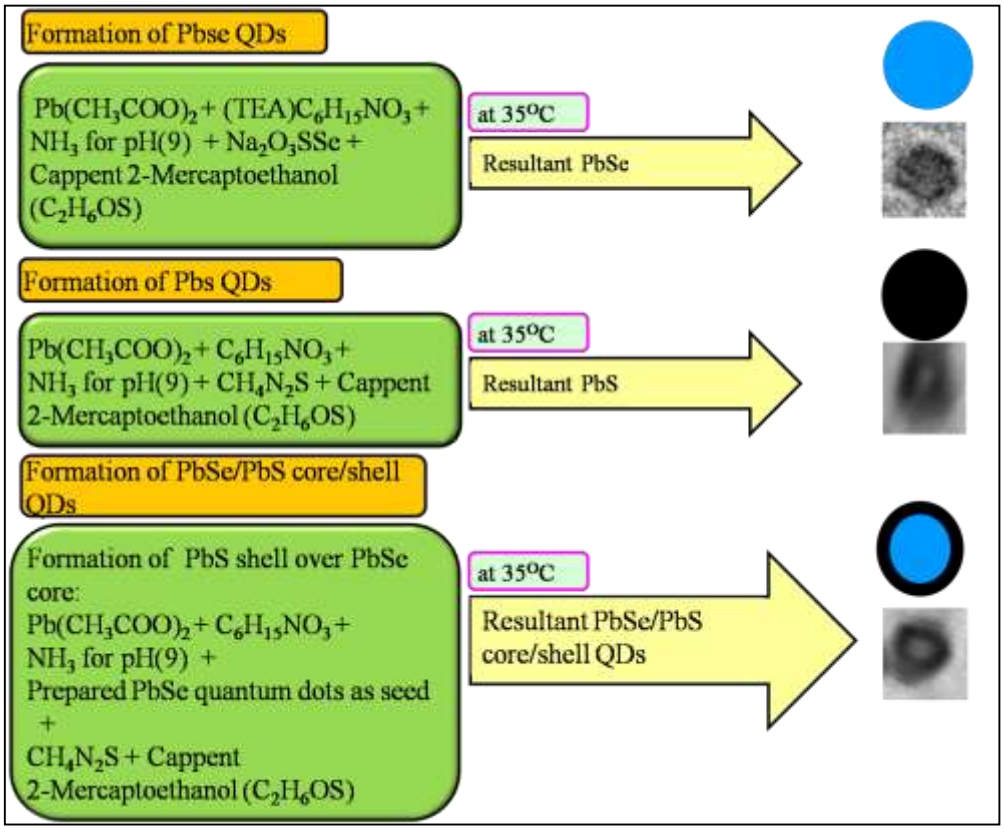

5.1 INTRODUCTION

Lead chalcogenide based semiconductor quantum dots (QDs) attract a great deal of interest due to their size dependent properties. The optical absorption and emission properties of these QDs can easily be adjusted due to quantum confinement. Most studies have focused on cadmium and zinc based quantum dots, the emissions and absorptions of which can be tuned all over the visible range of the electromagnetic spectrum [266-268]. Most researches are focusing on II-VI or III-V semiconductors compared to the other materials. On the other hand the materials belong to IV-VI semiconductors such as PbSe and PbS have larger Bohr exciton radius (46 nm for PbSe and 18 nm for PbS) and give emission in near infrared range. As a result, in PbSe or PbS quantum dots, it can be expected that such kind of materials has strong confinement effect, which is not possible in other materials. PbS and PbSe are narrow gap semiconductors with a bulk band gap in the range from 3000 - 4300 nm [269]. By scrutinizing crystallite size, tunable emission can be obtained in a large spectral region, ranging from the visible to the near infrared. This spectral range is of great interest for fabricating light sources (including lasers) or optical amplifiers. Broad emission in the near infrared and infrared is especially interesting for optical telecommunication devices. As an important branch of QDs materials, the near-infrared emitting (NIR) QDs with emission range of 700–1300 nm are becoming increasingly attractive in the last five years, because they can be used to noninvasive in vivo biomedical imaging (in this spectral region, the auto fluorescence and absorption from most flesh tissues are lowest) [270-272]. Among all nanocrystalline QDs, lead sulfide nanoparticles have some unique physical properties that fit various optical communication requirements and laser applications [273]. Varying PbS QD size allows tailoring the first absorption resonance in a wide spectral range from 3 down to 1 mm [274-275], with a specific intended absorption edge. For a specific particle size, the saturation intensity is entirely determined by the concentration of the nanocrystalline QDs per unit area, which may be controlled by sample thickness. This makes PbS QDs a good material for passive mode locking and high-speed photonic switch applications. Such quantum devices are being extensively studied as promising materials for specific photonic applications. A narrow bandgap of 0.41 eV, a large exciton Bohr radius (18 nm) and a strong quantum size effect in nanocrystalline form, PbS is widely used in many fields such as solar cells [276-281], infrared detectors [276, 282], infrared electroluminescent devices [283-284], and optical switches [285].

Furthermore, an efficient multiple exciton generation has been detected in PbS QD, thus rendering it a promising candidate for highly efficient photovoltaic devices [286, 287]

Recently, a liquid-phase synthesis method was reported that allows the growth of PbSe QDs in organic solution [288]. The procedure involves the reaction of lead oleate with trioctylphosphine selenide in diphenyl ether in the presence of an excess of oleic acid to control the growth of and protect the particles after the synthesis. The procedure was slightly modified by others, and optical properties of the NCs have been reported [289-300].The band gaps of the lead salts are small, but due to the very large Bohr radii of 18 nm for PbS and 46 nm for PbSe, [269]. The application of these PbSe QDs is currently under investigation, and electroluminescence and optical gain have been demonstrated. The PbSe QDs were also successfully doped in polymer waveguides. Using very similar synthesis procedures, it was also possible to synthesize oleate capped PbTe and PbS NCs [301]. Relatively little has been reported on the stability of these QDs in solution and in the solid state. The luminescence of these QDs can be very efficient when the surface of the QD is passivated with organic ligand. The luminescence efficiency of the PbSe QDs synthesized in this method is very high, between 10% and 90% when measured by comparison with an organic dye and 20% when measured directly with an integrating sphere.

The synthesis of core/shell QDs is usually applied to increase the luminescence stability, and for most of the II-VI semiconductor QDs methods to synthesize core/shell QDs have been reported. A shell of a large band gap semiconductor is grown over the original core in these type I core/shell structures, and the charge carriers (holes and electrons) that are generated in the QDs after photon absorption are confined to the core. Surface passivation by organic ligands is less critical in these structures. Recently, type II PbSe/PbS core/shells have been synthesized by Lifshitz et al. however, they did not provide detailed characterization of the photo stability. Efficient passivation of PbSe QDs is achieved by the epitaxial growth of a PbS shell onto PbSe QDs, leading to the formation of a core/shell structure [302]. Recently, high quality small sized PbSe/PbS core/shell QDs with band gap energy (E_g) of 1.3-1.0 eV was produced. PbS and PbSe have similar crystallographic and dielectric parameters and thus they form a perfect crystalline heterostructure. Hybrid passivated PbS and small sized PbSe/PbS QDs based solar cells show power conversion efficiency of 7 % [303] and 4 % [304] respectively.

There are many routes to prepare PbS QDs with different surfactants [305, 306] The most successful QDs used in solar cells and photo detectors are oleic acid capped PbS QDs or their post synthetic ligand exchange products [307, 308]. However, the 2.5 nm long oleic acid ligand inhibits charge transport among the nanocrystals. To improve charge transport, a post synthetic ligand exchange is used to replace the oleic acid with shorter ligand. Up to date, two successful routes for synthesis of highly photoluminescence (PL) PbS QDs have been developed, namely the organometallic method and water based synthesis [309-311].T he organ metallic method is a synthetic route in which trioctylphosphine (TOP) or trioctylphosphine oxide (TOPO) was used as stabilizing reagents. For example, Hines and Scholes reported Corresponding author. A variety of methods can be used for the formation of selenides, such as chemical bath deposition thermal decomposition of metal alkoxide, self-propagating high- temperature synthesis, sonochemical method, electrochemical method and sonoelectrochemical method. In this chapter we will address some structural, optical properties of 2-mercaptoethanol capped PbS, PbSe and PbSe/PbS core/shell QDs structures. Efficient passivation of PbSe by PbS QDs is achieved by the epitaxial growth of a PbS shell onto PbSe QDs, leading to the formation of a core/shell structure. There are many routes to prepare these QDs with different capping agent ratio [242].

5.2. EXPERIMENTAL

Synthesis and characterization used for 2-mercaptoethanol capped wurtzite PbSe, PbS and PbSe/PbS quantum dots

PbSe QDs were synthesized by solution growth method at 35±1^{o}C and 2-Mercaptoethanol has been used as capping agent. Same procedure of synthesis has also been followed for the synthesis of PbS and PbSe/PbS core/shell QDs which is fully explained with all reaction equations in second chapter (section 2.7). The prepared QDs were characterized by different characterization techniques. The structural investigation has been performed by XRD and the patterns were recorded in a Shimadzu powder x-ray diffractometer using Cu Kα1 radiation. The optical properties were studied by PerkinElmer Lambda2 UV–Vis spectrophotometer and absorbance spectra were recorded. Photoluminescence (PL) emission spectra of the samples were recorded by a computer controlled rationing luminescence spectrophotometer LS55 (Perkin-Elmer Instruments, UK) with accuracy= ±1.0 nm and λ reproducibility= ±0.5 nm. A 20 kW pulse <10 μs from a Xenon discharge lamp was used as the excitation source for recording

photoluminescence emission spectra. A gated photo multiplier tube was used as a detector. Prior to the PL experiments signal-to noise ratio was adjusted to 500:1, using the Raman band of water with excitation at 220 nm. The surface chemistry of the QDs has been studied using FTIR (Perkin-Elmer RX). Transmission electron microscopy (Hitachi H-7500) has been performed as the finest proof for the particle size and particle size distribution.

5.3 RESULTS AND DISCUSSIONS

The group IV-VI compounds formed by the elements of group IV and VI of the periodic table possess both zinc blende (cubic) as well as hexagonal (wurtzite) structure. The structure shown in figure 5.1 has cubic close packed arrays one of sulphur atoms and the other of lead atoms translated with respect to one another by ¼ the body diagonal of the usual cubic cell along a threefold axis. Each atom has 4 first neighbors of the other kind at the corners of a regular tetrahedron and 12 second neighbors of the same kind. Six of the second neighbors are in the same plane as the original atom at the corners of a regular hexagon; the remaining six are distributed three above and three below at the corners of a trigonal antiprism.

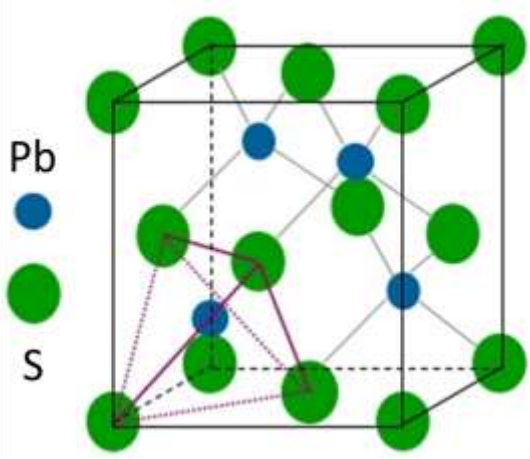

Figure 5.1: The zinc-blende crystal structure of PbS showing cubic symmetry. The grey and green spheres represent lead & sulphur atoms respectively.

A unit cell of PbSe zinc blende crystal is shown in figure 5.2. The grey spheres in the diagram denote Se atom and green spheres denote Pb atoms. Cubic PbSe structure results when Pb atoms are placed on one fcc lattice and Se. The atoms on the other fcc lattice as shown in figure 5.2. The conventional unit cell is a cube. This structure is almost identical to the diamond

structure except that the two interpenetrating fcc sublattices are of different atoms and are displaced from each other by ¼ of the body diagonal. Hence the general position of the atom is a/4, a/4, a/4 parallel to the central axial mirror plane i.e. glide plane.

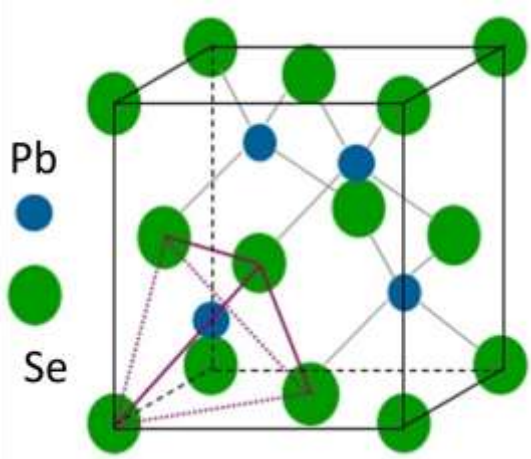

Figure 5.2: The zinc-blende crystal structure of PbSe showing cubic symmetry. The grey and green spheres represent lead & selenium atoms respectively**.**

5.3.1 Energy-dispersive X-ray analysis spectroscopy (EDXAS)

The quantitative and qualitative characterization of the PbS and PbSe QDs by energy dispersive X-ray (EDX) spectroscopy is shown in figure 5.3. Peaks of EDX spectra (figure 5.3) associated with Pb and S were clearly detected and provided strong evidence of the PbS formation, including the atomic ratio of Pb:S of 1:1.

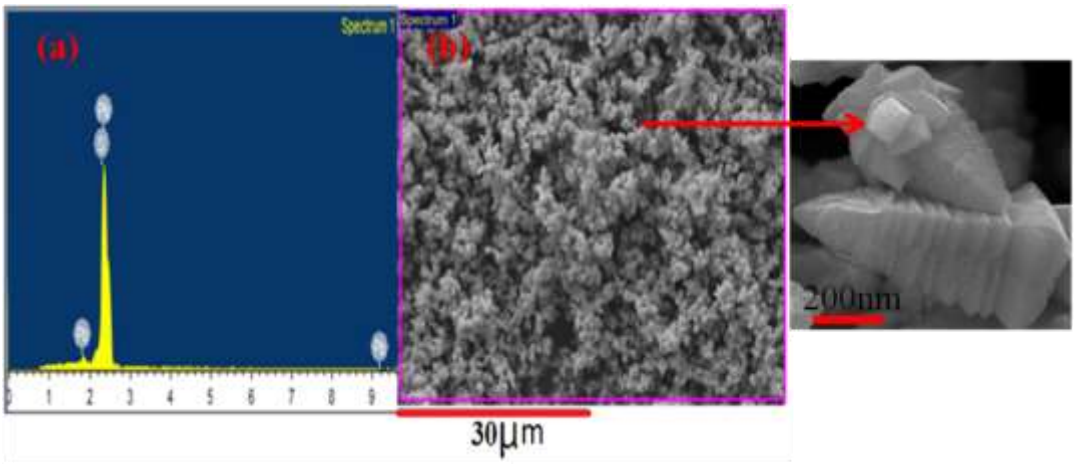

Figure 5.3: (a) EDX image of PbS and (b) FESEM image of prepared PbS with enlarged image.

The composition (in weight percentage) of the PbSe quantum dots were identified by EDX. Figure 5.4 shows the EDX spectrum of the PbSe quantum dots. As shown in the figure, as-prepared PbSe quantum dots only contain Pb and Se. The presence of Pb and Se demonstrate the existence of PbSe in atomic ratio of Pb:Se of 1:1. The value Pb, S and Pb, Se in prepared samples is tabulated below in table 5.1 and 5.2 respectively.

Table 5.1: Composition of PbS.

Elements	Weight%	Atomic%
S K	12.65	48.33
Pb M	87.35	51.67
Totals	100.00	

Table 5.2: Composition of PbSe.

Elements	Weight%	Atomic%
Se L	7.62	17.79
Pb M	92.38	82.21
Totals	100.00	

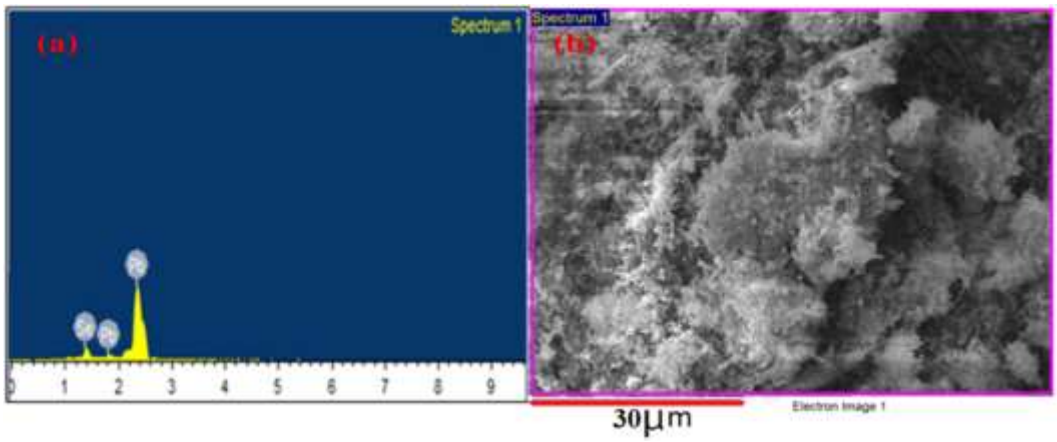

Figure 5.4: (a) EDX image of PbSe and (b) FESEM image of prepared PbSe with enlarged image.

5.3.2 Structural analysis

X-ray diffraction spectra of bulk PbS, bulk PbSe and 2-mercaptoethanol capped PbS (PbS1, PbS2, PbS3), PbSe (PbSe1, PbSe2, PbSe3) and core/shell PbSe/PbS (PbSe/PbS1, PbSe/PbS2, PbSe/PbS3) QDs have been shown in figure 5.5 (a, b and c). All the QDs were synthesized and capped by varying concentration of 2-mercaptoethanol (1 ml, 2 ml and 4 ml) for samples 1, 2 and 3 in each set respectively.

The XRD pattern of bulk PbS and 2-mercaptoethanol capped (PbS1, PbS2, PbS3) are shown in figure 5.5(a). The XRD pattern of lead sulphide nanoparticles have fundamental peaks

due to diffraction of lead sulphide on the plane (111), (200), (220), (311) and (222) which is in good agreement with the reported value [18].

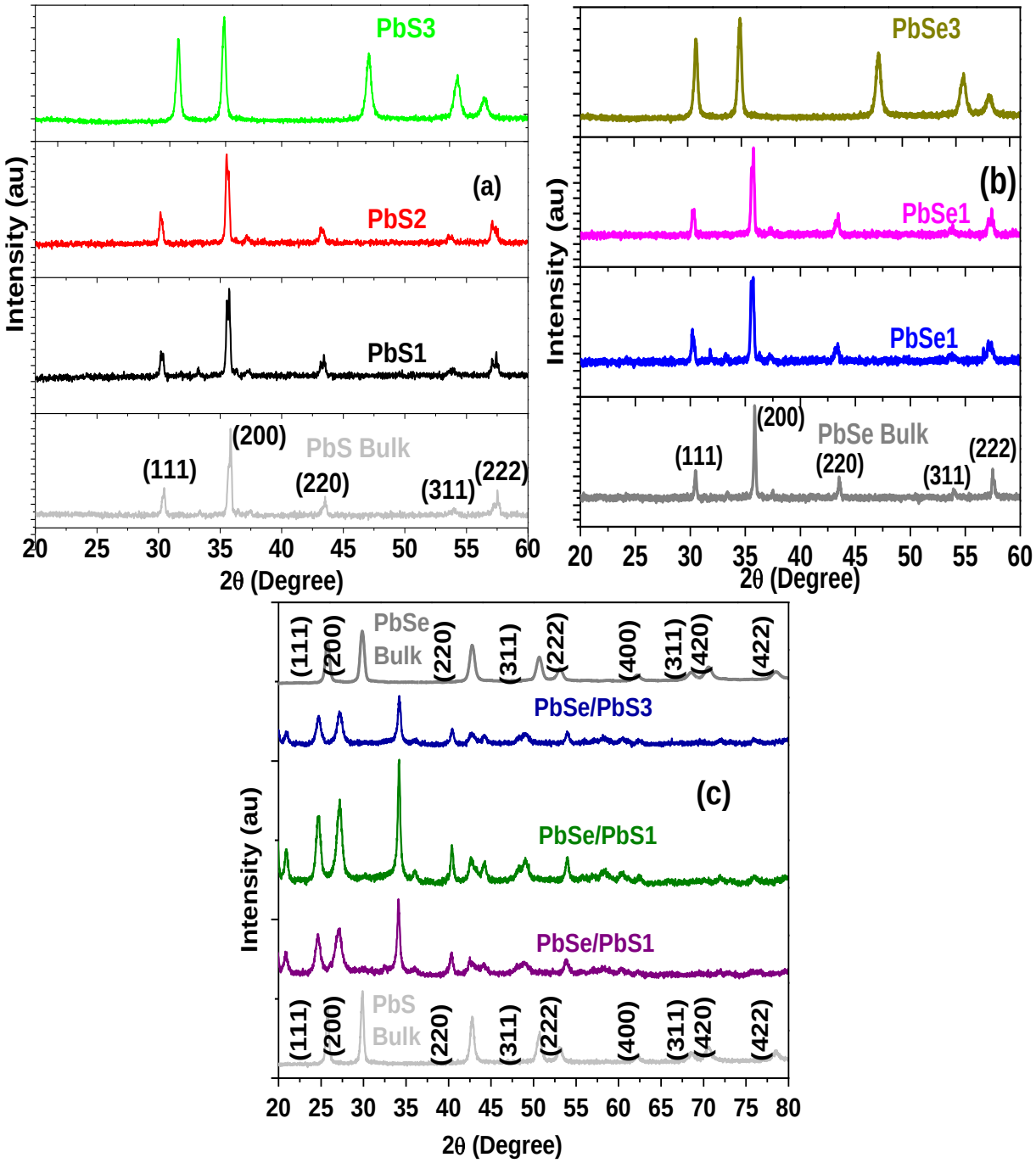

Figure 5.5: XRD pattern of (a) bulk PbS, and 2-mercaptoethanol capped PbS (PbS1, PbS2, PbS3) (b) bulk PbSe and 2-mercaptoethanol capped PbSe (PbSe1, PbSe2, PbSe3), (c) core/shell PbSe/PbS (PbSe/PbS1, PbSe/PbS2, PbSe/PbS3) QDs.

The successive broadening in XRD peaks show that the particle size substantially reduces with increasing concentration of the cappent. It shows that the cappent appropriately cap PbS QDs which arrest and stabilized the size. The crystallite size (*D*) of the QDs has been calculated using Scherer's formula. The average crystallite size obtained for PbS QDs is 6.5nm, which was obtained from the width of the (200) peak. The most prominent peaks in PbSe QDs (figure 5.5 (b)) were (1 1 1), (2 0 0), (2 2 0), (3 1 1) and (2 2 2) (h k l) planes. All the diffraction peaks can be readily indexed as the cubic structure PbSe, which agree with the literature datum (PDF No.65-2941). The strong and sharp reflection peaks suggest that the products are highly crystalline. Also, these patterns confirm that PbSe crystallites could be formed with high purity. The broadening of the peaks for PbSe QDs indicates small size of the synthesized materials. No additional peaks due to any impurity phase could be detected in the samples as vindicated from XRD spectra. Figure 5.5 (c) shows the XRD spectra of core/shell PbSe/PbS (PbSe/PbS1, PbSe/PbS2, PbSe/PbS3) QDs.

The diffraction peaks were broadened prominently, which is the characteristic of nanoparticles. XRD of core/shell structures clearly show that the prominent peak located at the centre of both PbS and PbSe spectra approximately. This is a clear indication of the formation of the corresponding core/shell structures. This shift in XRD patterns have been observed in many studies [307]. The full width at half maxima (FWHM), intensity, phase assignment and crystallite size as calculated have been tabulated in table 5.3. The lattice parameters `a' and 'c' of the unit cell have been calculated according to the relations explained in chapter 3 (section 3.3.1). Crystals have generally two types of strains, uniform and non uniform. We concluded that in our samples, there is non-uniform strain that leads to systematic shifts of atoms from their ideal positions leading to peak broadening. This type of strain arises from any of the following sources viz, point defects, vacancies, site-disorder and poor crystallanity. Hence an attempt has been made to estimate the average strain (ε_{str}) of the PbS and PbSe nanoparticles using Stokes-Wilson equation (chapter 3, section 3. 3. 1). It has been found that crystals with larger dislocation densities were harder and this hardness factor more important in shape of nanoparticles. The values of dislocation densities for all QDs have tabulated in table 5.4.

Table 5.3: FWHM, intensity, phase assignment, lattice constant and particle size of 2-Mercaptoethanol capped PbS, PbSe and PbSe/PbS QDs.

SAM	2θ (Deg)	d (Å)	FWHM (Deg)	I/I_o	Phase assignment	D (nm)	hkl	Lattice constant (Å)
PbS1	25.99	2.52	0.85	100	Cubic	**8.4**	111	5.6
	30.14	2.95	0.90	35	Cubic		200	5.9
	53.43	1.48	1.32	32	Cubic		220	5.1
PbS2	25.99	2.51	0.89	100	Cubic	**8.0**	111	5.5
	30.10	2.95	0.95	32	Cubic		200	5.9
	53.43	1.47	1.40	32	Cubic		220	5.08
PbS3	25.79	2.50	0.90	100	Cubic	**6.5**	111	5.6
	30.19	2.93	0.99	34	Cubic		200	5.9
	53.41	1.47	1.44	33	Cubic		220	5.4
PbSe1	25.97	2.51	0.76	100	Cubic	**9.0**	111	5.4
	30.11	2.95	0.85	33	Cubic		200	5.9
	53.39	1.47	1.23	27	Cubic		220	5.0
PbSe2	25.96	2.51	0.80	100	Cubic	**8.5**	111	5.6
	30.09	2.95	0.88	34	Cubic		200	5.9
	53.43	1.47	1.29	39	Cubic		220	5.0
PbSe3	25.99	2.50	0.83	100	Cubic	**8.0**	111	5.4
	30.15	1.60	0.90	34	Cubic		200	5.9
	53.40	1.47	1.84	33	Cubic		220	5.4
PbS/PbSe1	30.14	2.62	0.96	100	Cubic	**10.5**	111	5.4
	43.02	3.29	0.83	62	Cubic		200	5.9
	53.41	1.69		53	Cubic		222	5.8
PbS/PbSe2	30.10	2.62	0.99	100	Cubic	**9.7**	111	5.4
	43.10	3.28	0.90	62	Cubic		200	5.9
	53.47	1.69	0.77	53	Cubic		222	5.8
PbS/PbSe3	30.12	2.62	1.04	100	Cubic	**8.9**	111	5.2
	43.14	3.27	0.95	67	Cubic		200	5.4
	53.37	1.70	0.88	59	Cubic		222	5.8

Results clearly show that as the value of grain size decreases the value of dislocation density increases gradually. This is due to the additional lattice mismatch which implies lattice imperfection is more in small grains i.e. (6.5 nm). Dislocation density suggests that the prepared semiconductor QDs become less ordered and more hardened as a result, the strength of materials increases with decreasing grain size [2]. Specific surface area "SSA" is a property of solids which tells about the total surface area of a material per unit of mass solid and calculated by relations explained in chapter 3. It is used to derive scientific value that can be used to determine the type and properties of a material. The SSA is increased as the particle size becomes small. So it is important to measure the specific surface area to evaluate the activity and adsorption capacity of materials (e.g. catalysis and adsorbent). The large SSA of nanoparticles is the origin of a number of their unique applications. The specific surface area of the particles is the summation of the areas of the exposed surfaces of the particles per unit mass. There is an inverse relationship between particle size and surface area. If the particles are assumed to be as spherical and in a narrow size distribution, the specific surface area provides an average particle diameter in nanometer [2]. SSA values for all QDs have been tabulated in table 5.4.

Table 5.4: Particle size (nm), strain (ε_{str}), dislocation density (δ), specific surface area and surface to volume ratio of 2-Mercaptoethanol capped PbS, PbSe and PbSe/PbS QDs.

Samples	D (nm)	Strain ε_{str}	δ [nm]$^{-2}$	SSA (m^2/g)	Surface to volume ratio
PbS1	8.4	1.16	0.086	456	2.31
PbS2	8.0	1.28	0.118	489	2.45
PbS3	6.5	2.32	0.189	521	2.56
PbSe1	9.0	1.43	0.022	301	1.89
PbSe2	8.5	1.56	0.040	323	1.95
PbSe3	8.0	1.70	0.054	389	2.11
PbSe/PbS1	10.5	1.10	0.031	342	1.92
PbSe/PbS2	8.9	1.22	0.039	378	2.24
PbSe/PbS3	9.7	1.43	0.042	402	2.37

5.3.3 Transmission electron microscopy

The particle sizes of PbS3, PbSe3 and PbSe/PbS3 QDs have been determined by TEM to make sure the effectiveness of cappent and the results are presented in figure 5.6.TEM image (figure 5.6(a)) of the PbS QDs shows highly monodispersed nanoparticles with average sizes of 8.3 nm. Similarly PbSe QDs (figure 5.6(b)) with 10.2 nm and PbSe/PbS core/shell QDs (figure 5.6(c)) having 12.4 nm particle sizes. It is also clear from the figure that there is no agglomeration of QDs and we can obtain either the fine solution or even powder of uniformly distributed nanoparticles for various applications. There is no big disparity in the particle sizes obtained from different techniques. TEM images clearly shows that the as prepared nanoparticles have no agglomeration.

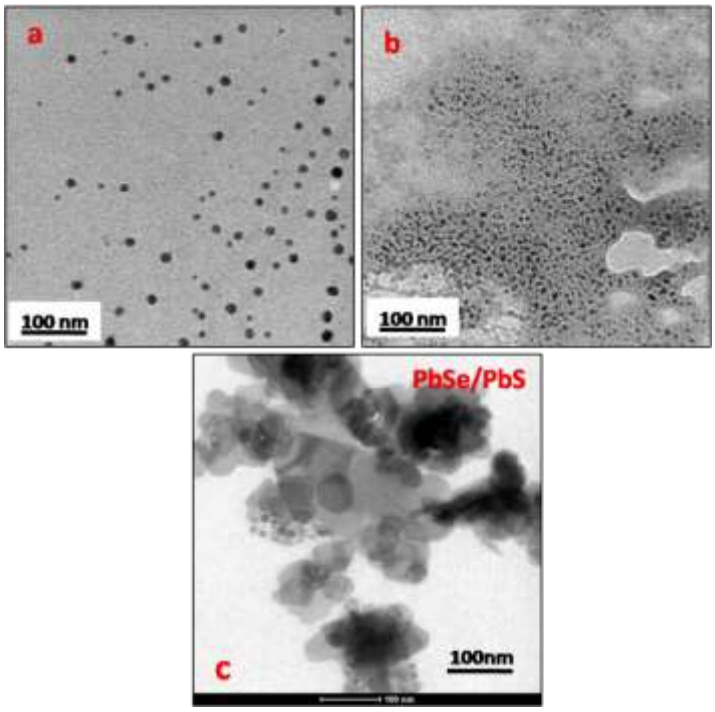

Figure 5.6: TEM images of capped (a) PbS3, (b) PbSe3 and (c) PbSe/PbS3 QDs.

5.3.4 Optical characterization

5.3.4.1 Optical absorption studies

PbSe/PbS is type I core/shell structure: Band gap of the shell (PbS) is larger than that of core (PbSe). The conduction and valance band offset are such that the conduction band of shell is

higher than that of core, while the valance band of the shell of lower energy than that of the core. This leads to an effective confinement of electron and hole in the core material. The exciton behavior mechanism on the core/shell system and the emission of the fluorescence is illustrated in figure 5.7. The optical band gap of 2-mercaptoethanol capped PbS (PbS1, PbS2, and PbS3), PbSe (PbSe1, PbSe2 and PbSe3) and core/shell PbSe/PbS (PbSe/PbS1, PbSe/PbS2, PbSe/PbS3) QDs have been determined from the absorption spectra. The UV–visible (UV–vis) absorption spectra of PbS, PbSe and PbSe/PbS QDs have been presented in figure 5.8. The absorption edge of the optical energy band gap of PbSe, PbS and PbSe/PbS QDs have been calculated using the equation 11 given in chapter 3.

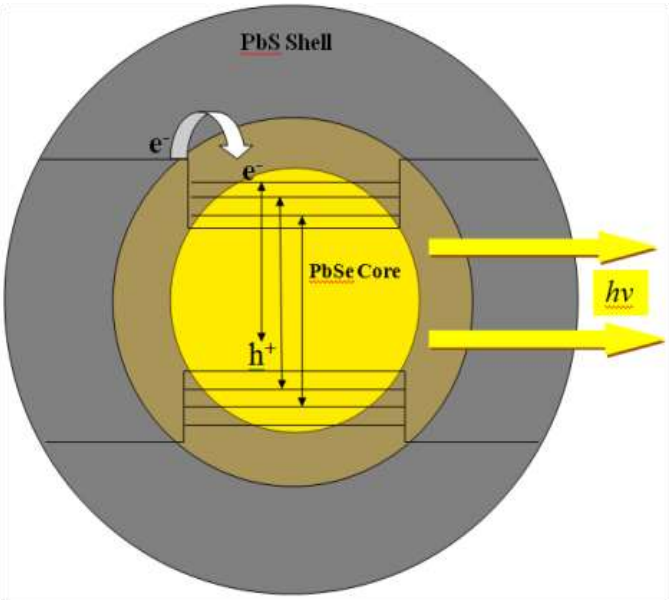

Figure 5.7: Schematic diagram of PbSe/Pbs Core/shell structure.

The optical absorption edge and the calculated band gaps have been shown in the table 5. Absorption edge for bulk PbS exists at 3000 nm and for PbSe at~ 5800 nm. The band gap energies gradually increase from 0.77 eV to 1.08 eV in case of PbS and from 0.70eV to 1.09eV in case of PbSe QDs. The estimated optical band gaps for PbSe/PbS core/shells were about 0.75 to 1.02 eV for low and high shell thicknesses respectively indicating the strong quantum confinement. The increase in band gap with increase in molar concentration of the capping agent is attributed to size quantization effect due to the small size of the particles [2]. Particle size and absorption edge with capping agent ratio tabulated in table 5.5 below.

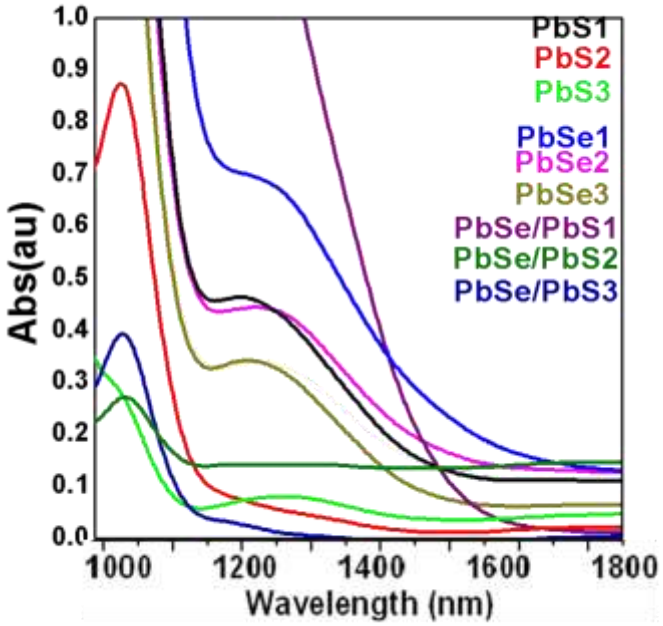

Figure 5.8: Absorption spectra of 2-mercaptoethanol capped PbS (PbS1, PbS2, PbS3), PbSe (PbSe1, PbSe2, PbSe3) and core/shell PbSe/PbS (PbSe/PbS1, PbSe/PbS2, PbSe/PbS3) QDs.

Table 5.5: Particle size, absorption edges, band gap and capping agent ratio for PbS, PbSe and PbSe/PbS QDs.

SAM.	Abs. Edge (nm)	E_g (eV)	Ratio of Capping Agent
PbS 1	1610	0.77	1 ml
PbS 2	1200	1.03	2 ml
PbS 3	1140	1.08	4 ml
PbSe1	1762	0.70	1 ml
PbSe2	1580	0.78	2 ml
PbSe3	1130	1.09	4 ml
PbS/PbSe1	1632	0.75	1 ml
PbS/PbSe2	1600	0.77	2 ml
PbS/PbSe3	1215	1.02	4 ml

On the other hand, various theoretical approaches have been employed to account for the variation in the electronic structure of nanocrystallites as a function of their size viz effective mass approximation (EMA), the tight-binding approximation (TBA) and hyperbolic band model (HBA). Particle sizes were estimated from the band gap values using Brus equation by effective mass approximation (EMA) by using equation no 13, 14 and 16 respectively. It has been found that only little number of reports is available on core/shell materials that have been analyzed by EMA, HBM and TBA theoretical models [2]. All calculated values using different models resemble very closely with experimental data but fitted more precisely with TBA model shown in figure 5.9.

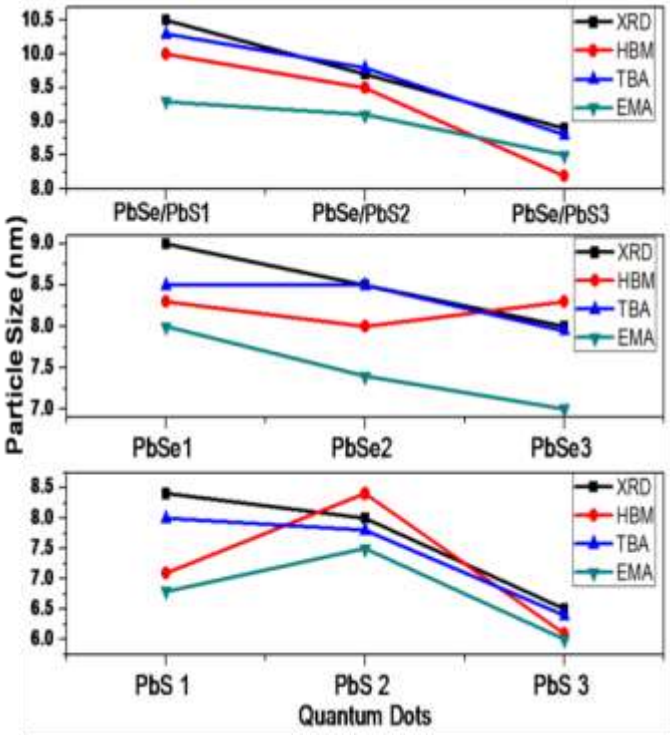

Figure 5.9: Best fitting of particle size calculated by XRD and theoretical models such as EMA, TBA and HBA.

5.3.4.2 Photoluminescence studies

The luminescence properties of 2-mercaptoetnanol capped PbS (PbS1, PbS2, PbS3), PbSe (PbSe1, PbSe2, PbSe3) and core/shell PbSe/PbS (PbSe/PbS1, PbSe/PbS2, PbSe/PbS3) QDs shown in figure 5.10. PL spectra were recorded at an excitation wavelength of 1000 nm. It is well known that surface defect states play important roles in the luminescence properties of nanoparticles, which act as radiative or nonradiative centers in nanoparticles [2]. The PL

spectrum of the PbS (1,2 and 3) QDs was dominated by very strong emission peak at around 1300 nm, 1320 nm and 1325 nm respectively but PbS (2 and 3) shows another peaks at 1580 due to sulfur defects in figure 5.10 (a). The fluorescence enhancement may be attributed to a much higher concentration of radiative recombination centers. The PL intensity of 2-mercaptoethanol capped particles is dramatically enhanced. The PL spectrum of the PbSe (1,2 and 3) QDs were shows strong emission peak at around 1280 nm, 1322 nm and 1325 nm respectively but PbSe (2 and 3) shows other peaks at 1600 nm due to surface defects shown in figure 5.10 (b).

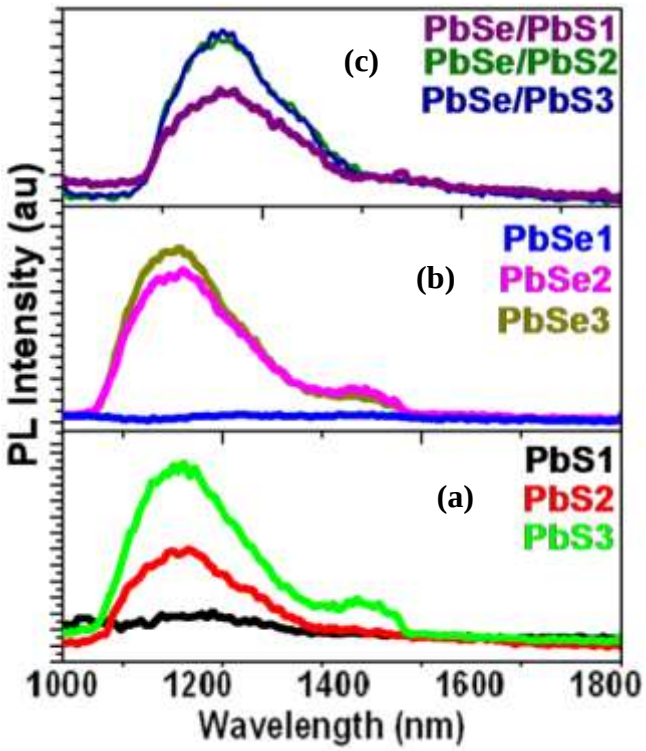

Figure 5.10: Photoluminescence spectra of 2-mercaptoethanol capped PbS (PbS1, PbS2, PbS3), PbSe (PbSe1, PbSe2, PbSe3) and PbSe/PbS (PbSe/PbS1, PbSe/PbS2, PbSe/PbS3) core/shell QDs.

The fluorescence enhancement may be attributed to a much higher concentration of radiative recombination centers. It is observed that the photoluminescence efficiency of capped PbSe QDs with higher concentration of 2-mercaptoethanol show high intensity due to passivation of surfaces [2]. Emission spectra for as prepared PbSe/PbS (1, 2 and 3) QDs have been recorded (figure 5.10 (c)). Interesting effect in PL spectra is the enhancement and single emission peak around 1460 nm for the PbSe/PbS (2 and 3) which can be associated with an

interband connection between the interface of PbSe core and PbS disordered shell. PbS confines the photo generated electron–hole pairs to the PbSe core interface modified by the quantum confinement effect, leading to the passivation of non-radiative transitions and enhancing the luminescence intensity. Structures and subsequently different materials properties, and this phenomenon can be related to local (short), intermediate and long-range structural order–disorder [2]. The peaks are also assumed to originate from the radiative recombination of carrier at surface trap states resulted from the compounded effect of PbSe at PbSe/PbS interface.

5.4 CONCLUSION

The PS, PbSe and PbSe/PbS QDs whose emission spans most of the NIR spectrum have been described which have been synthesized using wet chemical growth method. Their structural as well as optical properties have been investigated by XRD, UV-Vis spectroscopy, photo luminescence spectroscopy, and TEM. The PbS shell appears on PbSe QDs properly covered and creates dislocations or other defects to accommodate the mismatch in lattice constants between PbS and PbSe. The influence of surface passivation on the optical properties has also been evaluated. The UV-Visible-NIR spectra show a large blue shift attributing the enhanced optical properties, this size dependent blue shift in absorption edge is attributed to the quantum size effect. PL measurements show effectiveness of capping and core/shell structure formation as there is clear vindication of enhanced luminescence. Core/shell semiconductor QDs that were prepared by our method are low-cost, safe, and ubiquitous at least for II-VI and IV-VI group compounds.

CHAPTER – VI

SUMMARY

6.1 SUMMARY

Semiconductor quantum dots (QDs) have emerged as fascinating systems at the nanoscale with a wide range of applications extending from optoelectronic devices to biological detection. Recently, attention has also focused on the growth of organized array of quantum dots with the desire to develop ability to modulate the physical properties in two or three dimensions while exploiting the unique properties arising from quantum confinement effects. Typical application for such quantum dot systems may include photonic band gap devices, low power lasers, memories etc. Amongst the various techniques that have been employed for synthesis of low dimensional systems, wet chemical processes have emerged as the forerunner. Consequently research efforts are being avidly pursued to develop wet chemical nano-processes with the desire to generate more complex functional three-dimensional nanostructures. At these sizes, nano particles show fascinating behavior which has governed by quantum phenomenon. The individuality of the structural characteristics, energetic response, physics and chemistry of nano particles are indeed experimental and conceptual background for novel devices so these are the reasons for *small is beautiful……..*

Now a day's Nanotechnology will provide the ultimate convergence of computers, networks, and biotech, and create products never before even imagined. Nano-biology will prolong life, prevent illness, and increase people's health. Nanotechnology enhanced and will enhance superior physical, intellectual, and sensing powers to the humans. It will provide a cheap and available source of energy. Nano factories will build on-demand products in an inexpensive, flexible, and rapid process.

Quantum dots are very small particles of semiconductor materials ranges in a few nanometers and possess hundred to a few thousand atoms. When an electron is excited by a photon striking the quantum dot, it behaves as a particle confined in an infinite potential well, since the electron cannot escape from the quantum dot. The hole, created by the excited electron, behaves in the same fashion. The energy levels can be calculated using the "particle in a box model" in which the energy of different states is dependent on the length of the box. If the radius of the nanoparticles is equal to the exciton Bohr radius than there QDs are in the "weak confinement regime" while quantum dots are said to be in the "strong confinement regime" if

their radii are smaller than the exciton Bohr radius. If the size of the QDs is less than 10 nm then "quantum confinement effects" lead and electronic and optical properties become highly tunable.

Since quantum dots are only a few nanometers in diameter, they have a very high surface-to-volume ratio, approximately 80% of the atoms be located on the surface. Due to this high surface-to-volume ratio estimated that the properties of the surface have significant effects on the optical and structural properties of the particles. These very reactive surfaces induce the defects at the surface. Surface defects, just as dangling bonds, are surface-related trap states that act as non irradiative recombination sites which degrade the fluorescence quantum yield of quantum dots. Important motivation of utilizing core-shell nanostructure is to improve properties of core/shell QDs, such as luminescence efficiency. To better passivate the surface, a secondary semiconductor can be epitaxially grown surrounding the core particle. After coating the core with shell, the quantum yield has been shown to greatly increase up to ten times, as well as displaying increased stability against photo-oxidation and environmental attack. This is the motivation behind the core/ shell QDs.

Core/shell and inverted core/shell quantum dots (QDs) synthesized using wet chemical route are a class of materials which are actively being explored because of their amendable optical and electronic properties. In general in all types of core/shell QDs (e.g. CdS/ZnS), shell increases quantum yield by passivating the surface trap states. Specifically in inverted core/shell structures a core of a wide-gap semiconductor is over coated with a shell of a narrower gap material. The core and shell enable the emission wavelength to be tuned over a wider range of wavelengths than with either individual semiconductor. These "inverted" QDs provide capabilities for controlling functionalities by a direct control of the distribution of electron and hole wave functions and the electron-hole overlap integral. Consequently results in enhancement in the photoluminescence (PL) emission intensity due to localization of the electron-hole pair. Several different combinations of core/shell QDs such as CdSe/ZnS, CdS/ZnS, ZnO/ZnS, ZnSe/ZnS, CdSe/CdS, CdS/PbS, and ZnSe/CdS have previously been studied by different groups.

Particularly, scientists give more attention to QDs, core/shell QDs and multishell QDs because multishell QDs structures represent the special case of a multishell structure in which a

lower bandgap layer is embedded between a higher-bandgap core and outer shell material with both semiconductors having type-I band alignment. Among the first systems studied was CdS/HgS/CdS. These kinds of structures with unique properties can be prepared by a chemical or physical process, and some new and enhanced physical properties were found due to the core shell interface effects. Numerous investigations have focused on forming the multishell QDs by sandwiching the low band gap material in the well between the layers of quantum dots of higher band gap material viz. ZnS/PbS/ZnS CdS/HgS/CdS, ZnS/CdSe/ZnS. Very few authors (hardly one or two) have been reported the wurtzite ZnS/CdS/ZnS but methods were different or they were used physical synthesis method on high temperatures. Uniform shell coverage was observed only for graded shells (e.g., CdS/ZnS) and was found to be critical to achieving high luminescence.

Most researches are focusing in II-VI or III-V semiconductors compared to the other materials but IV-VI semiconductors such as PbSe and PbS have larger Bohr exciton radius (46 nm for PbSe and 18 nm for PbS). As a result, in PbSe or PbS quantum dots, it can be expected that such kind of materials has strong-confinement effect, which cannot occur in other materials. PbS and PbSe have narrow gap semiconductors with a bulk band gap in the range from 3000 - 4300 nm. The emission and absorption lines are therefore broader, but by virtue of its crystallite size, tunable emission can be obtained in a large spectral region, ranging from the visible to the near infrared. This spectral range is of great interest for fabricating light sources (including lasers) or optical amplifiers. Broad emission in the near infrared and infrared is especially interesting for optical telecommunication devices. As an important branch of QDs materials, the near-infrared emitting (NIR) QDs with emission range of 700–1300 nm are becoming increasingly attractive in the last five years, because they can be used to noninvasive in vivo biomedical imaging (in this spectral region, the auto fluorescence and absorption from most flesh tissues are lowest. A narrow bandgap of 0.41 eV, a large exciton Bohr radius (18 nm) and a strong quantum-size effect in nanocrystalline form, PbS is widely used in many fields such as solar cells, infrared detectors, infrared electroluminescent devices, and optical switches. Furthermore, an efficient multiple exciton generation has been detected in PbS QD, thus rendering it a promising candidate for highly efficient photovoltaic devices.

Nowadays (CdS, ZnS, PbS and PbSe) QDs and their core/shell QDs are very much important candidates for new applications. On the basis of the applications and demands these QDs has been opted for my research work. This thesis presents the results on the synthesis of CdS, ZnS QDs, CdS/ZnS core/shell QDs, ZnS/CdS inverted core/shell, ZnS/CdS/ZnS multishell QDs, PbSe, PbS QDs and their PbSe/PbS core/shell QDs by wet chemical methods.

First chapter presents an overview on quantum dots and size quantization effects is given to create a theoretical background behind the work presented in this thesis. Furthermore, an overview of various conventional techniques for size determination is presented. Second chapter of the thesis provides introduction of characterization techniques that we have used to identify the properties of quantum dots materials.

Third chapter described about wurtzite CdS, ZnS and CdS/ZnS QDs those have been synthesized using wet chemical growth method where consequence of size and shell thickness of QDs analyzed. Their structural as well as optical properties have been investigated by XRD, UV-Vis spectroscopy, photo luminescence spectroscopy, FTIR and TEM. XRD results indicated that lower synthesis temperature resulted in lower grain size and less strained particles. The UV-Visible spectra show a large blue shift attributing the enhanced optical properties, this size dependent blue shift in absorption edge is attributed to the quantum size effect. PL measurements show effectiveness of capping and core/shell structure formation as there is clear vindication of drastically enhanced luminescence. The ZnS shell grown on CdS QDs properly covers the ZnS QDs and creates dislocations or other defects to accommodate the mismatch in lattice constants between ZnS and CdS. The particle sizes of CdS, ZnS and CdS/ZnS QDs as determined from XRD and TEM images were in good agreement. Core/shell semiconductor QDs that were prepared by our method are safe and environmental friendly. Color tunable CdS, ZnS and CdS/ZnS QDs were created which are monodispersed possessing high stability and; narrow PL spectra that indicate superior monochromaticity. This method can also be applicable to synthesize the other tunable, monochromatic core/shell semiconductor QDs.

In forth chapter the low temperature wet chemical method was discussed that was used to prepare 2-mercaptoethenol capped inverted hexagonal ZnS/CdS QDs and high quality ZnS/CdS/ZnS multishell QDs were successfully synthesized by wet chemical method at 35±1^{o}C.

Red shift was observed in the ZnS/CdS QDs, compared with that of the ZnS QDs. The PL spectra indicate a band edge emission with immense tuning. Structural analysis indicate that the ZnS/CdS were possessing hexagonal structure and hence highly stable. TEM indicated that the QDs were of 2.5 nm - 5.2 nm average in diameter. The presence of 2-mercaptoethenol on the ZnS/CdS QDs was confirmed by FTIR spectroscopy. A proposed growth mechanism has been accomplished which disclosed the importance and role of 2-mercaptoethenol for stable inverted hexagonal ZnS/CdS QDs formation. ZnS/CdS/ZnS multishell QDs shows luminescence in the region of 430 nm to 550 nm was observed. The luminescence from CdS was enhanced by the complete ZnS shell, which may be the result of the decrease in the defects on the surface of the CdS well, which were assumed to act as centers for radiation less recombination. For these ZnS/CdS superlattices, the mismatch between their lattice parameters is only 3.0%. Furthermore, PL spectra show a strong emission centered at 505 nm. The strong emission at 505 nm is from the charge transfer of electrons from CdS electron to ZnS holes by excitation energy. These ZnS/CdS/ZnS are a promising optical material in the applications to various transparent green optoelectronic devices.

Synthesis and characterization of 2-mercaptoetnanol capped PbSe (PbSe1, PbSe2, and PbSe3), PbS (PbS1, PbS2, and PbS3), and core/shell PbSe/PbS (PbSe/PbS1, PbSe/PbS2, and PbSe/PbS3) QDs has been explained and discussed in chapter 5. The PbSe, PbS and PbSe/PbS core/shell QDs whose emission spans most of the NIR spectrum have been described which have been synthesized using wet chemical growth method. Their structural as well as optical properties have been investigated by XRD, UV-Vis spectroscopy, photo luminescence spectroscopy, and TEM. The UV-Visible-NIR spectra show a large blue shift attributing the enhanced optical properties, this size dependent blue shift in absorption edge is attributed to the quantum size effect. PL measurements show effectiveness of capping and core/shell structure formation as there is clear vindication of enhanced luminescence. Core/shell semiconductor QDs that were prepared by our method are low-cost, safe, and ubiquitous at least for II-VI and IV-VI group compounds.

It is well known that surface defect states play important roles in the luminescence properties of nanoparticles, which act as radiative or nonradiative centers in nanoparticles. The PL spectra of the PbS (1, 2 and 3) QDs were dominated by very strong emission peak at around 1300 nm,

1320 nm and 1325 nm respectively but PbS (2 and 3) shows another peaks at 1580 due to sulfur defects. The fluorescence enhancement may be attributed to a much higher concentration of radiative recombination centers. The PL intensity of 2-mercaptoethanol capped particles is dramatically enhanced. The PL spectra of the PbSe (1, 2 and 3) QDS were shows strong emission peak at around 1280 nm, 1322 nm and 1325 nm respectively but PbSe (2 and 3) shows another peaks at 1600 due to surface defects shown. The fluorescence enhancement may be attributed to a much higher concentration of radiative recombination centers. It is observed that the photoluminescence efficiency of capped PbSe QDs with higher concentration of 2-mercaptoethanol show high intensity due to passivation of surfaces. Emission spectra for as prepared PbSe/PbS (1, 2 and 3) QDs have been recorded. Interesting effect in PL spectra is the enhancement and single emission peak around 1460 nm for the PbSe/PbS (2 and 3) which can be associated with an interband connection between the interface of PbSe core and PbS disordered shell. PbS confines the photo generated electron–hole pairs to the PbSe core interface modified by the quantum confinement effect, leading to the passivation of non-radiative transitions and enhancing the luminescence intensity. Structures and subsequently different materials properties, and this phenomenon can be related to local (short), intermediate and long-range structural order–disorder. The peaks are also assumed to originate from the radiative recombination of carrier at surface trap states resulted from the compounded effect of PbSe at PbSe/PbS interface.

6.2 FUTURE ASPECTS

Future studies to complete the understanding of the shell material distribution around CdS core QDs includes trying shell material with smaller lattice mismatch comparing with the core material, such as CdS and ZnS. Further studies about PbS multishell QDS are important. The application of these PbSe multishell QDS in biology is worth further exploration due to their high luminescence, small hydrodynamic diameters, and optical stability. Studies using S, Se material to coat PbSe core QDs is also of great interest in both fundamental synthesis and potential applications, however, the growth of S, Se shell with significant thickness was not observed. Using different reaction chemicals, different precursors, and different reaction conditions can possibly lead to better shelling experiment results.

Main points for further research on these materials are:

- Synthesis of PbS and PbSe via wet chemical method for multiple exciton generation and application in Solar cell.
- Combination of II-VI and IV-VI like (PbS/CdS), (PbS/ZnS) Quantum Dots (QDs).
- Surface modifications of II-VI and IV-VI group QDs for Bio-applications.
- Thin film fabrication of II-VI and IV-VI group QDs by wet chemical method.
- Electrical and optical properties study of II-VI and IV-VI group QDs for photovoltaic device and Sensor application.

REFRENCES

1. K. S. Lee, P. N. Prasad, G. Huyet, C. H. Tan, Optics express 20 (2012) 10721.
2. H. Kumar, M. Kumar, P. B. Barman, R. R. Singh, Applied Physics A 117 (2014) 1249.
3. A. Valizadeh, H. Mikaeili, M. Samiei, S. M. Farkhani, N. Zarghami, A. Akbarzadeh, S. Davaran, Nanoscale research letters, 7 (2012) 1.
4. V. I. Klimov, A. A. Mikhailovsky, S. Xu, A. Malko, J. A. Hollingsworth, C. A. Leatherdale, M. G. Bawendi, Science 290 (2000) 314.
5. V. I. Klimov, Semiconductor and metal nanocrystals: synthesis and electronic and optical properties (2003) CRC Press.
6. B. O. Dabbousi, J. Rodriguez-Viejo, F. V. Mikulec, J. R. Heine, H. Mattoussi, R. Ober, M. G. Bawendi, The Journal of Physical Chemistry B 101 (1997) 9463.
7. J. Nanda, S. A. Ivanov, H. Htoon, I. Bezel, A. Piryatinski, S. Tretiak, V. I. Klimov, Journal of applied physics 99 (2006) 034309.
8. M. A. Malik, P.O. Brien, N. A. Revaprasadu, Chem. Mater. 14 (2002) 2004.
9. P. Reiss, J. Bleuse, A. Pron, Nano Lett. 2 (2002) 781.
10. M. Danek, K.F. Jense, C.B. Murray, M. G. Bawendi, Chem. Mater. 8 (1996) 173.
11. T. Mokari, U. Banin, Chem. Mater. 15 (2003) 3955.
12. M. Ethayaraja, C. R. Kumar, D. Muthukumaran, K. Dutta, R. J. Bandyopadhyaya, Phys. Chem. C 111 (2007) 3246.
13. S. A. Ivanov, J. Nanda, A. Piryatinski, M. Achermann, L. P. Balet, I. V. Bezel, P. O. Anikeeva, S. Tretiak, V. I. Klimov, J. Phys. Chem. B. 108 (2004) 10625.
14. H. Weller, Advanced Materials 5 (1993) 88–95.
15. H.C. Youn, S. Baral, J. H. Fendler, The Journal of Physical Chemistry 92 (1988) 6320.
16. L. Spanhel, M. Haase, H. Weller, A. Henglein, J. Am. Chem. Soc. 109 (1987) 5649.
17. R.G. Xie, U. Kolb, J. Li, T. Basche´ , A. Mews, J. Am. Chem. Soc. 127 (2005) 7480–7488.
18. C. W. Raubach, Y. V. B. De Santana, M. M. Ferrer, V. M. Longo, J. A. Varela, W. A. Junior, P. G. C. Buzolin, J. R. Sambrano, E. Longo, Chem. Phys. Lett. 536 (2012) 96.

19. A. Dinger, M. Hetterich, M. Goeppert, M. Gruen, C. Klingshirn, B. Weise, J. Liang, V. Wagner, J. Geurts, J. Cryst. Growth 200 (1999) 391.
20. M. Kokotov, G. Hodes, Chem. Mater. 22 (2010) 5483.
21. A. Eychmuller, A. Mews, H. Weller, Chem. Phys. Lett. 208 (1993) 59.
22. N. Sata, K. Eberman, K. Eberl, J. Maier, Nature 408 (2000) 946.
23. X. X. Guo, I. Matei, J. S. Lee, J. Maiera, Appl. Phys. Lett. 91 (2007) 103102.
24. A. Kumar, A. Jakhmola, V. Chaudhary, Journal of Photochemistry and Photobiology A: Chemistry 208 (2009) 195.
25. Y. Li, J. Feng, S. Daniels, N. L. Pickett, P. O. Brien, Journal of Nanoscience and Nanotechnology 7 (2007) 2301.
26. G. Jia, B. Hao, X. Lu, J. Yao, International Journal of Electrochemical Science 8 (2013)7976.
27. L. Cao, S. Hang, E. Shulin, Journal of Colloid and Interface Science 273 (2004) 478.
28. L. Cao, S. Huang, S. Lu, J. Lin, Journal of Colloid and Interface Science 284 (2005) 516.
29. G. Murugadoss, Spectrochimica Acta Part A: Molecular and Biomolecular Spectroscopy 93 (2012) 53.
30. A. L. Efros, A. L. Efros, Soviet Physics Semiconductors-Ussr 16 (1982) 772.
31. A. L. Efros, Solid state communications 70 (1989) 253.
32. A. L. Efros, M. Rosen, M. Kuno, M. Nirmal, D. J. Norris, M. Bawendi, Physical Review B 54 (1996) 4843.
33. Y. Kayanuma, Solid state communications 59 (1986) 405.
34. Y. Kayanuma, Physical Review B 38 (1988) 9797.
35. M. G. Bawendi, P. J. Carroll, W. L. Wilson, L. E. Brus, The Journal of Chemical Physics 96 (1992) 946.
36. L. E. Brus, J. Chem. Phys. 79 (1983) 5566.
37. L. E. Brus, J. Chem. Phys. 80 (1984) 4403.
38. L. E. Brus, J. Chem. Phys. 90 (1986) 2555.
39. H. M. Shmidt, H. Weller, Chem. Phys. Lett. 129 (1986) 615.
40. Y. Kayanuma, H. Momiji, Phys. Rev. B, 41 (1990) 10261.

41. N. Chestnoy, T. D. Harris, R. Hull, L. E. Brus, The Journal of Physical Chemistry 90 (1986) 3393.
42. D. J. Norris, A. Sacra, C. B. Murray, M. G. Bawendi, Phys. Rev. Lett. 72 (1994) 2612.
43. C. R. Kagan, C. B. Murray, M. Nirmal, M. G. Bawendi, Phys. Rev. Lett. 76 (1996) 1517.
44. Y. Wang, A. Suna, W. Mahler, R. J. Kasowski, Chem. Phys. 87 (1987) 7315.
45. Y. Nosaka, The Journal of Physical Chemistry 95 (1991) 5054.
46. B. Pejova, A. Tanuševski, I. Grozdanov, Journal of Solid State Chemistry 177 (2004) 4785.
47. J. C. Slater, G. F. Koster, Physical Review 94 (1954) 1498.
48. P. E. Lippens, M. Lannoo, Physical Review B 39 (1989) 10935.
49. N. A. Hill, K. B. Whaley, The Journal of chemical physics 100 (1994) 2831.
50. K. Leung, S. Pokrant, K. B. Whaley, Phys. Rev. B 57 (1998) 12291.
51. J. Perez-Conde and A. K. Bhattacharjee, Phys. Rev. B 63 (2001) 245318.
52. G. Allan, Y. M. Niquet, C. Delerue, , Appl. Phys. Lett., 77 (2000) 639.
53. S. Sapra, D. D. Sharma, Phys. Rev. B. 69 (2004) 125304.
54. M. V. Ramakrishanan, R. A. friesner, Phys. Rev. Lett. 67 (1991) 629.
55. A. Zunger, L. W. Wang, J. Chem. Phys. 100 (1994) 2394.
56. A. Zunger, L.W. Wang, Phys. Rev. B 51 (1995) 17398.
57. A. Zunger, L. W. Wang, Phys. Rev. B 53 (1996) 9579.
58. L. W. Wang, A. Zunger, Studies in Surface Science and Catalysis 103 (1997) 161.
59. M. Bruchez, M. Moronne, P. Gin, S. Weiss, A. P. Alivisatos, Science 281 (1998) 2013.
60. M. Klude, T. Passow, H. Heinke, D. Hommel, Physica status solidi (b) 229 (2002) 1029.
61. Coe, Seth, et al. "Electroluminescence from single monolayers of nanocrystals in molecular organic devices." Nature 420.6917 (2002): 800-803.
62. J. M. Hartmann, et al., Journal of Applied Physics 95 (2004) 5905.
63. P.C. Hiemenz, R. Rajagopalan, (Eds.) 14 (1997) CRC press.

64. R. Bali, N. Razak, A. Lumb, A.T. Harris, Int. Conf. In Nanoscience and Nanotechnology, 2006. ICONN'06. International Conference on. IEEE 7 (2006) 340592.
65. P. Rodgers, Nature Nanotechnology (2006) doi:10.1038/nnano.2006.5.
66. N.R. Jana, Z.L. Wang, T.K. Sau, T. Pal, Curr. Sci. 79 1367 (2000).
67. S. Panigrah, S. Kundu, S. K. Ghosh, S. Nath, S. Praharaj, B. Soumen, T. Pal, Polyhydron 25 (2006) 1263.
68. X. Song, W. Zhang, Z. Yin, J. Colloid Interface Sci. 273 (2004) 463.
69. C. J. Zhong, D. Mott, J. Galkowski, L. Wang, J. Luo, Langmuir 23 (2007) 5740.
70. S. Kapoor T, Mukherjee, Chem. Phys. Lett. 83 (2003) 370
71. H.H. Huang, F.Q. Yan, Y.M. Kek, C.H. Chew, G. Q. Xu, W. Ji, S. H. Tang, Langmuir 13 (1997) 172.
72. C.M. Liu, L. Guo, H.B. Xu, Z.Y. Wu, J. Weber, Micro electron. Engi. 66 (2003) 107.
73. R. Zhou, X. Wu, X. Hao, F. Zhou, H. Li W. Rao, Nucl. Instrum. Method Phys. Res. B 266 (2008) 599.
74. I. Lisiecki, M.B. Pileni, J. Am. Soc. 115 (1993) 3887.
75. J. Tanori, M.P. Pileni, Langmuir 13 (1997) 639.
76. S.H. Wu, D.H. Chen, J. Colloid Interface Sci. 273 (2004) 165.
77. R. Rossetti, R. Hull, J.M. Gibson, L.E. Brus, J Chem Phys. 82 (1985) 552.
78. A. Fojtik, H. Weller, U. Koch, A. Henglein, Phys Chem. 88 (1984) 969.
79. L.E. Brus, J. Chem. Phys. 80 (1984) 4403.
80. S. Chandra, N. Khare, Semicond. Sci. Technol. 2 (1987) 214.
81. S. Wageh, S.M. Liu, F.T. You, X.R. Xu, J. Lumin. 102 (2003) 768.
82. N. Karar, F. Singh, B.R. Mehta, J. Appl. Phys. 95 (2004) 656.
83. H. Tang, M. Yan, H. Zhang, M. Xia, D. Yang, Mat. Let. 59 (2005) 1024.
84. D. Kaushik, M. Sharma, A.B Sharma, R.K. Pandey, Journal of Nanoscince and Nanotechnology 8 (2008) 4303.
85. S. Chaure, N.B. Chore, R.K. Pandey, Journal of Nanoscince and Nanotechnology 7 (2007) 1.
86. L. Spanhel, M. Haase, H. Weller, A. Henglein, J Am Chem Soc. 109 (1987) 5649.

87. H. S. Zhou, I. Honma, H. Komiyama, J. W Haus, J. Phys. Chem. 97 (1993) 895.

88. A.R. Kortan, R. Hull, R.L. Opila, M.G. Bawendi, M.L. Steigerwald, P.J. Carrol, L.E Brus, J. Am. Chem. Soc. 112 (1990) 1327.

89. D.V. Talapin, A.L. Rogach, A. Kornowski, M. Haase, H. Weller, Nano. Lett. 1 (2001) 207.

90. M. Wang, J. Kwon Oh, T.E. Dykstra, X. Lou, G.D. Scholes, M.A. Winnik, Macromolecules 39 (2006) 3664.

91. D.W. Deng, J.S. Yu, Y. Pan, Journal of colloid and interface science 299 (2006) 225.

92. I. Mekis, D.V. Talapin, A. Kornowski, M. Haase, H. Weller, Journal of Physical Chemistry B 107 (2003) 7454.

93. L. Xu, L. Wang, X. Huang, Zhu J, H. Chen, K. Chen, Physica E 8 (2000) 129.

94. M. A. Hines, P. Guyot-Sionnest, J. Phys. Chem., 100 (1996) 468.

95. A.E. Raevskaya, A.L. Stroyuk, S.Y. Kuchmiy, Journal of colloid and interface science 302 (2006) 133.

96. M. Sharma, D. Gupta, D. Kaushik, A.B. Sharma, R. K Pandey, Journal of Nanoscience and Nanotechnology 8 (2008) 3949.

97. D. Schooss, A. Mews, A. Eychmüller, H. Weller Physical Review B 49 (1994) 17072.

98. E.A. Meulenkamp, J Phys Chem B 102 (1998) 5566.

99. M. Hilgendorff, L. Spanhel, Ch. Rothenhausler, G. Mu¨ller. J Electrochem Soc. 145 (1998) 3632.

100. K. Kang, K. Daneshvar, Journal of applied physics, 95 (2004) 646.

101. N. Arul Dhas, C. Paul Raj, A. Gedanken, Chemistry of materials 10 (1998) 3278.

102. A. Gedanken, J. Zhu, Y. Koltypin, Chem. Mater. 12 (2000) 73.

103. B. Pamplin, R.S. Feigelson, Thin Solid Films 60 (1979) 141.

104. J.A. James, R.C. Kell, Crystal Growth. Ed. Pamplin BR, Pergamon Press, New York (1975).

105. A.A. Chernov, Modern crystallography, Springer 1984.

106. J.C. Brice, J.C. Brice, The growth of crystals from liquids, Amsterdam: North-Holland Publishing Company, 1973.
107. S.K. Kulkarni, A.A. Khosravi, M. Kundu, P.D. Vyas, Appl. Phys Lett. 67 (1995) 2506.
108. S.K Kulkarni, Appl. Surf. Sc. 169 (2000) 438.
109. A.A. Bol, A. Meijerink, Phys. Rev. B 54 (1998) 15997.
110. A.A. Bol, A. Meijerink, Phy Chem.Chem. Phys. 3 (2001) 2105.
111. A.A. Bol, J. Ferwerda, J.A. Bergwerff, A. Meijerink. J. Lumin. 99 (2002) 325.
112. T.R. Ravindran, A.K. Arora, B. Balamurugan, B.R. Mehta, Nanostruc. Mat. 11 (1999) 603.
113. R. Benerjee, R. Jayakrishana, P. Ayyub, J. Phys: Condens. Matter (2000) 12 10647.
114. M.K. Naskar, A. Patra, M. Chatterjee Journal of colloid and interface science 29 (2006) 271.
115. H. Li, W.Y. Shih, W.H Shih, Nanotechnology 18 (2007) 205604.
116. R. Seoudi, A. B. El-Bailly, W. Eisa, A.A. Shabaka, S.I. Soliman, R. K. Abd El Hamid, R. A. Ramadan, Journal of Applied Sciences Research 8 (2012).
117. Z. Deng, L. Tong, M. Flores, S. Lin, J. X. Cheng, H. Yan, Y. Liu Journal of the American Chemical Society 133 (2011) 5389.
118. J. Niu, W. Xu, H. Shen, S. Li, H. Wang, L.S. Li, Bull. Korean Chem. Soc. 33 (2012) 393.
119. A. Rahdar, F. Izadpanah, World Applied Programming 3 (2013) 108.
120. T.D. Nguyen, W.Y. Hamad, M.J. MacLachlan. Chem. Commun. 49 (2013) 11296.
121. M. Taherian, A. S. Alvani, M. A. Shokrgozar, R. Salimi, S. Moosakhani, H. Sameie, F. Tabatabaee, Electronic Materials Letters 10 (2014) 393.
122. M. D. Peterson, S. C. Jensen, D. J. Weinberg, E. A. Weiss, ACS nano 8 (2014) 2826.
123. S. M. Liu, H. Q Guo, Z. H. Zhang, R. W. Li, Z. G. Chen, Physica E: Low-dimensional Systems and Nanostructures 8 (2000) 174.
124. A. Gtozman, E. Lifshitz, Materials Science and Engineering C 15 (2001) 17.
125. K. K. Song, S. Le, Curr. Appl. Phys. 1 (2001) 169.
126. V. V, Nikesh, S. Mahamuni, Semicond. Sci. Techno. 16 (2001) 687.

127. D. Valerini, A. Creti, M. Lomascolo, L. Manna, R. Cingolani, M. Anni, Phys. Rev. B. 71 (2005) 235409.

128. J. Zhao, J. Zhang, C. Jiang, J. Bohnenberger, T. Bashe, A. Mews, J. Appl. Phys. 96 (2004) 3206.

129. H. S Zhou, H. Sasahara, I. Honma, H. Komiyama, J.W. Haus, Chem. Mater. 6 1994 1534.

130. C. F. Hoener, K. A. Allan, A. J. Bard, A. Campion, M. A. Fox, T. E. Mallouk, J. M. White, The Journal of Physical Chemistry 96 (1992) 3812.

131. Y. J. Lee, T. G. Kim, Y. M. Sung, Nanotechnology 17 (2006) 3539.

132. Eychmuller, H. Weller, Phys. Rev. B 49 (1994) 072.

133. T. F. Towey, A. Khan-Lodi, B. H. Robinson, J. Chem. Soc. Faraday Trans. 86 (1990) 3757.

134. M. Braun, C. Burda, M. A. El-Sayed, Journal of Physical Chemistry A 105 (2001) 5548.

135. H. Borchert, D. V. Talapin, N. Gaponik, C. McGinley, S. Adam, A. Lobo, H. Weller, Journal of Physical Chemistry B 107 (2003). 9662

136. R. B. Little, M. A. El-Sayed, G. W. Bryant, S. Burke, Journal of Chemical Physics 114(4) (2001) 1813.

137. J. Xu, D. Battaglia, X. Peng, M. Xiao Journal of Colloid and Interface Science 284 (2005) 516.

138. A. SalmanOgli, A. Rostami, Journal of Nanoparticle Research, 13 (2011) 1197.

139. H. Qu, L. Cao, W. Liu, G. Su, B. Dong, H. Zhai,. Photoluminescence properties of ZnS/CdS/ZnS quantum dot–quantum wells doped with Ag+ ions. Journal of Nanoparticle Research, 13(10), 5 (2011) 5157-5161.

140. X. Zeng, W. Zhang, J. Cui, M. Zhou, H. Chen, Materials Research Bulletin 50 (2014) 359.

141. C. Giansante, L. Carbone, C. Giannini, D. Altamura, Z. Ameer, G. Maruccio, G. Gigli, Journal of Physical Chemistry C 117 (2013).

142. M. Nam, J. Park, S. W. Kim, K. Lee, Journal of Materials Chemistry A 2(11) (2014) 3978.

143. E. Pedrueza, A. Segura, R. Abargues, J. B. Bailach, J. C. Chervin, J. P. Martínez-Pastor, Nanotechnology 24 (2013) 205701.

144. J. Y. Woo, J. H. Ko, J. H. Song, K. Kim, H. Choi, Y. H. Kim, S. Jeong, Journal of the American Chemical Society 136 (2014) 8883.

145. S. Park, B. L. Clark, D. A. Keszler, J. P. Bender, J. F. Wager, T. A. Reynolds, G. S. Herman, Science 297 (2002) 65.

146. J. J. Li, A. Wang, W. Guo, J. C. Keay, T. D. Mishima, M. B. Johnson, X. Peng, J. Am. Chem. Soc. 2003 12512567.

147. J. Xu, D. Cui, T. Zhu, G. Paradee, Z. Liang, Q. Wang, A. Y. Wang, Nanotechnology, 17 (2006) 5428.

148. A. Sashchiuk, L. Langof, R. Chaim, E. Lifshitz, Journal of crystal growth 240 (2002) 431.

149. J. W. Stouwdam, J Shan, F. C. Veggel, A. G. Pattantyus-Abraham, J. F. Young, M. Raudsepp, Journal of Physical Chemistry C 111 (2007) 1086.

150. D. Yanover, R. Vaxenburg, J. Tilchin, A. Rubin-Brusilovski, G. Zaiats, R. K. Capek, E. Lifshitz, Journal of Physical Chemistry C 118 (2014) 17001.

151. X. Michalet, F. F. Pinaud, L. A. Bentolila, J. M. Tsay, S. J. J. L. Doose, J. J. Li, S. Weiss, science 307 (2005) 538.

152. I. L. Medintz, H. T. Uyeda, E. R. Goldman, H. Mattoussi, Nature materials 4 (2005) 435.

153. P. Alivisatos, Nature biotechnology 22 (2004) 47.

154. A. M. Smith, S. Dave, S. Nie, L. True, X. Gao, (2006). Multicolor quantum dots for molecular diagnostics of cancer.

155. X. Wu, H. Liu, J. Liu, K. N. Haley, J. A. Treadway, J. P. Larson, M. P. Bruchez, Nature biotechnology 21 (2003) 41-46.

156. X. Gao, Y. Cui, R. M. Levenson, L. W. Chung, S. Nie, Nature biotechnology 22 (2004) 969.

157. B. Dubertret, P. Skourides, D. J., Norris, V. Noireaux, A. H. Brivanlou, A. Libchaber, Science, 298 (2002) 1759.

158. W. C., Chan, T. P. Fu, Journal of applied polymer science 67 (1998)1085.

159. D. R. Larson, W. R. Zipfel, R. M. Williams, S. W. Clark, M. P. Bruchez, F. W. Wise, W. W. Webb, Science, 300 (2003) 1434.

160. M. Dahan, S. Levi, C. Luccardini, P. Rostaing, B. Riveau, A. Triller, Science 302 (2003) 442.

161. T. Takagahara, Physical review letters 71 (1993) 3577.

162. K. T. Ramesh, Nanomaterials (2009) 1.

163. J. Heath Chemical Society Reviews 27 (1998) 65.

164. Z. Guo, L. Tan, Fundamentals and applications of nanomaterials (2009) Artech House.

165. D. Khoklov, Lead Chalcogenides: Physics and Applications Optoelectronic Properties of Semiconductors and Superlattices, Taylor & Francis, 2003, 18, (b) M.J. Bruchez, M. Moronne, P. Gin, S. Weiss, A.P. Alivisatos, Science. 1998, 281, 2013 (c) D. Pantarotto, C.D. Partidos, J. Hoebeke, F. Brown, E. Kramer, J. P. Briand, S. Muller, M. Prato, A. Bianco, Chem. Biol. 2003, 10, 961 (d) J. Ma, H. Wong, L.B. Kong, K.W. Peng, Nanotech. 2003, 14, 619.

166. W. U. Huynh, J. J. Dittmer, A. P. Alivisatos, Science 295 (2002) 2435.

167. 177 K. G. U.Wijayantha, L. M. Peter, L. C. Otley, Sol. En. Mater. Sol. Cells. 83 (2004) 363.

168. S. A. McDonald, P. W. Cyr, L. Levina, E. H. Sargent, Appl. Phys. Lett. 85 (2004) 2089.

169. S. Zhang, P. W. Cyr, S. A. McDonald, G. Konstantos, E. H. Sargent, Appl. Phys. Lett. 87 (2005) 233101.

170. A. Maria, P. W. Cyr, E. J. D. Klern, L. Levina, E. H. Sargent, Appl. Phys.Lett. 87 (2005) 213113.

171. E. J. D. Klem, D. D. MacNeil, P. W. Cyr, L. Levina, E.H. Sargent, Appl. Phys. Lett. 90 (2007) 183113.

172. K. W. Johnston, A. G. Pattantyus-Abraham, J. P. Clifford, S. H. Myrskog, D. MacNeil, L. Levina, E. H. Sargent, Appl. Phys. Lett. 92 (2008) 151115.

173. P. Fritz, S. Guenes, J. Luther, S. Kumar, N. S. Sariciftci, G. D. Scholes, J. Photochem. Photo Bio A; Chem. 195 (2008) 39.

174. D. H. Cui, J. Xu, T. Zhu, G. Paradee, S. Ashok, M. Gerhold, Appl. Phys. Lett. 88 (2006) 183111.

175. X. Jiang, R. D. Schaller, S. B. Lee, J. M. Pietryga, V. I. Klimov, A. A. Zakhidov, J. Mater. Res. 22 (2007) 2204.

176. G. I. Koleilat, L. Levina, H. Shukla, S. H. Myrskog, S. Hinds, A. G. Pattantyus-Abraham, E. H. Sargent, ACS Nano 2 (2008) 833.

177. E. Kikuchi, S. Kitada, A. Ohno, S Aramaki, Shinya Maenosono, Appl. Phys. Lett. 92 (2008) 173307.

178. L. Cademartiri, J. Bertolotti, R. Sapienza, D. S. Wiersma, G. V. Freymann, G. A. Ozin, J. Phys. Chem B 110 (2006) 671.

179. J. H. Warner, E.Thomsen, A.R Watt, N. R. Heckenberg and H. R.-Dunlop, Nanotech. 16 (2005) 175.

180. I. Fushman, D. Englund, J. Vuckovic, Appl. Phys. Lett. 87 (2005) 241102.

181. D. Englund, D. Fattal, E. Waks, G. Solomon, B. Zhang, T. Nakaoka, Y. Arakawa, Y. Yamamoto and J. Vuckovic, Phys. Rev. Lett. 95 (2005) 013904.

182. D. F. Dorfner, T. Hrilmann, G. Abstreiter, J. J. Finley, App. Phys. Lett. 91 (2007) 233111.

183. C. Paguet, F. Yoshino, L. Levina, I. Gourevich, E. H. Sargent, E. Kumacheva, Adv. Funct. Mater. 16 (2006) 1892.

184. R. D. Schaller, M. A. Petruska, V. I. Klimov, J. Phys. Chem B 107 (2003) 13765.

185. T. Asano, B. S. Song, S. Noda, Opt. Express, 14 (2006) 1996.

186. Z. Wu, Z. Mi, P. Bhattacharya, T. Zhu, J. Xu, Appl. Phys. Lett. 90 (2007) 171105.

187. V.K. LaMer, R.H. Dinegar, Journal of the American Chemical Society 72 (1950) 4847.

188. U. Winkler, D. Eich, Z.H. Chen, R. Fink, S.K. Kulkarni, E. Umbach, Chem. Phys. Lett. 306 (1999) 95.

189. A. Khosravi, M. Kundu, B.A. Kuruvilla, G.S. Shekhawat, R.P. Gupta, A.K. Sharma, P.D. Vyas, S.K. Kulkarni, Appl. Phys. Lett. 67 (1995) 2506.

190. P.H. Borse, N. Deshmukh, R.F. Shinde, S.K. Date, S.K. Kulkarni, J. Mater. Sci. 34 (1999) 6087.

191. H.C.J. Moseley. Energy-dispersive X-ray microanalysis (1913).

192. L. Yang, D.J. Watts, Toxicol. Lett. 158 (2005) 122.
193. Z. Guo, K. Lei, Y. Li, H.W. Ng, S. Prikhodko, H.T. Hahn Compos. Sci. Technol. 68 (2008) 1513.
194. A.L. Willis, N.J. Turro, S.O. Brien, Chem. Mater. 17 (2005) 5970.
195. M. Nirmal, L. Brus, 32 (1999) 407.
196. W. K. Leutwyler, S. L. Bürgi, H. Burgl, Science, 271 (1996) 933.
197. H. Weller, Angewandte Chemie, 32 (1993) 41.
198. U. Banin, Y. Cao, D. Katz, O. Millo, Nature, 400 (1999) 542.
199. W. CHAN, Science, 281 (1998) 2016.
200. G. P, Mitchell, C. A. Mirkin, R. L. Letsinger, Journal of the American Chemical Society, 121 (1999) 8122.
201. R. W. Saalfrank, I. Bernt, M. M. Chowdhry, F. Hampel, G. Vaughan, Chemistry-A European Journal, 7 (2001) 2765.
202. A.P. Alivisatos, Science. 271 (1996) 933.
203. M.A. Anderson, S. Gorer, R.M. Penner, the Journal of Physical Chemistry B 101 (1997) 5895.
204. X. Peng, M.C. Schlamp, A. Kadavanich, A.P. Alivisatos, J. Am.Chem. Soc.119 (1997)7019.
205. J.F.A. Oliveira, T.M. Milao, V.D. Araujo, M.L. Moreira, E. Longo, M.I.B. Bernardi, J. Alloy Compd. 509 (2011) 6880.
206. R. Alexandre, Loukanova, D. Ceco, Dushkina, I. Karolina, V. A Papazovaa, V. M Kirova, E.A Abrashevb, Colloids and Surfaces A: Physicochem. Eng. Aspects 245 (2004) 9.
207. D.F. Fanga, Z.M. Zhangb, Z.P. Wangb, Z.J. Ding Physics Procedia 32 (2012) 920.
208. M. Ethayaraja, C. Ravikumar, D. M. Dutta, R. Bandyopadhyaya, J. Phys. Chem. C 111 (2007) 3246.
209. V.T.K. Lien, C.V. Ha, L.T. Ha, N.N. Dat, Journal of Physics: Conference Series 187 (2009) 012028.
210. J.S. Steckel, J.P. Zimmer, S. Coe-Sullivan, N. E. Stott, V. Bulovic, M.G. Bawendi, Angew. Chem. Int. Ed. 43 (2004) 2154 –2158.
211. M. Koneswaran, R. Narayanaswamy, Microchim Acta 178 (2012) 171.

212. P.K. Sahoo, S.S.K. Kamal, T.J. Kumar, B. Sreedhar, A.K. Singh1, S.K. Srivastava, Defence. Sci.J. 59(4) (2009) 447.
213. W.C.W. Chan, S.M. Nie, Science.281 (1998) 2016.
214. G. Hodes, Phys.Chem.Chem.Phys.9 (2007) 2181.
215. J.R. Weertman, Mater. Sci. Eng. A. 166 (1993) 161.
216. H.Van.Swygenhoven, Science. 296 (2002) 66.
217. M. Marandi, N. Taghavinia, A. Irajizad, S. M. Mahdavi, Nanotechnology 16 (2005) 334.
218. Y. C. Charles, J. Wang, J. Am. Chem. Soc. 126 (2004) 14336.
219. S.H. Hwang, C.N. Moorefield, P.S. Wang, K.U. Jeong, S.Z.D. Cheng, K.K. Kotta, G.R. Newkome, Chem. Commun. (2006), 3495.
220. C.N.R. Rao, G.U. Kulkarni, P.J. Thomas, P.P, Edwards. Chem. Eur. J. 8 (2002)28.
221. X. Xu, Appl. Catal. B. 102 (2011)147.s
222. R.S. Singh, S. Bhushan, A.K. Singh, S.R. Deo, D.J. Nanomater. Bios.6 (2011)403.
223. R. Seoudi, Physica. B. 405 (2010)919.
224. A. Reddy, D. Divya, A. Murali, G. Vijayalakshmi, R.P. Reddy, B.K. ptoethanol, Physica B. 406 (2011) 1944.
225. E. Assaid, E. Feddi, J.E. Khamkhami, d.F. Dujardin, J. Phys.: Condens. Matter 15 (2003) 175.
226. A.D. Yoffe, Adv. Phys. 42 (1993) 173.
227. W. Swelm, A. Higazy M. Algradee, World Journal of Condensed Matter Physics, 1 (02) (2011) 24.
228. G. Jia1, B. Hao, X. Lu, J. Yao, Int. J. Electrochem. Sci., Vol. 8, 2013
229. S. Zhou, L. Dong, S. Popov, A. Friberg, Europ. Opt. Soc. Rap. Public. 8, (2013) 13042.
230. H. Kamisaka, Svetlana, V. Kilina, K. Yamashita, O.V. Prezhdo, J. Phys. Chem. C 2008, 112, 7800.
231. H. Tas, M. Sahin Journal of Applied Physics 111, (2012) 083702.
232. Y. Wang, N. Herron, J. Phys. Chem. 95(1991) 525.
233. M. Marandi, N. Taghavinia, A.Z. Iraj, Mandevi, Nanotechnol 17 (2006) 1230.
234. S. Jamali, E. S. Iranized, S.F. Shayestech. Int. J. Nanosci. & Nanotechnol. (2007) 3.

235. K. Murakoshi, H. Hosokawa, M.Saito, Y. Wada, C. Sakata, H. Mori and S. Yanagida, J. Chem. Soc. Faraday Trans. 94 (1998)579.
236. A. Sengupta, B. Jiang, K.C. Mandal, J.Z. Zhang, J. Phys. Chem. B. 103 (1999) 3128.
237. M.C Brelle, J.Z. Zhang, L. Nguyen, R.K. Mehra, J. Phys. Chem. A 103 (1999) 10194.
238. C. Unni, D. Philip, Gopchandran, K. Spectrochim. Acta. A 71 (2008) 1402
239. E. Longo, Phys. Rev. B. 69 (2004) 125115.
240. L.S. Cavalcante, Cryst. Eng. Comm 14 (2012) 853.(W. Hoheisel, V.L. Colvin, C.S. Johnson, A.P. Alivisatos, J. Chem. Phys. 101(1994) 8455.
241. B.C. Zhang, Y.H. Shen, A.J. Xie, L.B. Yang, X.F Wang, Mater. Chem. Phys. 116 (2009) 392.
242. J. Nanda, D. D. Sarma, J. Appl. Phys.90 (2001) 2504.
243. R.N. Bhargava, D. Gallagher, Phys. Rev. Lett. 72 (1994) 416.
244. P.V.B. Lakshmi, K.S. Raj, K. Ramachandran, Cryst. Res. Technol. 44 (2009) 153.
245. N. Murase, R. Jagannathan, Y. Kanematsu, M. Watanabe, A. Kurita, H. Hirata, T. Yazawa, T. Kushida, J. Phys. Chem. B. 103 (1999) 754.
246. S. Wageh, Z.S. Ling, X.X. Rong, J. Cryst. Growth.255 (2003) 332.
247. S.K. Panda, A. Datta, S. Chaudhuri, Chemical Physics Letters. 440 (2007) 235.
248. V.M. Longo, J. Phys. Chem. C. 115 (2011) 5207.
249. K.S. Siow, L. Britcher, S. Kumar, H.J. Griesser, A Review, Plasma Process Polym. 3 (2006) 392.
250. R.A. Sperling, W.J. Parak, Phil. Trans. R. Soc. A. 368 (2010) 1333.
251. J. Gubicza, G. Tichy, T. Ungára, Powder Diffraction. 20 (4) (2005) 366.
252. M. Koneswaran, R. Narayanaswamy, Microchim Acta. 178 (2012) 171.
253. J.G. Díaz, M. Zieliński, W. Jaskólski, G.W. Bryant, Physical Review B 74 (2006) 205309.
254. J. Pérez-Conde, A. K. Bhattacharjee, Phys. Rev. B 67 (2003) 235303
255. N. Soltani, E. Saion, M. Erfani, A. Bahrami, M. navaseri, K. Rezaee, Md. Z. Hussein, Chalcogenide Letters 9 (2012) 379.
256. G. Faming, Applied Physics Letters 98 (2011) 193105.
257. I.O. Oladeji, L. Chow, Thin Solid Films 474 (2005) 77.

258. J.F. Lu, X.H. Zeng, H.F. Liu, W. Zhang, Y. Zhang, J. Phys. Chem. C 116 (2012) 23013.

259. E. Lifshitz, H. Porteanu, A. Glozman, H. Weller, M. Pflughoefft, A. Echymuller, Journal of Physical Chemistry B 103 (1999) 6870.

260. A.L. Patterson, Phys. Rev. Lett. 56, (1939) 978.

261. X.G. Peng, M.C. Schlamp, A.V. Kadavanich, A.P. Alivisatos, J. Am. Chem. Soc. 119 (1999) 77019

262.

263. P. Samokhvalova, P. Linkova, J. Michelb, M. Molinarib and I. Nabiev, Proc. of SPIE Vol.

264. J. Archana, M. Sabarinathan, M. Navaneethan, S. Ponnusamy, C. Muthamizhchelvan, Y. Hayakawa, Materials Letters 125 (2014) 35.

265. E.R. Goldman, E.D. Balighia, H. Mattoussi, M.J. Kuno, M. Mauro, P.T. Tran, G.P. Anderson, J. Am. Chem. Soc. 124 (2002) 6378.

266. C. B. Murray, D. J. Norris, M. G. Bawendi, J. Am. Chem. Soc. 115 (1993) 8706.

267. X. G Peng, L. Manna, W. D. Yang, J. Wickham, E. Scher, A. Kadavanich, A. P. Alivisatos, Nature 59 (2000) 404.

268. X. G Peng, J. Wickham, A. P. Alivisatos, J. Am. Chem. Soc. 120 (1998) 5343.

269. A. D. Yoffe, Adv. Phys. 42 (1993) 173.

270. T. Okuno, Y. Masumoto, M. Ikezawa, T. Ogawa, A. A. Lipovskii, Applied physics letters 77 (2000) 504.

271. S. Hinds, S. Myrskog, L. Levina, G. Koleilat, J. Yang, S. O. Kelly, E. H. Sargent, Journal of American Chemical Society 129 (2007) 7218.

272. J. C. Liu, H. Z. Yu, Z. L. Wu, W. L. Wang, J. B. Peng, Y. Cao, Nanotechnology 19 (2008) 345602.

273. L. C. Brousseau, Q. Zhao, D. A. Shultz, D. L. Feldheim, J. Am. Chem. Soc. 120 (1998) 7645.

274. P. T. Guerreiro, S. Ten, N. F. Barrelli, J. Butty, G. E. Jabbour, N. Peyghambarian, Appl. Phys. Lett. 71 (1997) 1595.

275. Z. Hens, D. Vanmaekelbetgh, E. J. A. J. Stoffels, H. V. Kempen, Phys. Rev. Lett. 88 (2002) 236803.

276. S. A. Mcdonald, G. Konstantatos, S. Zhang, W. P. Cyr, E. Klem, L. Levina, Nat. Mater. 4 (2005) 138.

277. S. Zhang, P. Cyr, S. Mcdonald, G. Konstantatos, E. Sargent, Appl. Phys. Lett. 87 (2005) 233101.

278. S. Gunes, K. P. Fritz, H. Neugebauer, N. S. Sariciftci, S. Kumar, G. D. Scholes, Solar Energy Materials and Solar Cells 91 (2007) 420.

279. P. Wang, L. Wang, B. Ma, B. Li, Y. Qiu, The Journal of Physical Chemistry B 110 (2006) 14406.

280. R. Bayon, R. Musembi, A. Belaidi, M. Bar, T. Guminskaya, M. C. Lux-Steiner, T. h. Dittrich, Solar energy materials and solar cells 89 (2005) 13.

281. E. J. D. Klem, D. D. MacNeil, W. P. Cyr, L. Levina, E. H. Sargent, Applied physics letters 90 (2007) 183113.

282. P. Gadenne, Y. Yagil, G. Deutscher, J. Appl. Phys. 66 (1989) 3019.

283. G. Kanstantatos, C. Huang, L. Levina, Z. Lu, E. H. Sargent, Advanced Functional Materials 15 (2005) 1865.

284. M. A. Hines, G. G. Scholes, Adv. Mater. 15 (2003) 1844.

285. R. S. Kane, R. E. Cohen, R. J. Silbey, The Journal of Physical Chemistry 100 (1996) 7928.

286. R. D. Schaller, M. Sykora, J. M. Pietryga, V. I. Klimov, Nano Letters 6 (2006) 424.

287. R. J. Ellingson, M. C. Beard, J. C. Johnson, P. Yu, O. I. Micic, Nozik AJ, A. L. Efros Nano Letters 5 (2005) 865.

288. C. B. Murray, S. Sun, W. Gaschler, H. Doyle, T. A. Betley, C. R. Kagan, IBM Journal of Research and Development 45 (2001) 47.

289. H. Du, C. Chen, R. Krishnan, T. D. Krauss, J. M. Harbold, F. W. Wise, M. G. Silcox, J. Nano Lett. 2 (2002) 1321.

290. B. Wehrenberg, C. Wang, P. Guyot-Sionnest, The Journal of Physical Chemistry B 106 (2002) 10634.

291. W. W. Yu, J. C. Falkner, B. S. Shih, V. L. Colvin, Chemistry of materials 16 (2004) 3318.

292. J. H. Warner, E. Thomsen, A. R. Watt, N. R. Heckenberg, H. Rubinutein-Dunlop, Nanotechnology 16 (2005) 175.

293. M. Brumer, A. Kigel, L. Amirav, A. Sashchiuk, O. Solomesch, N. Tessler, E. Lifshitz, Advanced Functional Materials 15 (2005) 1111.

294. A. H. Ip, S. M. Thon, S. Hoogland, , O. Voznyy, D. Zhitomirsky, R. Debnath, L. Levina, L. Rollny, G. Carey, A. Fischer, K. Kemp, I. Kramer, Z. Ning, A. Labelle, K. Chou, A. Amassian, E. H. Sargent, Nature Nanotechnology 7 (2012) 577 .

295. L. Etgar, D. Yanover, R. K. Capek, R. Vaxenburg, Z. Xue, B. Liu, M. Nazeeruddin, E. Lifshitz, M. Gratzel, Advanced Functional Materials 23 (2013) 2736.

296. F. Qu, R. S. Silva, N. O. Dantas, Physica Status Solidi (B) 232 (2002) 95.

297. Z. Zhang, S. H. Lee, J. J. Vittal, W. S. Chin, The Journal of Physical Chemistry B 110 (2006) 6649.

298. G. Konstantatos, I. Howard, A. Fischer, S. Hoogland, J. Clifford, E. Klem, L. Levina, E. H. Sargent, Nature 422 (2006) 180.

299. R. R. Hawaldar, K. G. Kanadeb, K. R. Patilc, S. D. Sathayed, U. P. Mulika, D. P. Amalnerkar, Materials chemistry and physics 91 (2005) 447.

300. S. T. Lakshmukvmar, A. C. Rastogi, Solar energy materials and solar cells 32 (1994) 7.

301. M. A. Korzhuev, Fiz. Khim. Obrab. Mater. 3 (1991) 131–134

302. J. Zhu, X. Liao, J. Wang, H. Y. Chen, Materials research bulletin 36 (2001) 1169.

Metadata Sheet in DOC format for the submission of B Tech Project Report/ Ph.D Thesis in PDF Format

Ph.D Thesis

Title of the Project Report / Thesis: "DEVELOPMENT OF II-VI AND IV-VI GROUP QUANTUM DOTS AND THEIR CORE/SHELL STRUCTURES"

Name of Student(s): Hitanshu Kumar **116902 [Enrolment Number]**

Branch: Physics and Materials Science

Name of Project Supervisor(s)/Guide(s)

1. Dr. Ragini Raj Singh

2. Prof. P. B. Barman

Admission Year: 2011

Project / Thesis Viva Date: 12 February 2016

Abstract:
This thesis work preferentially concerned with the size tunable and stable quantum dots (QDs) synthesized by solution growth method at room temperature using 2-mercaptoethanol. Excellent structural, optical and surface properties have been attained such as highly stable structure and high luminescence. Prepared quantum dots structures and core/shell quantum dots structures are: CdS, ZnS, CdS/ZnS, ZnS/CdS, ZnS/CdS/ZnS, PbS, PbSe, PbSe/PbS.

Keywords: Quantum dots, inverted core/shell structures, electron microscopy, luminescence, FTIR